4. RESULTS

4.1. Semi-solid metal processing

4.1.1. ProCAST simulation of SSM-HPDC of plates

ProCAST (operating in semi-solid mode with "Viscosity" defined with "Power Cut-Off") was used to provide an indication of the flow behaviour and cooling characteristics of the plates during HPDC. Figure 4.1 shows the simulated flow behaviour of the SSM-slurry during HPDC. Complete filling of the die is predicted to occur after only ~ 0.33 s (Fig. 4.1(c)).

To determine how the plates cool down in the die during the intensification step, values of $T_{initial}$ = 580^{o}C (casting temperature) and T_{die} = 250^{o}C were used for the simulation. Complete solidification is predicted to occur within ~ 5.5 s within the plate (Fig. 4.2(a)), whereas it is predicted to occur only after ~ 20 s in the relatively high-volume biscuit (Fig. 4.2(b)).

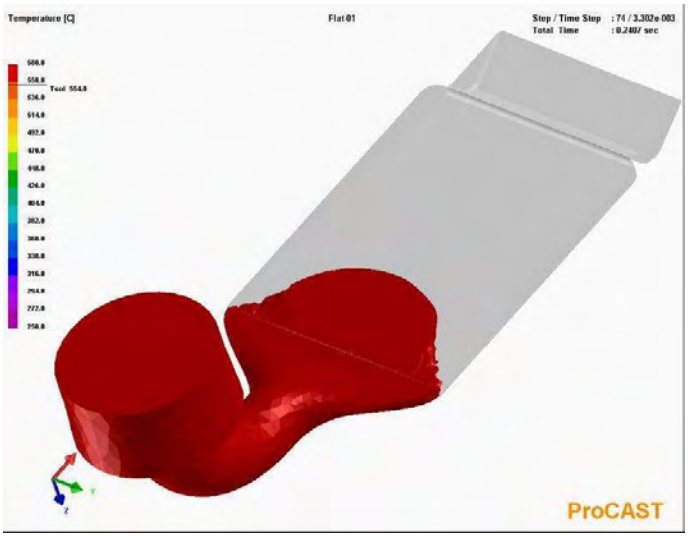

(a)

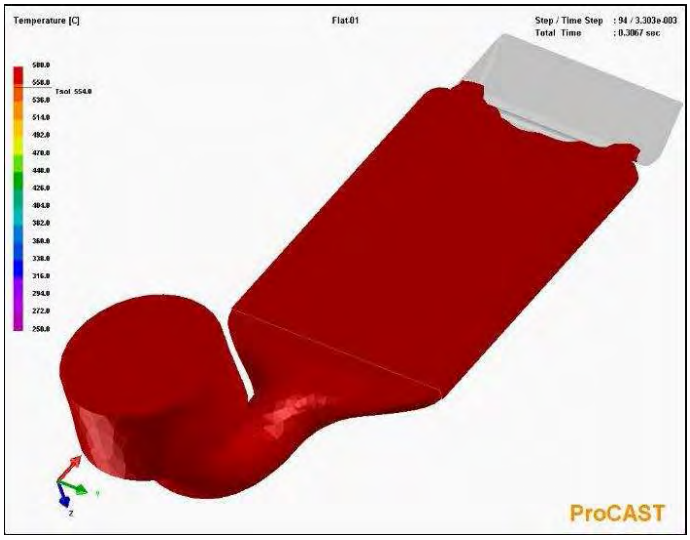

(b)

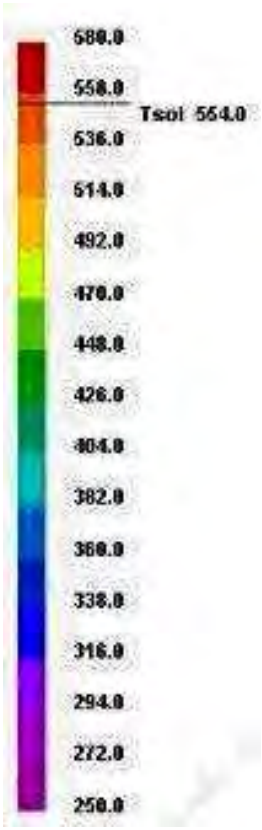

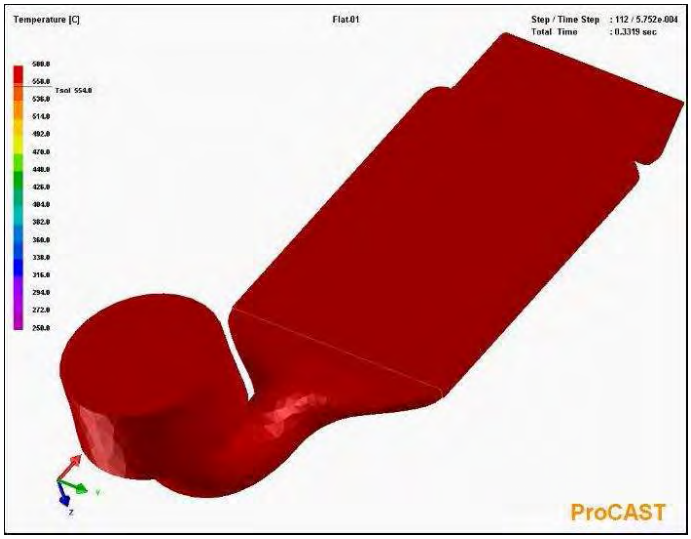

(c)

Figure 4.1: ProCAST simulation of filling of the die during SSM-HPDC after (a) 0.24 s, (b) 0.30 s and (c) 0.33 s.

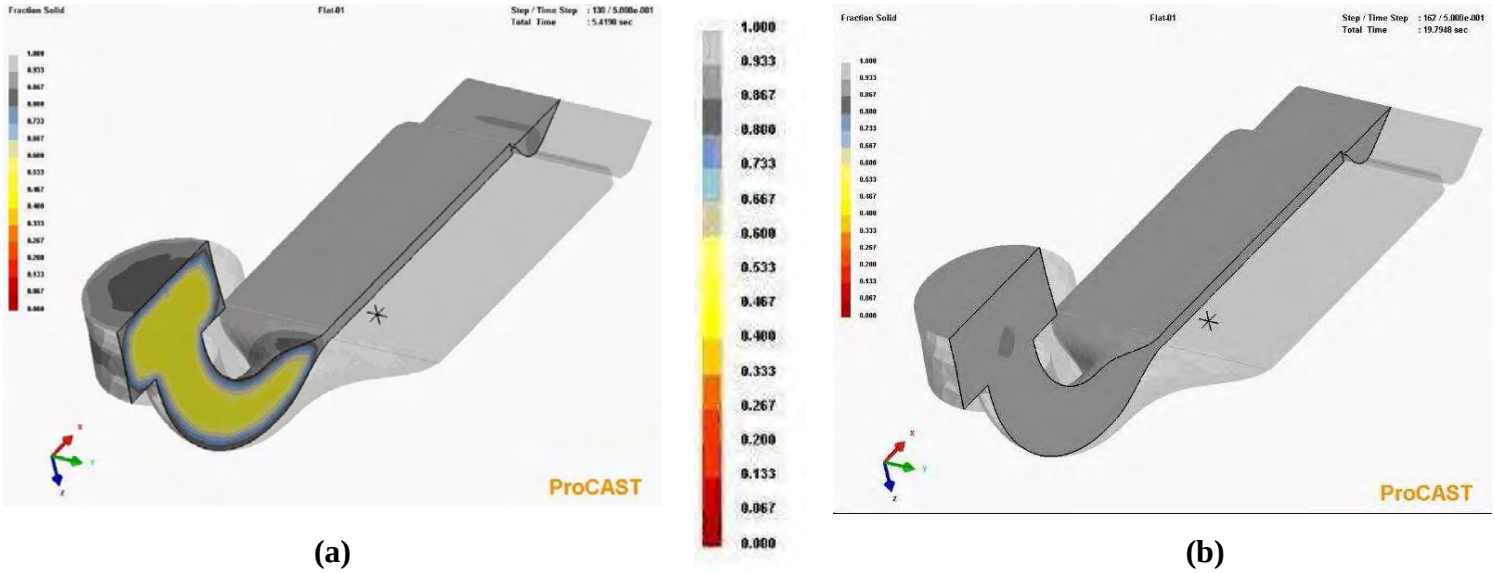

(a) **(b)**

Figure 4.2: ProCAST simulation of the solid fraction as a function of intensification time showing complete solidification in (a) the plate after 5.5 s and (b) the biscuit after 20 s.

The cooling behaviour within different parts of the plate-casting during intensification between 0-10s, 10-20s and 20-30s is compared in Fig. 4.3. The fastest cooling rates within the plates of ~ 18^{o}C/s are shown to occur during the first ten seconds of intensification (Fig. 4.4). Thereafter, the cooling rates drop significantly to ~ 9^{o}C/s between 10-20s and only ~ 2.5^{o}C/s between 20 and 30s. The large (high-volume) biscuit is shown to have a low cooling rate throughout of between 2 and 8^{o}C/s.

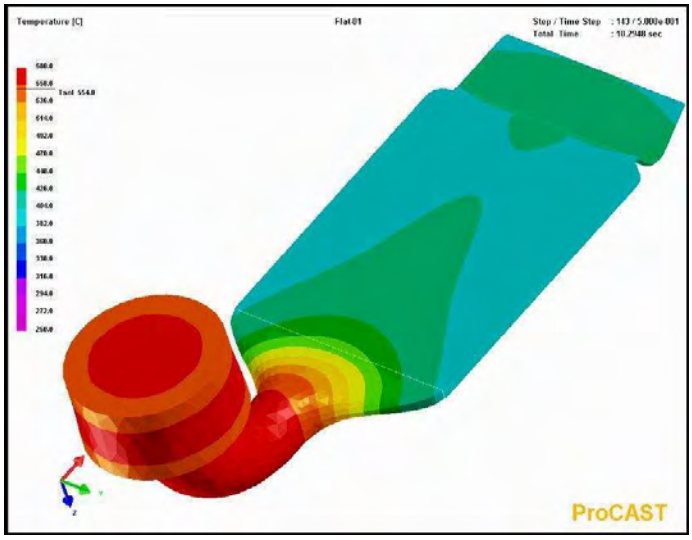

(a)

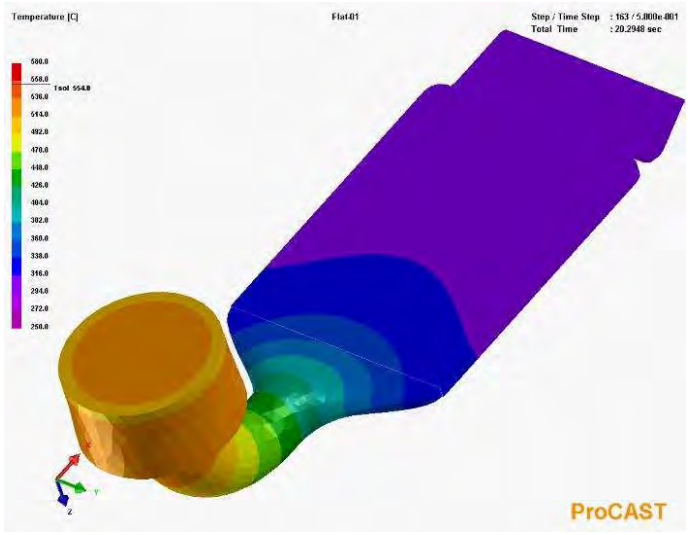

(b)

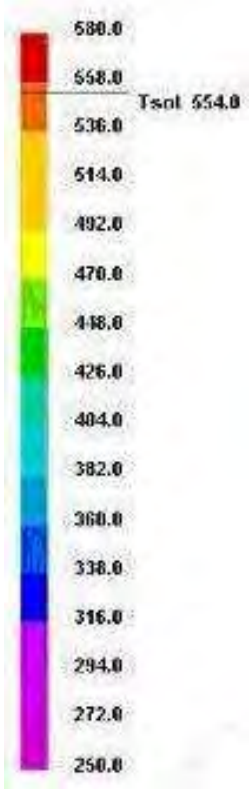

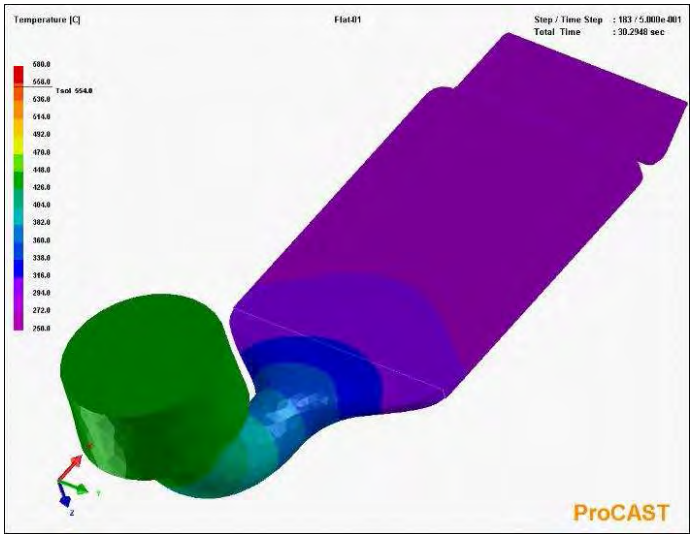

(c)

Figure 4.3: Temperature distribution within the plate during intensification in the die for (a) 10 s, (b) 20 s and (c) 30 s as predicted by ProCAST.

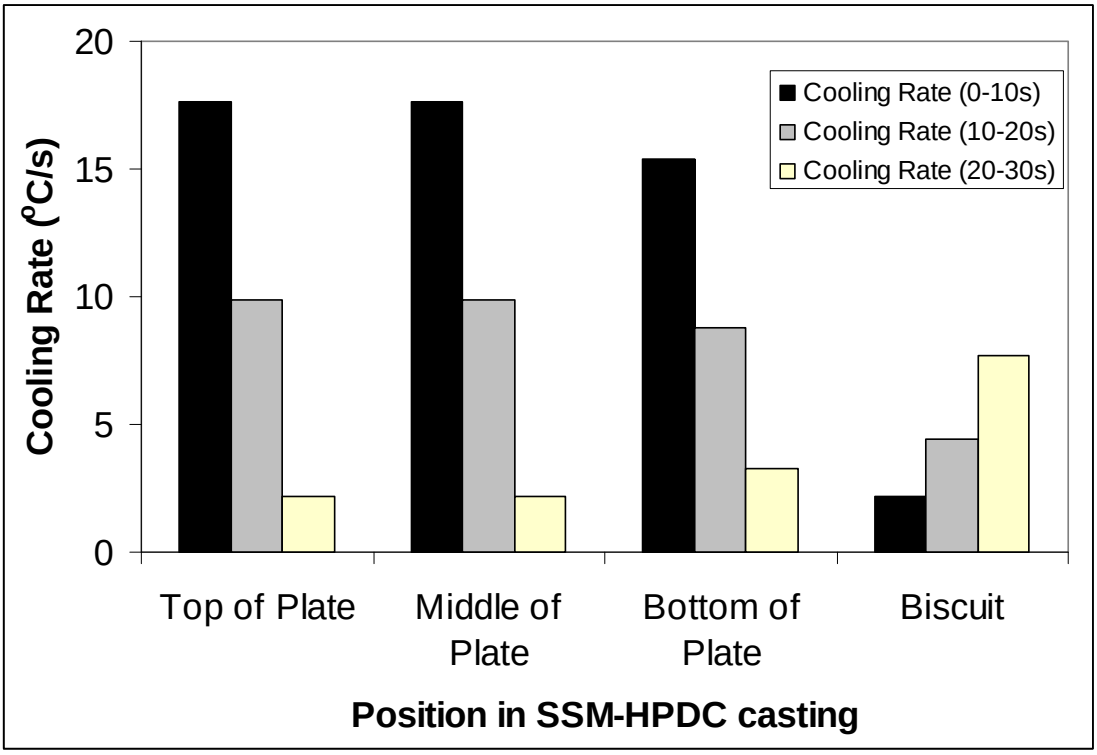

Figure 4.4: The average cooling rates achieved during intensification within different parts of the plate-casting.

4.1.2. Optical microscopy of SSM-HPDC of plates

Optical micrographs of the typical as-cast (F temper) microstructure of SSM-HPDC Al-7Si-Mg alloys are shown in Figure 4.5(a) (low magnification) and Figure 4.5(b) (high magnification). The microstructure consists of globular primary α-Al and a fine eutectic with fibrous silicon particles corresponding to a MR number (Table 2.2) of 5.

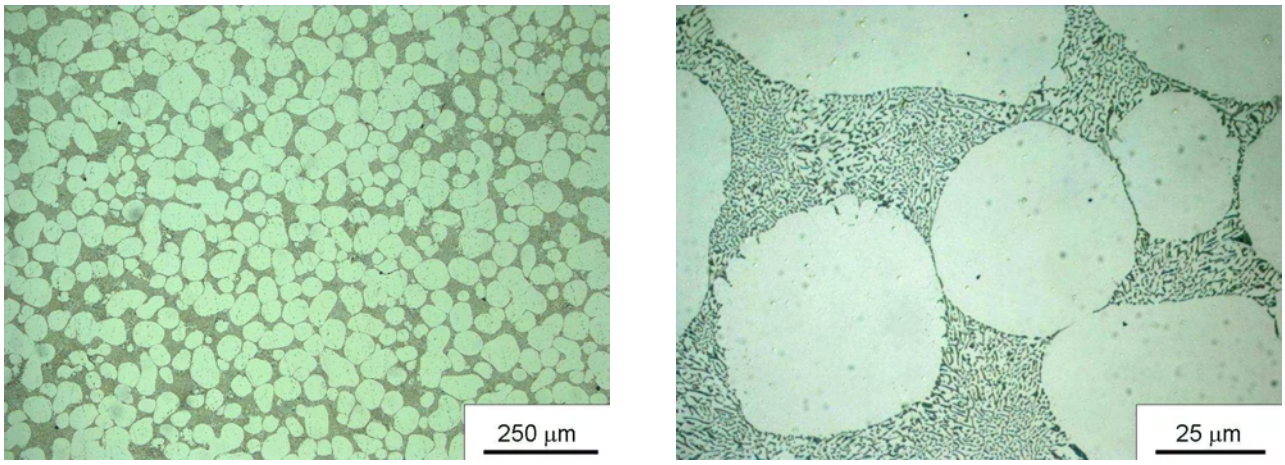

(a) **(b)**

Figure 4.5: Typical as-cast (F temper) microstructure of Al-7Si-Mg alloys after SSM-HPDC at (a) low magnification and (b) high magnification.

Statistical analysis of the microstructures of as–cast SSM-HPDC Al-7Si-Mg alloys shows a typical globule diameter of ~70 µm with roundness (Eq. 4.1) of ~ 1.4 (Table 4.1). Roundness was used as a parameter to describe the primary α-Al globules, since round particles are a prerequisite for SSM-processing.

Table 4.1: Statistical analysis of diameter and roundness of primary α-Al globules in SSM-HPDC Al-7Si-Mg alloys.

	Diameter (µm)	**Roundness**
Mean	69.5	1.43
Std. Dev	26.8	0.38
Samples	587	587

$$\textbf{Roundness} = (\text{Perimeter})^2 / (4\pi \times \text{area}) \qquad (4.1)$$

Perfectly circular areas will have a roundness of 1 and other shapes > 1.

4.2. Solution heat treatment

4.2.1. Spheroidisation of eutectic Si

The size and shape of the eutectic silicon particles in Al-7Si-Mg alloys can be "modified" (refined) either by chemical additions such as Sr or by rapid cooling during solidification (Table 2.2). Figure 4.6 shows optical micrographs of as-cast SSM-HPDC Al-7Si-Mg alloys with varying Sr contents. Statistical analysis of the eutectic Si-particles in these samples is presented in Table 4.2. The aspect ratio (the ratio between the major axis and minor axis of an ellipse equivalent to the object) is used for the eutectic Si-particles, since this parameter has been shown to influence the properties of these alloys [101].

Table 4.2: Statistical analysis of equivalent diameter and aspect ratio of eutectic Si in as-cast SSM-HPDC Al-7Si-Mg alloys with 2, 14 and 200 ppm Sr.

	Diameter (μm)			Aspect ratio		
	2 ppm	**14 ppm**	**200 ppm**	**2 ppm**	**14 ppm**	**200 ppm**
Mean	1.47	0.62	0.86	2.59	2.03	2.13
Std.Dev	1.22	0.57	0.79	2.0	0.95	1.2
Samples	772	1302	792	772	1302	792

The SSM-HPDC processed alloy containing 2 ppm Sr has coarser Si-eutectic particles with a higher aspect ratio (MR = 3) than the 14 ppm Sr and the 200 ppm Sr alloys (Table 4.2). The full modification (MR = 5) of the 14 ppm Sr alloy is due to the high cooling rates that are achieved during HPDC (Fig. 4.4). For comparison, Fig. 4.7 shows the unmodified microstructure (MR = 1) of the 14 ppm Sr alloy that had been rheoprocessed only and left to cool to room temperature in air (no HPDC).

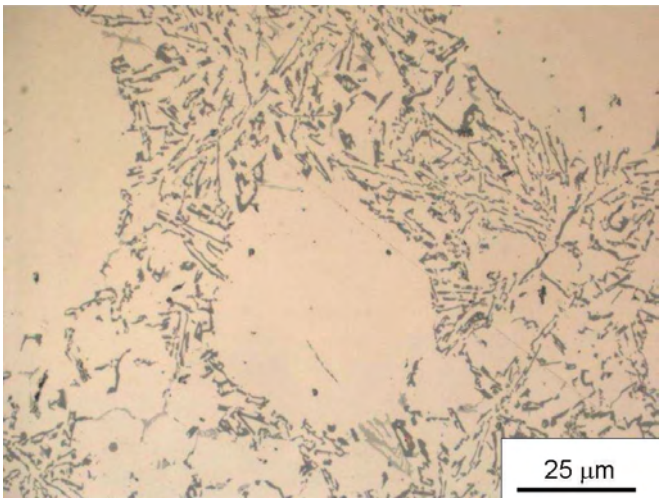

2 ppm Sr (MR = 3)

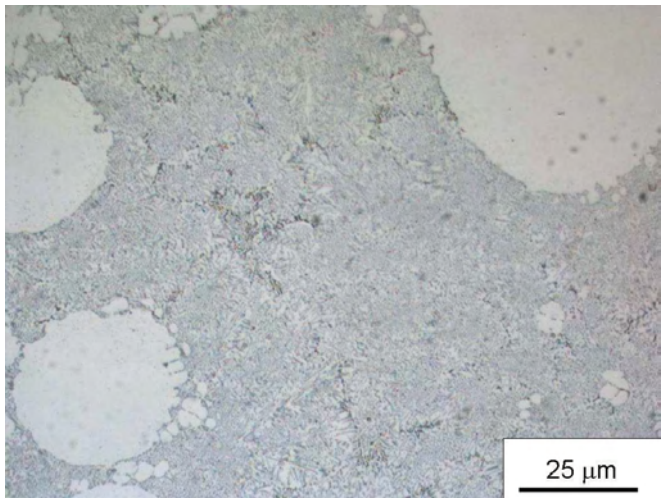

14 ppm Sr (MR = 5)

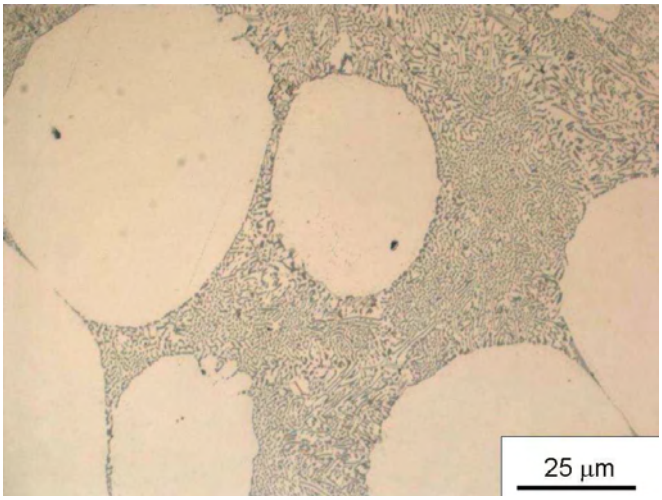

200 ppm Sr (MR = 5)

Figure 4.6: As-cast microstructures (including MR numbers from Table 2.2) of SSM-HPDC Al-7Si-Mg alloys with increasing Sr contents.

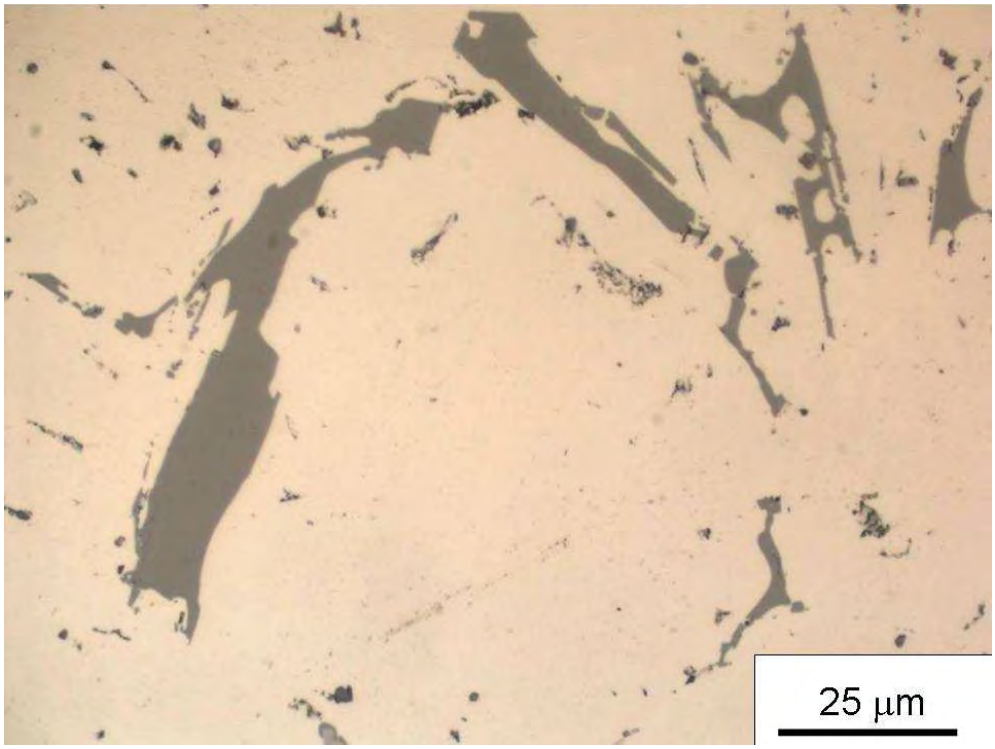

Figure 4.7: Microstructure with MR = 1 (Table 2.2) of rheoprocessed only (not HPDC) alloy with 14 ppm Sr following air cooling from the semi-solid temperature.

Modification of the eutectic component enables rapid spheroidisation of the silicon particles during solution treatment. Figure 4.8 shows microstructures of SSM-HPDC Al-7Si-Mg alloys with 2, 14 and 200 ppm Sr respectively after solution treatment at 540^{o}C for 1 h. Statistical analysis of the eutectic Si-particles in these samples is presented in Table 4.3.

Table 4.3: Statistical analysis of diameter and aspect ratio of eutectic Si in solution treated (540^{o}C-1h) SSM-HPDC Al-7Si-Mg alloys with 2, 14 and 200 ppm Sr.

	Diameter (µm)			Aspect ratio		
	2 ppm	**14 ppm**	**200 ppm**	**2 ppm**	**14 ppm**	**200 ppm**
Mean	1.36	1.13	1.24	1.73	1.58	1.54
Std.Dev	0.83	0.80	0.84	1.5	0.79	1.0
Samples	840	1057	420	840	1057	420

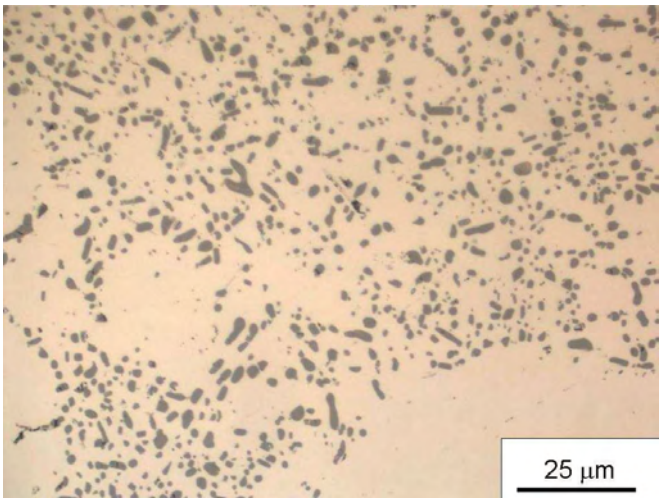

2 ppm Sr

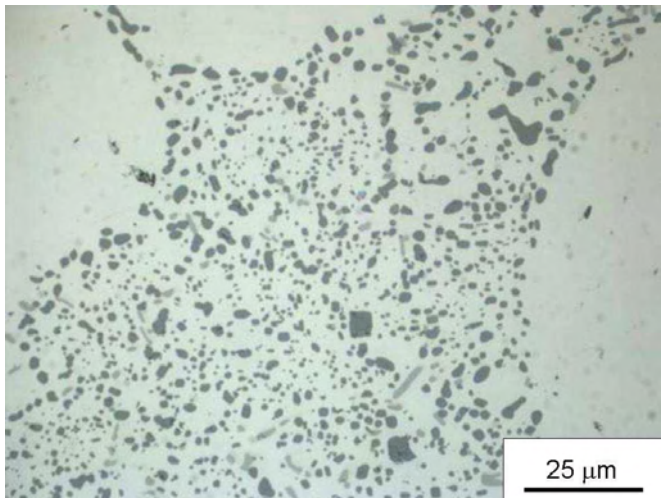

14 ppm Sr

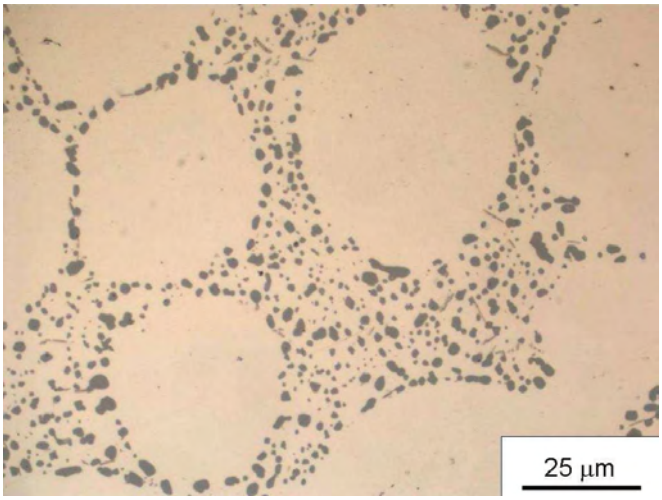

200 ppm Sr

Figure 4.8: Optical micrographs of solution treated (at 540^{o}C for 1 h) SSM-HPDC Al-7Si-Mg alloys with 2 ppm Sr, 14 ppm Sr and 200 ppm Sr.

It is seen that spheroidisation of the eutectic silicon particles occurred in all the alloys with a decrease in the aspect ratio (Table 4.3).

No spheroidisation of the eutectic silicon particles occurred at 540^{o}C in the rheoprocessed-only (no HPDC) alloy with 14 ppm Sr, even after 4 h at 540^{o}C (Fig. 4.9).

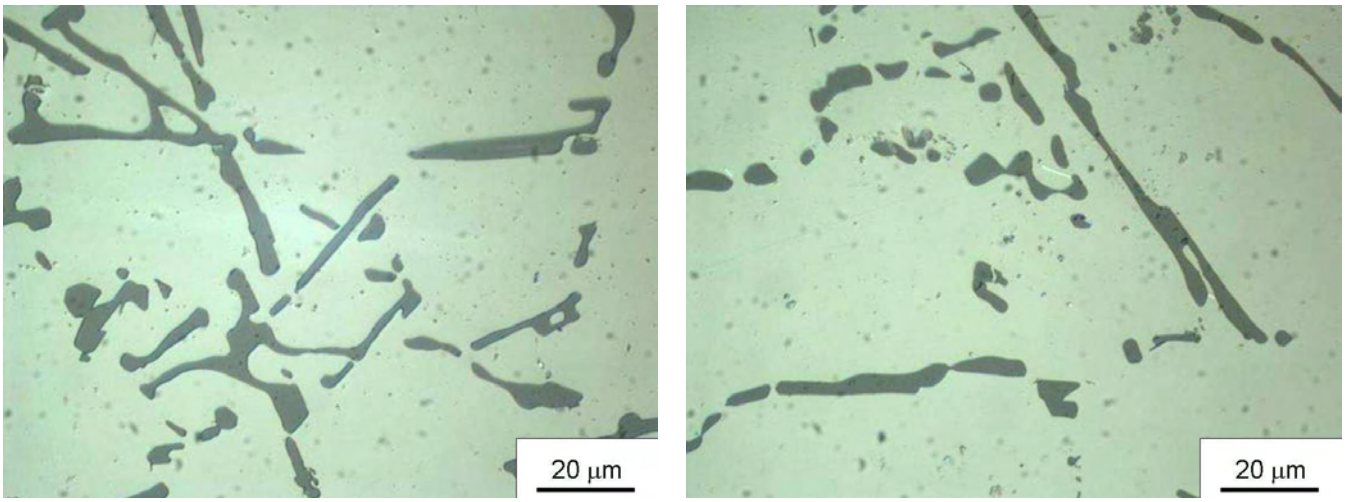

540°C-1h **540°C-4h**

Figure 4.9: Microstructures after solution treatment at 540°C for rheoprocessed-only (no HPDC) alloy with 14 ppm Sr.

The chronology of the spheroidisation of eutectic Si particles of SSM-HPDC Al-7Si-Mg alloys (with 200 ppm Sr) is shown in Fig. 4.10. Statistical analysis of the coarsening of the Si-particles in the eutectic after solution treatment at 540°C is presented in Table 4.4.

Table 4.4: Statistical analysis of the diameter (in µm) of eutectic Si particles after solution treatment at 540°C in SSM-HPDC Al-7Si-Mg alloys

	30 min	1 h	2 h	6 h	24 h
Mean	1.12	1.24	1.41	1.64	2.05
Std. Dev	0.74	0.84	0.89	1.21	1.50
Samples	582	420	278	427	280

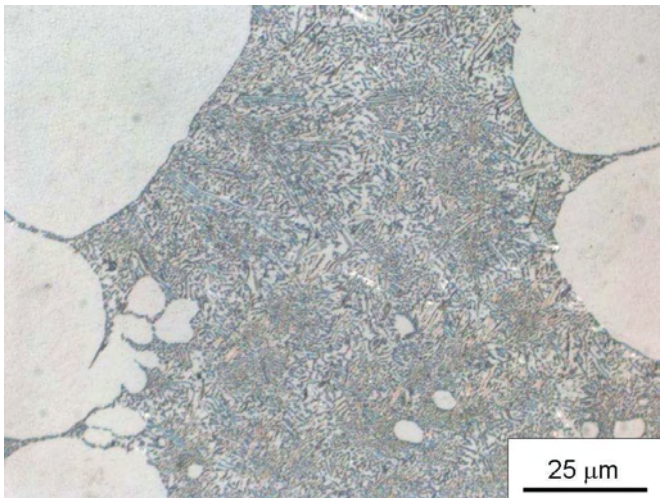

As-cast (MR = 5)

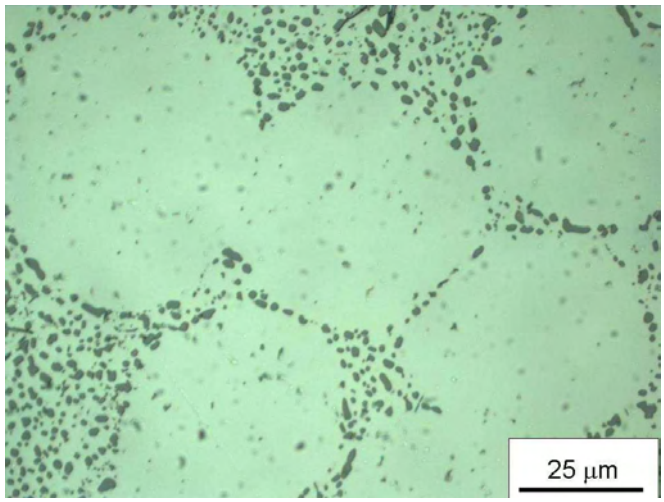

30 min – 540°C

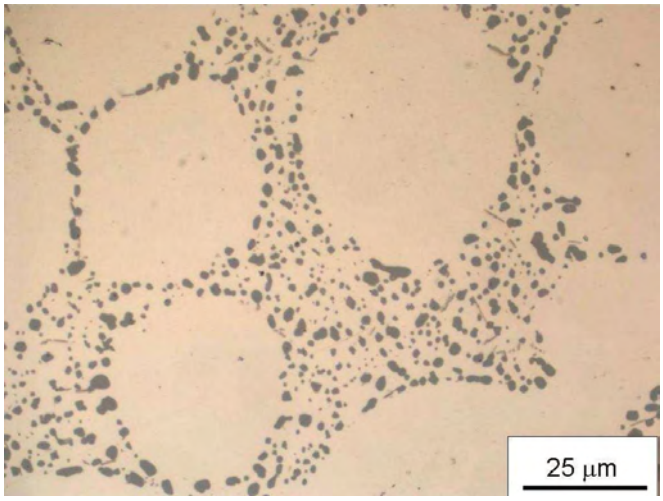

1 h – 540°C

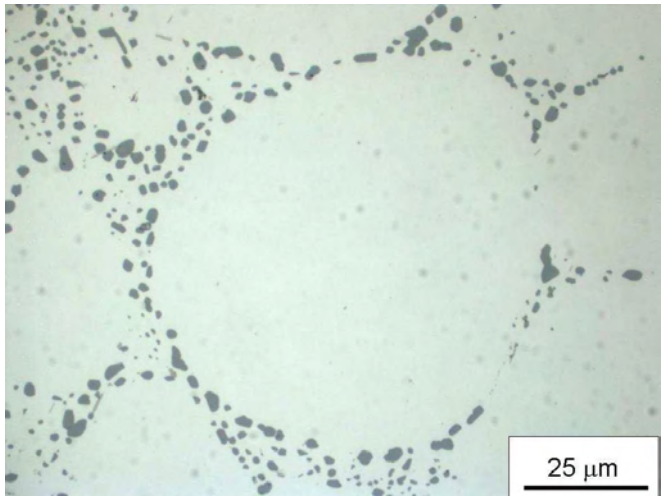

2 h – 540°C

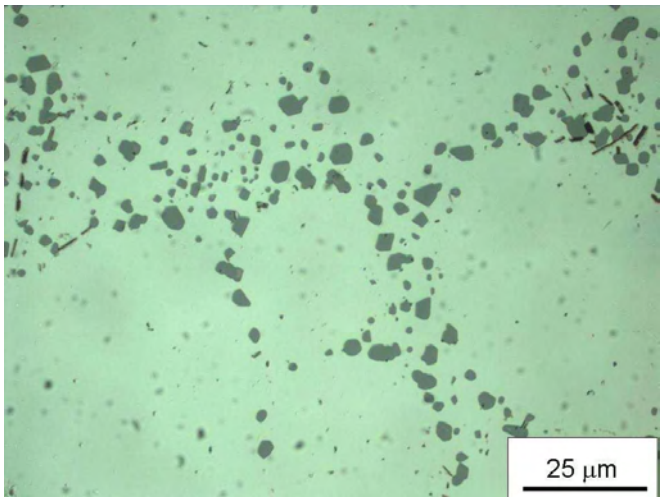

6 h – 540°C

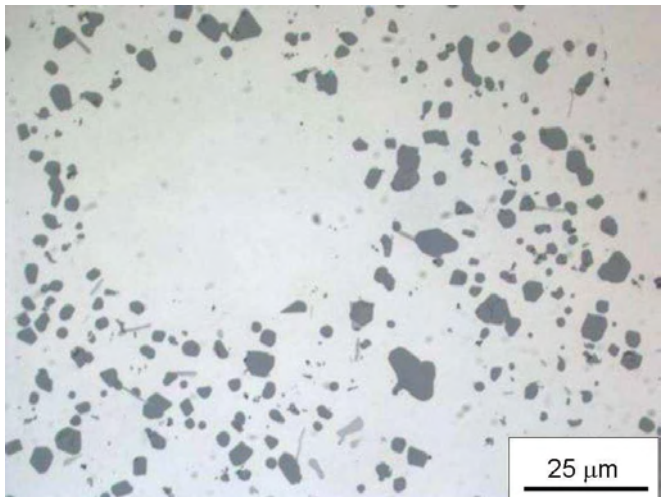

24 h – 540°C

Figure 4.10: Chronology of spheroidisation of the eutectic silicon particles after solution treatment at 540°C of SSM-HPDC Al-7Si-Mg alloys containing ~ 200 ppm Sr.

The cube of the change in mean diameter of the Si eutectic particles (D^3-D_o^3, where D_o = 0.86 μm in Table 4.2) is in reasonable direct proportion to solution treatment time (Fig. 4.11). Therefore, the growth process of the eutectic silicon particles during solution treatment is described by the Lifshitz-Slyozov-Wagner (LSW) theory of Ostwald ripening [6,69,102].

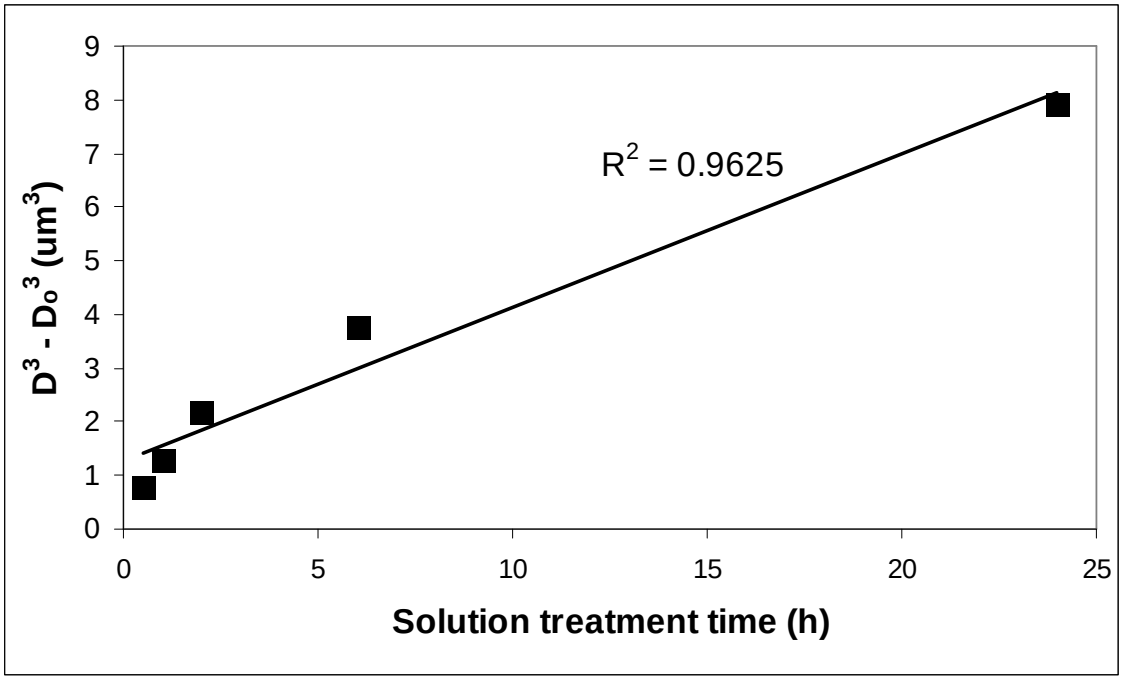

Figure 4.11: The cube of the change in mean diameter of the Si eutectic particles as a function of solution treatment time at 540°C using as starting diameter (D_o) of as-cast fibrous Si.

4.2.2. Dissolution of solutes and reduction of microsegregation

The time necessary to place magnesium in solid solution (dissolve the Mg_2Si in the alloy) is rapid at 540°C and occurs within minutes (section 2.3.1). However, it is frequently specified that solution treatments for these alloys at 540°C should be for 4-10 h (Table 2.8). Artificial aging curves (Fig. 4.12) indicate that similar levels of strengthening can be obtained following solution treatment at 540°C for either 1 or 6 h [HM1-HM3].

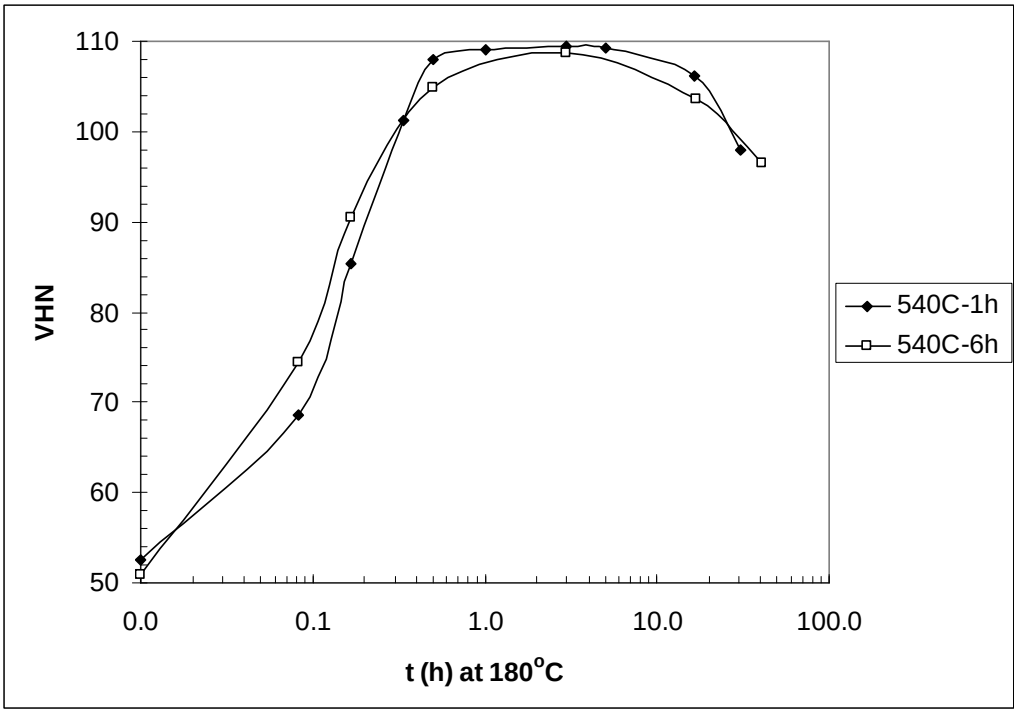

Figure 4.12: Artificial aging curves for SSM-HPDC A356 (0.34% Mg) following solution treatment at 540°C for 1 or 6 h (no natural pre-aging).

Tensile results (Table 4.5) of alloy F357 with 0.62% Mg (Table 3.1) confirm these observations, indicating that even in the higher Mg-containing alloys, a solution treatment of 1 h at 540°C is sufficient to obtain maximum strength [HM8].

Table 4.5: Yield strength (YS), ultimate tensile strength (UTS) and % elongation after fracture of heat treated SSM-HPDC F357 (0.62% Mg) samples. The standard deviation from five values for tensile properties is also indicated in brackets

Heat treatment	YS (MPa)	UTS (MPa)	% Elongation
T4			
540°C-0.5h, 120h NA	170 (3.4)	294 (4.4)	14.6 (2.0)
540°C-1h, 120h NA	172 (4.7)	297 (4.0)	17.0 (2.5)
540°C-6h, 120h NA	172 (1.9)	290 (4.1)	14.2 (0.7)
T6			
540°C-0.5h, 20h NA, 180°C-4 h	304 (2.2)	353 (1.3)	7.8 (1.4)
540°C-1h, 20h NA, 180°C-4 h	312 (4.1)	355 (3.9)	6.0 (1.3)
540°C-6h, 20h NA, 180°C-4 h	317 (4.9)	354 (5.2)	5.6 (1.4)

4.2.3. Impact strength

The impact strength of SSM-HPDC Al-7Si-Mg alloys with different Mg-contents that had been solution treated at 540°C for either 1 or 6 h were determined using a Zwick impact tester with a 40 kpcm hammer [HM3]. The impact strength in the T4 and T6 temper conditions was determined and is shown in Table 4.6. Similar impact properties are obtained after a solution treatment of 1 h rather than 6 h for each composition. There is therefore no advantage to impact strength by employing a longer solution treatment time of 6 h. The strength of the alloy plays a more important role than the solution treatment time on the impact strength in the T4 and T6 temper conditions. Linear relationships are found between impact strength and YS (Fig. 4.13(a) and UTS (Fig. 4.13(b)) regardless of whether the solution treatment was performed for 1 or 6 h. The alloys with lower strength have better impact properties because crack propagation is more difficult in these materials due to blunting, which would suggest that a better correlation between impact strength and UTS (rather than YS) should be found. The reason why a better correlation with UTS is not found in this case is most likely related to the fact that UTS is influenced significantly more by small casting defects than YS [103]. Note that Figure 4.13 is only applicable to alloys in the T4 and T6 temper conditions where spheroidisation of the Si has taken place.

The impact properties of alloys in the F and T5 temper conditions (where the eutectic Si particles are not spheroidised) are discussed later in section 4.8.

Also included in Fig. 4.13 are unit total energies (UTE) for premium strength cast A356/7 alloys obtained using tear testing [94]. Although tear testing is considered a more appropriate technique to measure fracture properties of Al-alloys than Charpy testing [94], the UTE values are reasonably comparable to the impact strength values determined in this study.

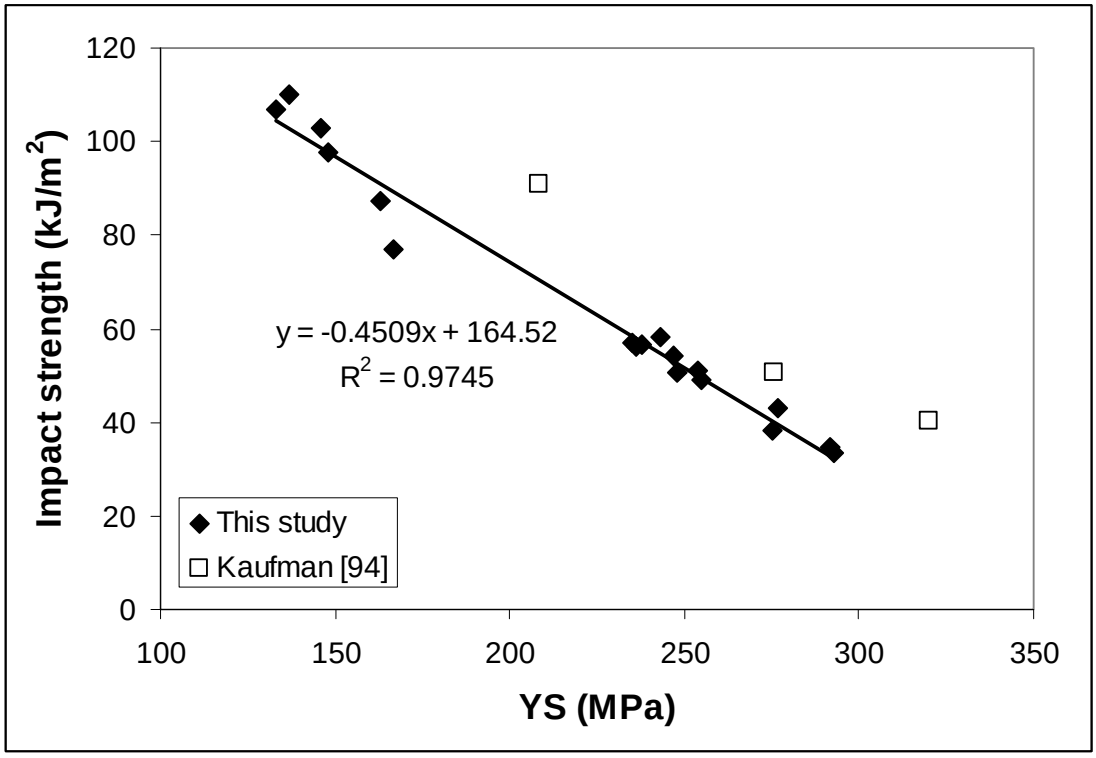

(a)

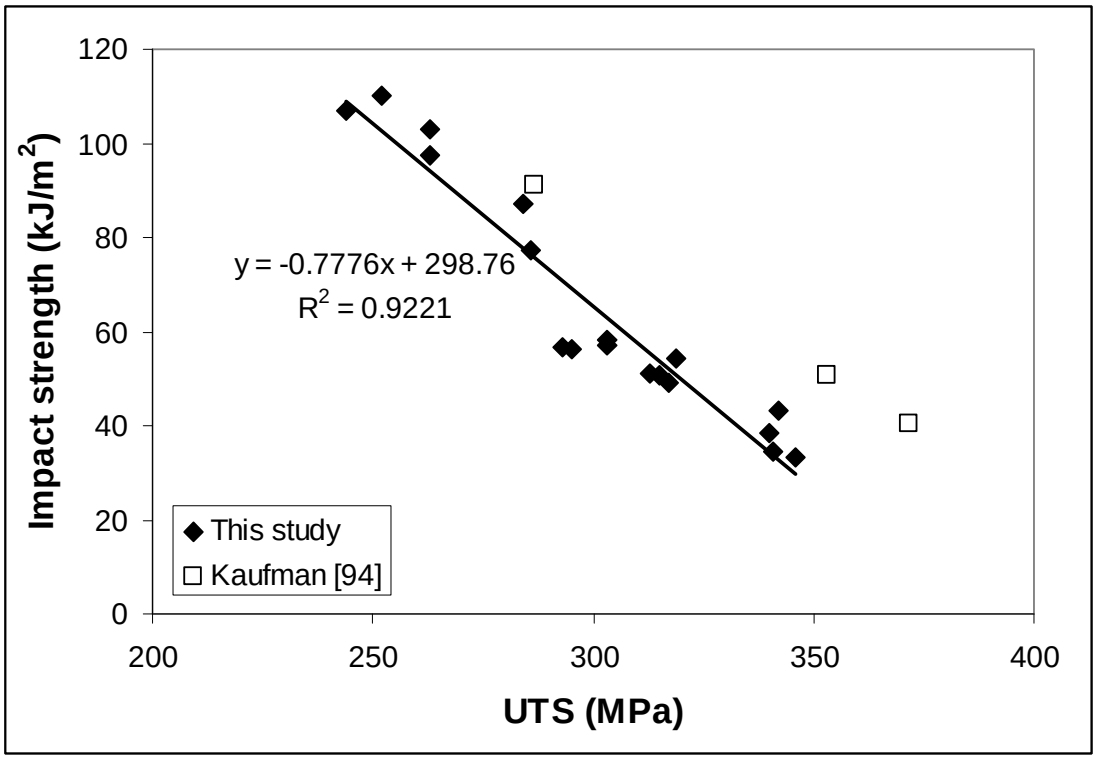

(b)

Figure 4.13: Impact strength of SSM-HPDC Al-7Si-Mg alloys in the T4 and T6 temper conditions as a function of (a) YS and (b) UTS of the alloys. UTE values from tear testing from Kaufmann [94] are also included.

Table 4.6: Impact strength of T4 and T6 heat treated samples of Al-7Si-Mg alloys (standard deviation from five values is also indicated in brackets).

Heat treatment	Impact Strength (kJ/m^2)
T4	
0.25% Mg	
540^{o}C,1 h	110.0 (3.7)
540^{o}C, 6 h	106.9 (9.1)
0.31% Mg	
540^{o}C,1 h	103.0 (5.5)
540^{o}C, 6 h	97.6 (6.0)
0.45% Mg	
540^{o}C,1 h	87.3 (6.4)
540^{o}C,6 h	77.1 (4.7)
T6	
0.25% Mg	
540^{o}C-6h, 0h NA,180^{o}C-1h	56.5 (6.7)
540^{o}C-1h, 0h NA, 180^{o}C-1h	57.0 (2.4)
540^{o}C-6h, 20h NA, 180^{o}C-4h	56.1 (4.1)
540^{o}C-1h, 20h NA, 180^{o}C-4h	58.3 (1.6)
0.31% Mg	
540^{o}C-6h, 0h NA, 180^{o}C-1h	50.6 (2.3)
540^{o}C-1h, 0h NA, 180^{o}C-1h	54.1 (3.0)
540^{o}C-6h, 20h NA, 180^{o}C-4h	49.1 (6.7)
540^{o}C-1h, 20h NA, 180^{o}C-4h	50.9 (4.3)
0.45% Mg	
540^{o}C-6h, 0h NA, 180^{o}C-1h	38.3 (3.8)
540^{o}C-1h, 0h NA, 180^{o}C-1h	43.0 (0.7)
540^{o}C-6h, 20h NA, 180^{o}C-4h	33.4 (2.6)
540^{o}C-1h, 20h NA, 180^{o}C-4h	34.6 (2.0)

4.3. Quench after solution treatment

Slow quench rates after the solution heat treatment can reduce the problems of distortion and residual stresses, but also result in a loss of strength and hardness after artificial aging (section 2.3.2). Natural (Fig. 4.14) and artificial (Fig. 4.15) aging curves for SSM-HPDC A356 with 0.36% Mg (Table 3.1) are shown for samples that were solution treated at 540^{o}C for 1 h and then quenched in water (WQ) at either 25 or 70^{o}C [HM3]. Artificial aging was performed at 180^{o}C.

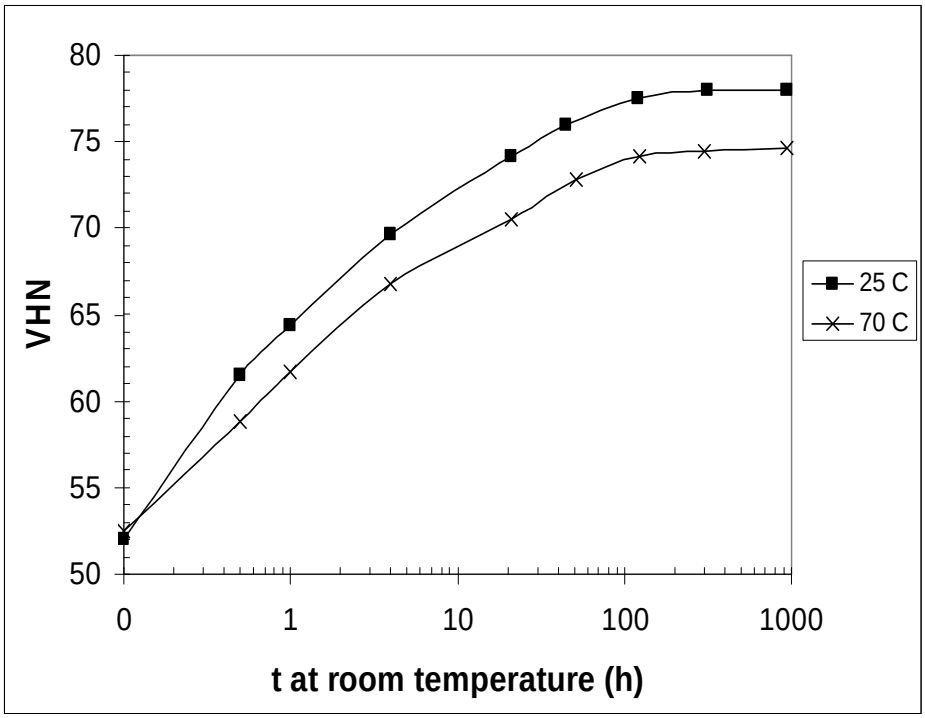

Figure 4.14: Natural aging curves for SSM-HPDC A356 solution treated at 540^{o}C for 1 h, followed by water quenching at 25 and 70^{o}C.

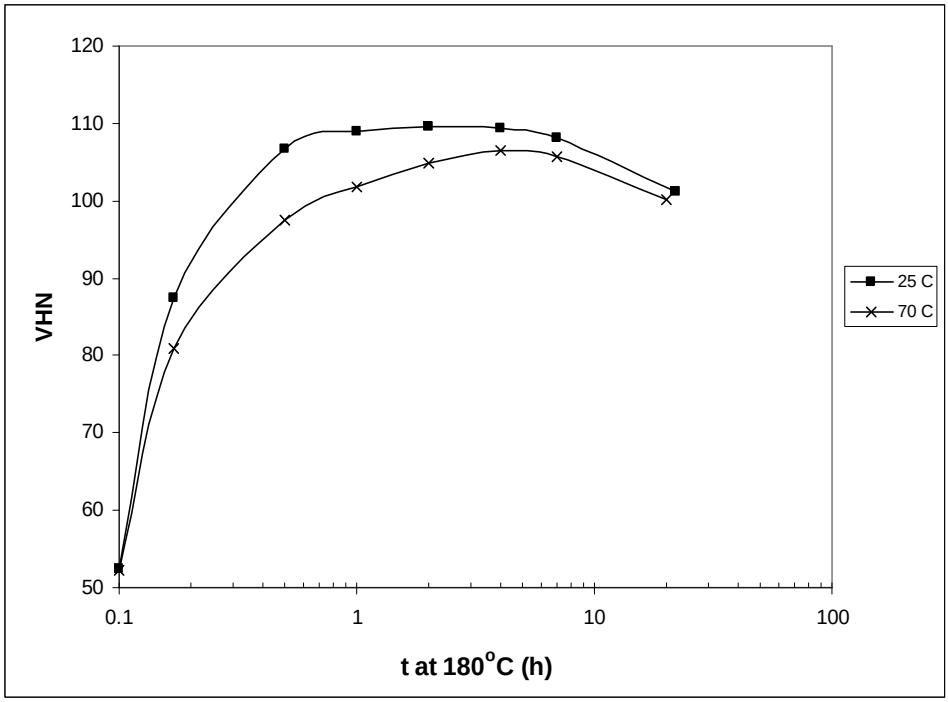

Figure 4.15: Artificial aging curves at 180°C for SSM-HPDC A356 solution treated at 540°C for 1 h, followed by water quenching at 25 and 70°C and artificial aging at 180°C.

It is seen that the higher quench temperature leads to a lower T4 hardness due to less supersaturation (Fig. 4.14). The more sluggish artificial aging response following the 70°C quench is presumably due to less quenched in vacancies (Fig. 4.14). The peak hardness (VHN = 106) is slightly less than when a 25°C water quench is used. This is most likely due to a lower degree of supersaturation obtained after the 70°C water quench. The tensile properties of SSM-HPDC A356 (0.40% Mg) in the T4 and T6 temper conditions are compared in Table 4.7 for samples quenched in 25 and 70°C water respectively. As expected, the YS and UTS of the 70°C water quenched alloys are less than the 25°C water quenched alloys.

Table 4.7: YS, UTS, % elongation after fracture of T4 and T6 heat treated SSM-HPDC samples (0.40wt% Mg-A356). The standard deviation from five values for tensile properties is also indicated in brackets.

Heat Treatment	YS (MPa)	UTS (MPa)	% Elongation
T4			
540°C-1h, 25WQ, 120h NA	152 (3.5)	282 (6.1)	15.8 (3.3)
540°C-1h, 70WQ, 120h NA	138 (2.2)	264 (6.5)	16.5 (2.5)
T6			
540°C-1h,25WQ,0h NA,180°C-4h	276 (8.0)	342 (4.9)	9.1 (1.2)
540°C-1h,70WQ,0h NA,180°C-4h	265 (5.0)	330 (2.7)	9.8 (2.1)
540°C-1h,25WQ,120h NA,180°C-4h	280 (5.2)	337 (6.0)	6.9 (1.8)
540°C-1h,70WQ,120h NA,180°C-4h	265 (3.5)	327 (4.5)	8.6 (0.7)

4.4. Natural aging and the T4 temper

Natural aging time is the time a component is stored at room temperature after the solution heat treatment and quench. The precipitation hardening that result from natural aging alone (no artificial aging) produces the T4 temper. Figure 4.16 shows natural aging curves for SSM-HPDC Al-7Si-Mg alloys after solution treatment at 540°C for 1 h, followed by a water quench (25°C) before natural aging [HM1].

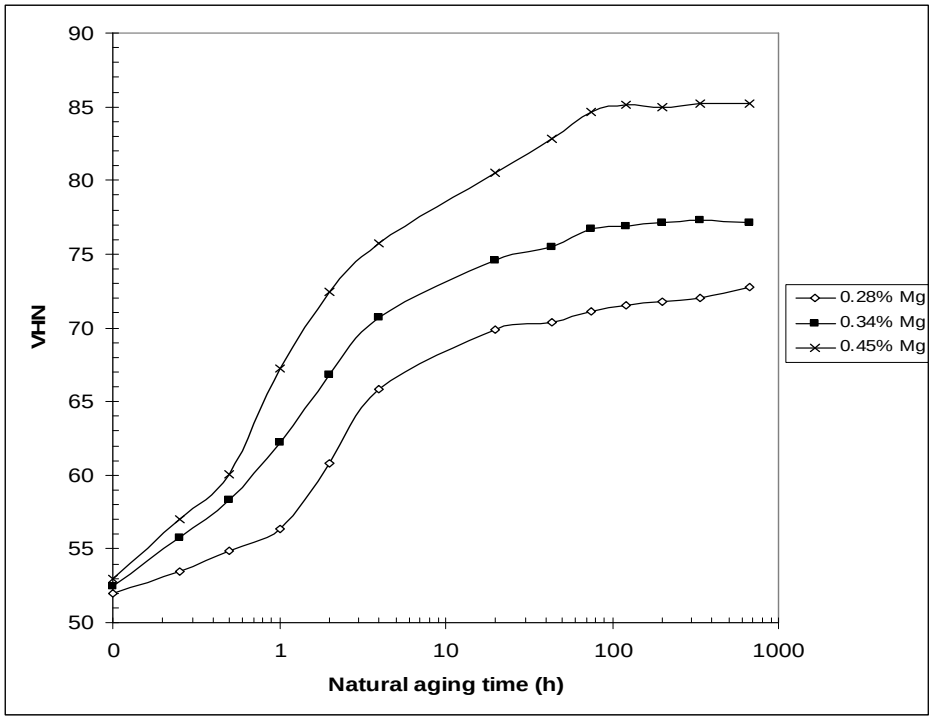

Figure 4.16: Natural aging curves for SSM-HPDC Al-7Si-Mg alloys following solution treatment at 540^{o}C for 1 h and a 25^{o}C water quench.

The alloy is relatively soft immediately after quenching (VHN = ~ 53), but thereafter the hardness increases rapidly and eventually levels out after about 120 h corresponding to the stable T4 temper. The natural aging response of these alloys is considered to be due to the forming of (Mg+Si) clusters (see APT results in section 4.14). The tensile properties of SSM-HPDC Al-7Si-Mg alloys with different Mg-contents are shown in Table 4.8.

Table 4.8: YS, UTS, % elongation after fracture of T4 heat treated SSM-HPDC Al-7Si-Mg alloys (solution treated at 540°C-1 h, 25°C water quench and natural aging for at least 120 h). The standard deviation from five values for tensile properties is also indicated in brackets.

Mg-content (wt%)	YS (MPa)	UTS (MPa)	% Elongation
0.25	137 (4.2)	252 (6.2)	20.2 (0.94)
0.31	146 (7.3)	263 (8.8)	17.4 (1.8)
0.38	152 (2.1)	268 (3.9)	14.5 (1.3)
0.40	152 (3.5)	282 (6.1)	15.8 (3.3)
0.45	163 (1.5)	284 (2.6)	16.5 (1.9)
0.62	172 (4.7)	297 (4.0)	17.0 (2.5)

4.5. Artificial aging and the T6 temper

Artificial aging is performed at temperatures above room temperature to cause precipitation of strengthening phases. Artificial aging curves at artificial aging temperatures of 160, 180 and 190°C are shown in Fig. 4.17 [HM2]. The curves were determined for samples that were solution treated at 540°C for 6 h, water quenched and naturally aged for 20 h before artificial aging. As expected, the maximum hardness is reached in a shorter time as aging temperatures are increased due to higher diffusion rates. However, the maximum hardness achieved simultaneously decreases slightly, due to the higher solubility and hence lower supersaturation, leading to a lower nucleation rate and volume fraction of strengthening phases at higher aging temperatures. The optimum artificial aging parameters depend on the properties required. If a high hardness (strength) is required, a low aging temperature is required (such as 160°C), but this unfortunately takes relatively long times to obtain this high hardness (Fig. 4.17). The best combination of relatively short aging treatments resulting in acceptably high hardness values is obtained by aging at 170-180°C. If a short aging time is, however, a more important factor than maximum hardness (strength), then 185-195°C will give optimum results.

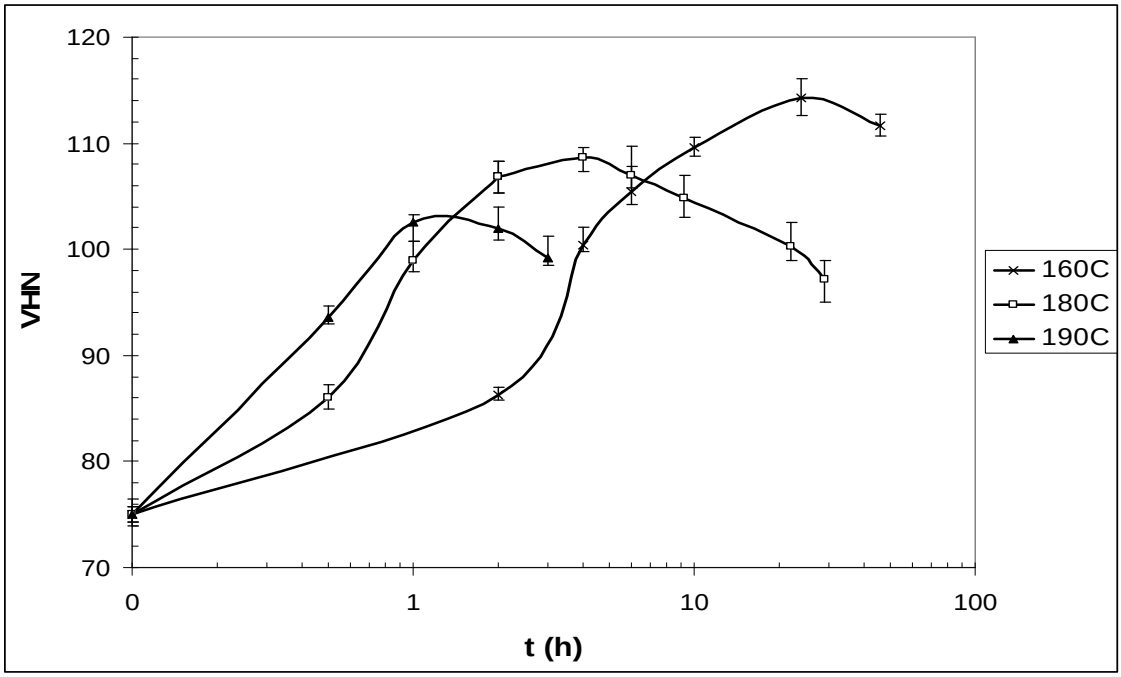

Figure 4.17: Artificial aging curves for alloy A356 (0.36% Mg) after solution treatment at 540°C for 6 h, water quenching, natural aging for 20 h and artificial aging at different temperatures.

Artificial aging curves at 180°C for alloy A356 (with 0.36 wt% Mg), following natural aging periods of either 0, 1, 20 or 120 h, are shown in Fig. 4.18 [HM4]. When no prior natural aging is applied, the initial artificial aging response is rapid. The converse is also true - when natural aging is employed, the subsequent artificial aging response is sluggish. Natural aging of only 1 h decreases the artificial aging response of this alloy significantly.

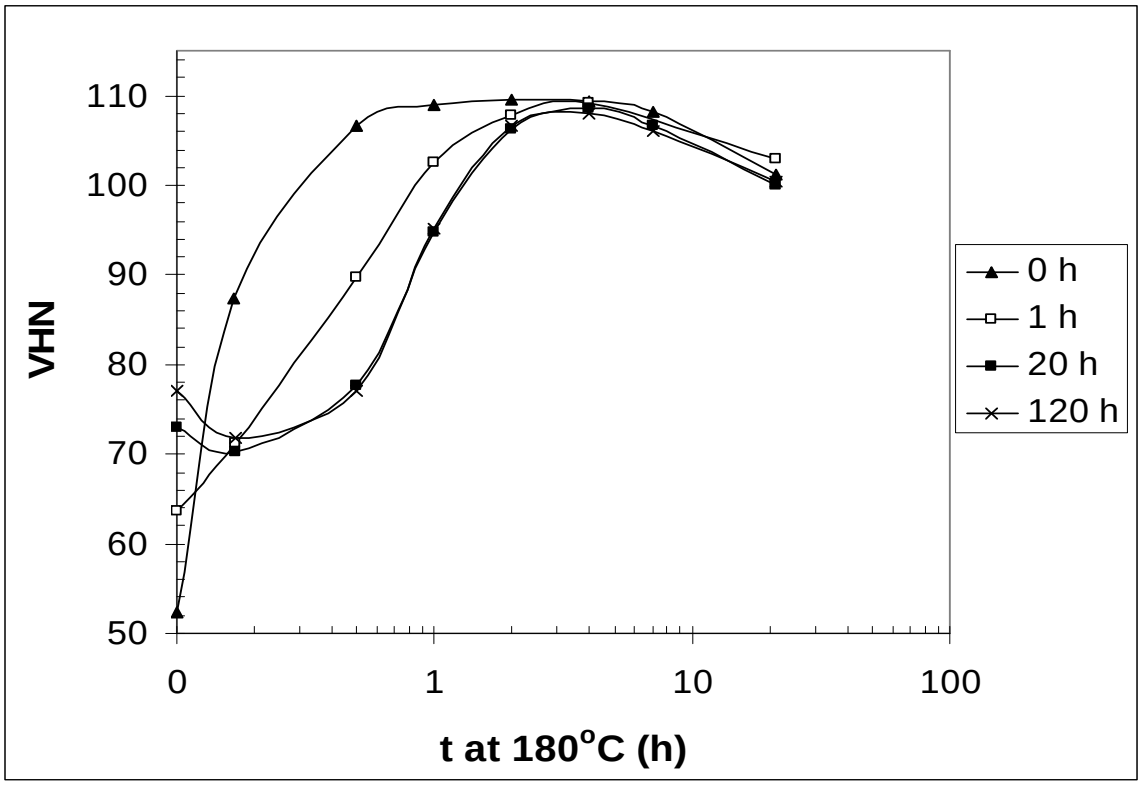

Figure 4.18: Artificial aging curves at 180°C after natural aging for times of 0, 1, 20 and 120 h respectively for A356 with 0.36wt% Mg.

This phenomenon can be explained by two different mechanisms. Firstly, it has been shown that the precipitates which grow during artificial aging from the clusters are coarser than those that develop in certain 6000 series alloys aged immediately after quenching. This results in a reduction of up to 10% in tensile properties for certain alloys [9]. Secondly, it has been shown that natural aging following the solution treatment reduced the age hardenability of Al-Mg-Si wrought alloy 6016, especially in the under-aged condition [104]. This was attributed to solute clustering during natural aging, and the subsequent dissolution of these clusters during artificial aging. The extent of the loss was, however, recovered by precipitation of β″–particles upon further aging.

Considering Fig. 4.18, it is seen that for alloy A356, the hardness values of naturally aged samples are also recovered with further artificial aging. The mechanism of the formation of coarser precipitates that leads to a decrease in tensile properties does not allow for a full recovery in hardness. It is also seen from Fig. 4.18 that the hardness of the sample that did not age naturally increases immediately during artificial aging.

However, the samples that were naturally aged soften during the first 10 minutes at 180^{o}C, before the hardness increases again. The clusters that form during natural aging and their response during artificial aging are shown in detail in the APT results in section 4.14.

When no natural pre-aging occurs, a plateau is maintained once the maximum hardness is reached during artificial aging after about 1 to 5 h (Fig. 4.18). This differs from when natural pre-aging occurs, when a hardness peak is observed after approximately 4 h. The tensile properties (YS and UTS) are shown Table 4.9 as a function of the artificial aging time within the hardness plateau (with no prior natural aging). It is seen that the ultimate tensile strengths of the samples on the hardness plateau are similar. However, the yield strength of the 1 hour artificially aged sample is significantly lower than the rest of the samples with a concurrent higher ductility. The hardness plateau allows more freedom in terms of the artificial aging times that can be used and the dangers of either under-aging or over-aging are therefore minimised. Once natural aging occurs, a hardness plateau is not maintained during the subsequent artificial aging. Instead, a hardness peak is reached after approximately 4 h (Fig. 4.18). This would necessitate stricter control in terms of artificial aging time (i.e. aging for less than 4 h will result in under-aging, and aging for more than 4 h will result in over-aging). The tensile properties after artificial aging for 4 h at 180^{o}C as a function of prior natural aging time are also shown in Table 4.9. In this case, no significant differences are seen in either the yield strength or ultimate tensile strength. The influence of natural aging prior to artificial aging can therefore be removed by a 4 h, 180^{o}C artificial aging treatment. It is seen from Fig. 4.18 that, while artificial aging at 180^{o}C for 1 h causes maximum hardening in SSM-HPDC A356 that was not naturally aged, under-aging is achieved in samples that were naturally aged prior to artificial aging. The tensile properties of 0.40wt% Mg-A356 were determined under these conditions (1 h artificial aging at 180^{o}C for samples that were naturally aged for 0 h, 20 h and 120 h). The negative influence of natural aging on the initial stages of artificial aging can be seen in Table 4.9. Similar effects to those observed for SSM-HPDC A356 in Table 4.9 have also been found for the higher Mg-containing (0.62%) SSM-HPDC alloy F357 and are presented in Table 4.10 [HM8].

Table 4.9: Yield strength (YS), UTS and % elongation after fracture of SSM-HPDC A356. The standard deviation from five values for tensile properties is also indicated in brackets.

Heat treatment	YS (MPa)	UTS (MPa)	% Elongation
0.36wt% Mg			
540°C-1h,0h NA,180°C-1h	255 (4.8)	330 (6.4)	10.4 (2.5)
540°C-1h,0h NA,180°C-2h	269 (8.5)	334 (6.8)	7.5 (1.9)
540°C-1h,0h NA,180°C-4h	273 (6.5)	333 (8.4)	8.4 (2.1)
540°C-1h,0h NA,180°C-5h	273 (3.1)	328 (6.9)	7.7 (3.1)
540°C-1h,1h NA,180°C-4h	269 (5.8)	325 (4.6)	10.3 (3.4)
540°C-1h,20h NA,180°C-4h	270 (4.7)	325 (2.8)	9.3 (1.7)
540°C-1h,120h NA,180°C-4h	270 (5.5)	328 (5.8)	8.0 (2.2)
0.40wt% Mg			
540°C-1h,0h NA,180°C-1h	266 (7.5)	341 (9.5)	7.8 (1.8)
540°C-1h,20h NA,180°C-1h	224 (7.5)	315 (3.4)	12.5 (1.4)
540°C-1h,120h NA,180°C-1h	233 (8.2)	318 (5.2)	10.0 (2.7)
540°C-1h,-18°C for 20h,180°C-1h	266 (6.7)	343 (4.7)	9.1 (1.9)

Table 4.10: Yield strength (YS), ultimate tensile strength (UTS) and % elongation after fracture of SSM-HPDC F357 (0.62% Mg). The standard deviation from five values for tensile properties is also indicated in brackets

Heat treatment	YS (MPa)	UTS (MPa)	% Elongation
540°C-1h,0h NA,180°C-1h	296 (2.9)	358 (3.7)	7.4 (0.7)
540°C-1h,0h NA,180°C-2h	307 (3.1)	364 (2.5)	9.6 (2.4)
540°C-1h,0h NA,180°C-4h	315 (5.2)	360 (5.0)	5.7 (1.1)
540°C-1h,20h NA,180°C-1h	243 (6.2)	320 (7.9)	9.5 (2.6)
540°C-1h,20h NA,180°C-2h	289 (10.7)	346 (4.5)	8.0 (2.4)
540°C-1h,20h NA,180°C-4h	312 (4.1)	355 (3.9)	6.0 (1.3)

To determine whether the process of natural aging could be impeded by low temperatures, SSM-HPDC A356 samples were stored in a freezer at -18°C for 20 h after quenching, before artificial aging at 180°C for 1 h. The tensile properties (Table

4.9) indicate that this treatment was indeed successful. The artificial aging response of the samples that were kept in the freezer was the same as the samples that were not naturally aged at all. However, it would be more practical to remove the influence of natural pre-aging by employing an artificial aging treatment of 180^{o}C for 4 h.

The onset of the hardness plateau (no natural aging) and hardness peak (with natural aging) in Fig. 4.18 as a function of artificial aging temperature follows an Arrhenius-type response (t_{T6} = C EXP (Q/RT)) with C the pre-exponential factor, Q the activation energy in J/mol and R the universal gas constant = 8.314 J/mol K). The equations that describe the time-to-maximum-hardness (t_{T6}) are given by equation 4.2 (with prior natural aging time) and equation 4.3 (for no natural aging time) [HM2]:

$$\mathbf{t_{T6} = 2.3 \times 10^{-15} EXP\ (163000 / 8.314T)} \qquad \mathbf{(4.2)}$$

$$\mathbf{t_{T6} = 4.9 \times 10^{-16} EXP\ (163000 / 8.314T)} \qquad \mathbf{(4.3)}$$

with t_{T6} the time in seconds and T the artificial aging temperature in K.
Arrhenius-type plots are shown in Fig. 4.19 for the artificial aging of SSM-HPDC Al-7Si-Mg alloys with prior natural aging (Equation 4.2) and without prior natural aging (Equation 4.3). Comparing the equations and plots, it is seen that an instantaneous transfer from quench to artificial aging does not have an influence on the activation energy (Q). It does, however, decrease the pre-exponential factor C, thereby resulting in a much faster artificial aging response. These equations are useful for determining how long an SSM-HPDC Al-7Si-Mg component must be artificially aged at a specific temperature to get maximum hardness (for convenience the temperatures and times are shown in Table 4.11).

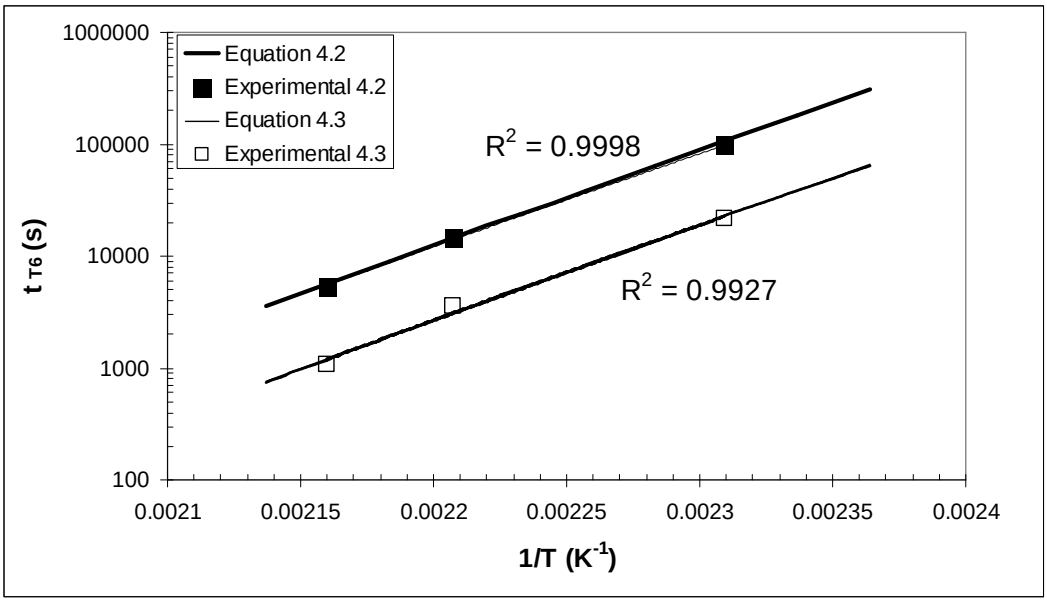

Figure 4.19: Arrhenius-type plots for the artificial aging of SSM-HPDC A356 with prior natural aging (Equation 4.2) and without prior natural aging (Equation 4.3).

The determined activation energy of 163 kJ/mol is higher than those reported by Rometsch and Schaffer [82] (130-138 kJ/mol) and Shercliff and Ashby [15] (130-145 kJ/mol) for Al-Si-Mg alloys. The activation energy for diffusion of Si in Al has been proposed in a range from 118 kJ/mol [105] to 151 kJ/mol [106]. Similarly, the activation energy for diffusion of Mg in Al has been proposed in a range from 111 kJ/mol [107] to 161 kJ/mol [108].

Table 4.11: Time-to-maximum-hardness (t_{T6}) at different artificial aging temperatures (using equations 4.2 and 4.3).

Temperature (^{o}C)	t_{T6} (with natural aging) (h)	t_{T6} (with no natural aging) (h)
160	29	6.5
165	18	4.0
170	10	2.5
175	6.5	1.5
180	4	1.0
185	2.5	0.5
190	1.5	0.3

Note that equation 4.3 (no natural pre-aging) calculates the onset of the hardness plateau (Fig. 4.18). As was shown in Tables 4.9 and 4.10, this does not necessarily result in maximum yield strength (i.e. time-to-maximum-hardness is not the same as time-to-maximum-yield strength). With equation 4.2 (with natural pre-aging), however, time-to-maximum-hardness and time-to-maximum-yield strength are the same. To ensure that maximum yield strength is reached in samples with no prior natural pre-aging, equation 4.2 should rather be used. According to Table 4.11, the traditional artificial aging temperature of 170^{o}C for 6 h (Table 2.7) results in under-aging of naturally pre-aged Al-7Si-Mg alloys, with over-aging of alloys that were not naturally pre-aged. This is not an ideal situation where different properties are obtained as a function of natural pre-aging (see Fig. 2.34). As discussed before, application of equation 4.2 will result in similar tensile properties being obtained regardless of natural pre-aging. Table 4.12 shows tensile properties of alloy F357 (with 0.62% Mg) after artificial aging at 170^{o}C for 6 and 10 h respectively [HM8]. It can be seen that higher strength (especially YS) is indeed obtained as predicted by Table 4.11.

Table 4.12: Yield strength (YS), ultimate tensile strength (UTS) and % elongation after fracture of heat treated F357 samples (0.62% Mg). The standard deviation from five values for tensile properties is also indicated in brackets.

Heat treatment	YS (MPa)	UTS (MPa)	% Elongation
540^{o}C-6h, 20h NA, 170^{o}C-6h	307 (5.7)	356 (4.8)	6.1 (1.5)
540^{o}C-6h, 20h NA, 170^{o}C-10h	320 (4.5)	358 (3.1)	5.8 (1.2)

The tensile properties of SSM-HPDC Al-7Si-Mg alloys heat treated with the traditional heat treatment (540^{o}C-6h, 20h NA, 170^{o}C-6h) are compared with those heat treated with the shortened cycles (540^{o}C-1h, 0-120h NA, 180^{o}C-4h) in Table 4.13. The tensile properties obtained using the traditional and short heat treatment cycles are remarkably similar over a wide range of Mg-compositions. The advantage of the shortened cycles is that it involves only 5 hours at elevated temperatures compared to 12 h with the traditional treatment, with obvious productivity increases and energy savings. The reason why similar properties can be obtained at the higher artificial aging temperature of 180^{o}C compared to 170^{o}C is due to the fact that the

180°C-4h treatment results in peak aging, whereas 170°C-6h results in under-aging (Table 4.11).

Table 4.13: Yield strength (YS), ultimate tensile strength (UTS) and % elongation after fracture of SSM-HPDC Al-7Si-Mg samples heat treated with the traditional or shortened heat treatments. The standard deviation from five values for tensile properties is also indicated in brackets.

Heat treatment	YS (MPa)	UTS (MPa)	% Elongation
0.28% Mg			
540°C-6h, 20h NA, 170°C-6h	243 (4.1)	296 (6.5)	7.2 (1.3)
540°C-1h, 0-120h NA, 180°C-4h	240 (2.8)	301 (3.1)	9.4 (0.9)
0.34% Mg			
540°C-6h, 20h NA, 170°C-6h	261 (4.5)	316 (5.9)	8.3 (2.1)
540°C-1h, 0-120h NA, 180°C-4h	259 (5.2)	317 (7.1)	8.8 (1.4)
0.45% Mg			
540°C-6h, 20h NA, 170°C-6h	297 (5.0)	345 (5.6)	7.3 (2.3)
540°C-1h, 0-120h NA, 180°C-4h	294 (5.8)	344 (3.1)	7.1 (1.4)
0.62% Mg			
540°C-6h, 20h NA, 170°C-6h	307 (5.7)	356 (4.8)	6.1 (1.5)
540°C-1h, 0-120h NA, 180°C-4h	312 (4.1)	355 (3.9)	6.0 (1.3)

4.6. The effects of Mg and Fe in Al-7Si-Mg alloys

The tensile properties of SSM-HPDC Al-7Si-Mg alloys from this study are compared in Fig. 4.20 with SSM-processed Al-7Si-Mg alloys from other researchers [35,89], all heat treated with the traditional T6 heat treatment cycles.

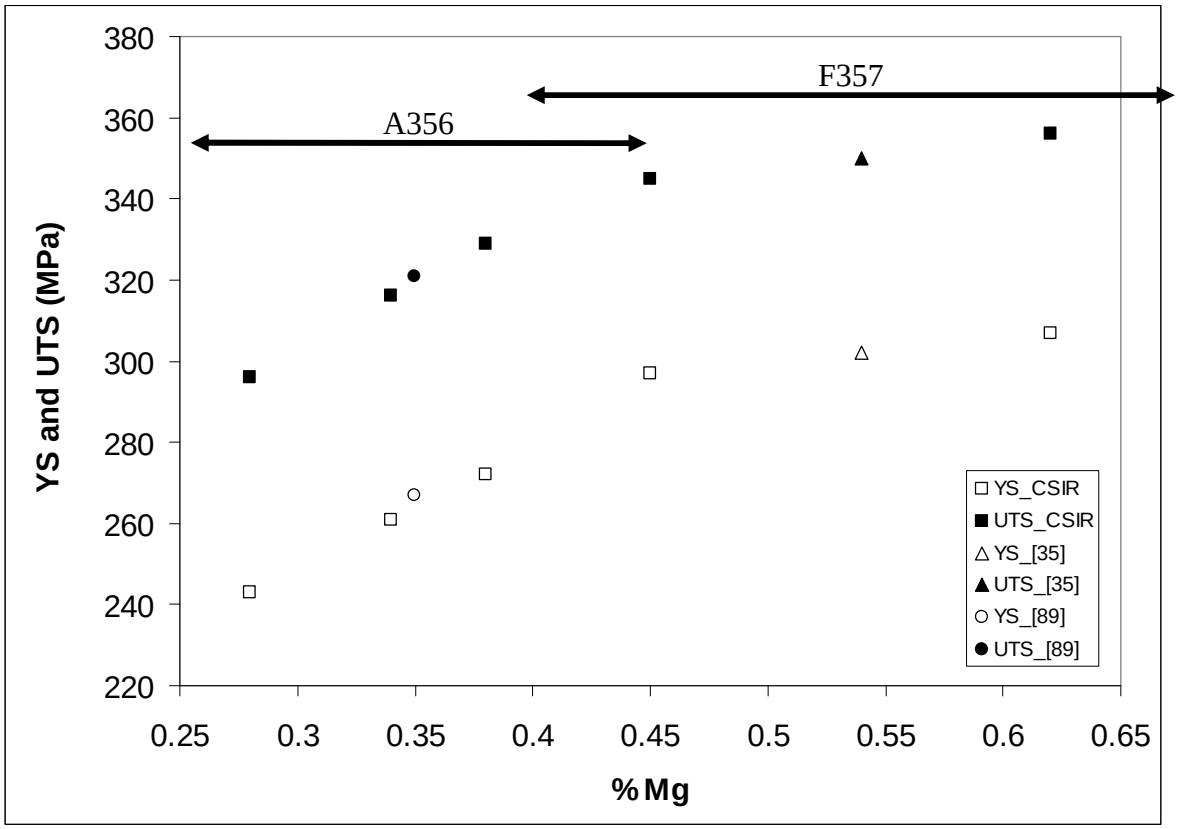

Figure 4.20: YS and UTS as a function of the bulk wt% Mg-content of SSM-processed Al-7Si-Mg alloys heat treated with the traditional heat treatment cycles.

A lower increase in strength with bulk Mg-concentration is observed for alloy F357 when compared to alloy A356. This is in line with the findings of Taylor and co-workers [48] who determined the matrix Mg-content of A356 and F357 alloys (the Mg-concentration in solid solution after solution treatment) by using electron probe microanalysis (EPMA) - as shown in Fig. 2.20. In the low Mg-alloys (A356), it is seen that the final matrix Mg concentration equals the bulk Mg-content of the alloy. This implies that, during solution treatment, all the as-cast Mg_2Si was dissolved, and that the π-$Al_8FeMg_3Si_6$ phase was also dissolved. As the alloy Mg-content increases, the matrix Mg-levels do not reach the bulk values. Since very little Mg_2Si is expected to remain after the solution treatment, this phenomenon is due to the increased stability of the π-phase as the alloy Mg-content is increased. Deviation from full dissolution of Mg in the matrix occurs at approximately 0.4% Mg. The calculated phase equilibria (minor phases) using Thermo-Calc for an Al-alloy with a base composition of alloy F357 with 0.62% Mg (Table 3.1), but with variable Mg, are

shown in Fig. 4.21 [HM8]. In this figure, the liquidus and solidus temperatures are indicated by arrows; "pi" refers to the π phase, "beta" is β–Al_5FeSi, and "alpha" is an Al-Mn-Fe-Si solid solution based on Al_8Fe_2Si (containing approximately equal amounts of Mn and Fe for the cases considered here). In all cases the major phases were liquid, Al-based FCC solid solution (the primary phase upon solidification), and Si (formed by eutectic solidification). In the region of the solution temperature (just below the solidus) the effect is quite clear: higher Mg levels increase the stability range of π to higher temperatures, and suppress β–Al_5FeSi formation at high temperatures. A secondary effect is that the dissolution temperature of Mg_2Si increases (and the equilibrium mass fraction of Mg_2Si at low temperatures increases), as one would expect. The extension of the stability range of the π-phase to high temperatures is in line with the observation that it is not possible to remove π by solution treatment in the high-Mg alloys above 0.4% in Fig. 2.20. According to the Thermo-Calc simulations, the dissolution temperature of π increases linearly with the Mg content of the alloy, and reaches 540°C at a Mg content of 0.40%.

Figs. 4.22(a,b) show scanning electron micrographs of SSM-HPDC A356 and F357 after solution treatment at 540^{o}C for 6 hours. The needle-like phase that is found in both A356 and F357 is tentatively identified by energy dispersive spectroscopy (EDS) (Fig. 4.23(a)) as likely to be β–Al_5FeSi. The blocky intermetallic phase that was mainly found in F357 is tentatively identified with EDS (Fig. 4.23(b)) as likely to be the Mg-containing π-phase ($Al_8FeMg_3Si_6$).

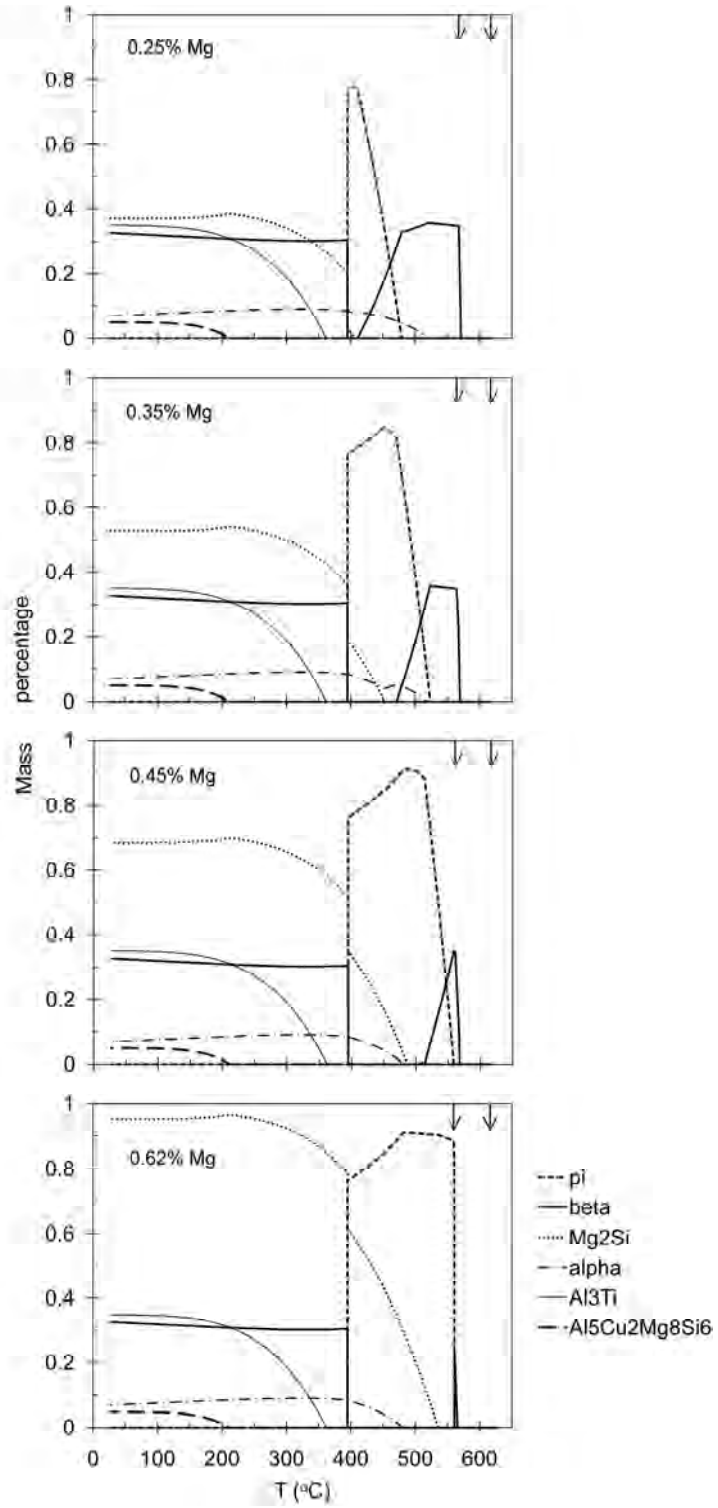

Figure 4.21: Calculated phase equilibria (minor phases) for Al alloy containing 7.01% Si, 0.10% Fe, 0.01% Cu, 0.01% Mn, 0.13% Ti and variable Mg.

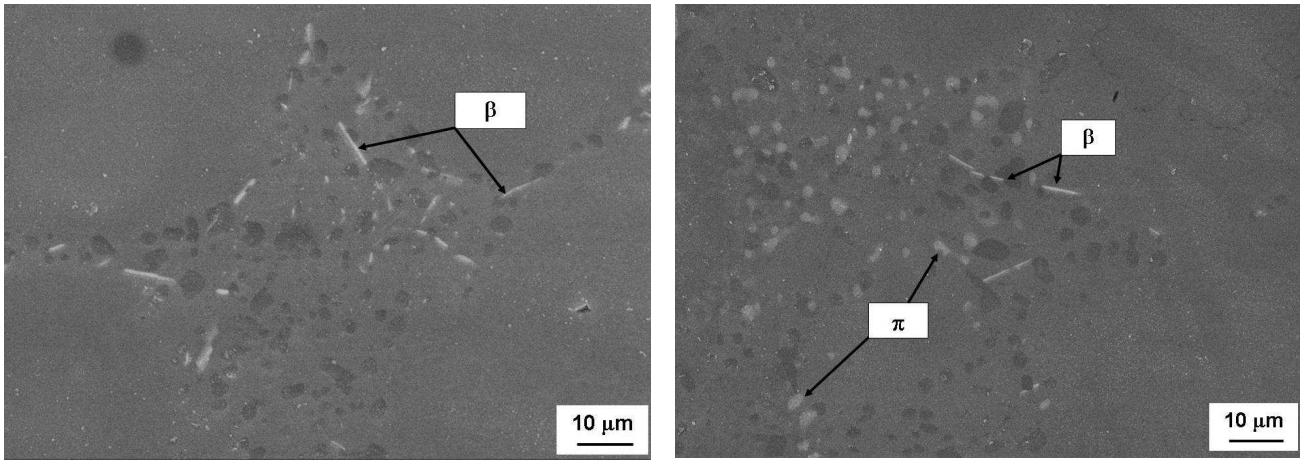

(a) **(b)**

Figure 4.22: Secondary electron images of (a) alloy A356 (with 0.36wt% Mg) and (b) alloy F357 (with 0.62% Mg) after solution treatment at 540°C for 6 h.

The data from Taylor and co-workers [48] as plotted in Fig. 2.20 were used to estimate the Mg-concentration available for precipitation hardening for the bulk compositions used in Fig. 4.20.

Make y = wt% Mg available for precipitation hardening

x = Bulk wt% Mg-content of alloy

For $0.25 \leq$ Bulk Mg ≤ 0.4

$$y = x \qquad (4.4)$$

For $0.4 \leq$ Bulk Mg ≤ 0.7 (see Figure 4.24, deduced from the high Mg-range in Figure 2.20)

$$y = -0.25x^2 + 0.665x + 0.1755 \qquad (4.5)$$

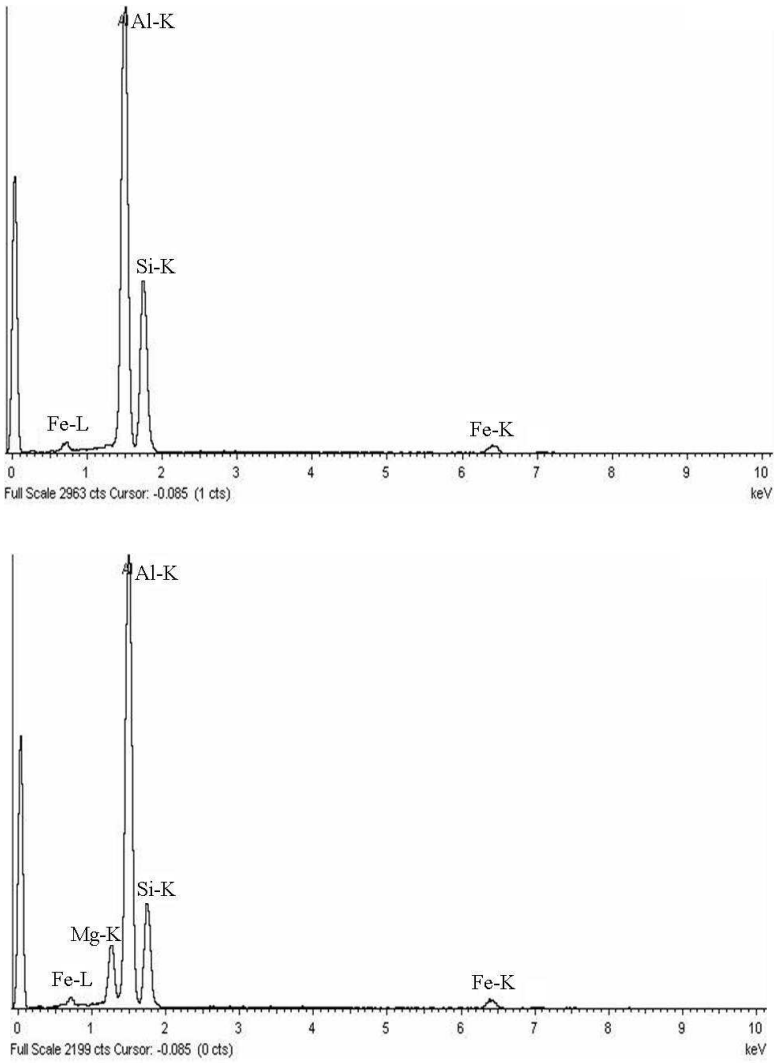

Figure 4.23(a): EDS spectrum for a β–Al_5FeSi-particle. Note the absence of a Mg-peak, (b) EDS spectrum for a π-particle. Note the presence of a Mg-peak.

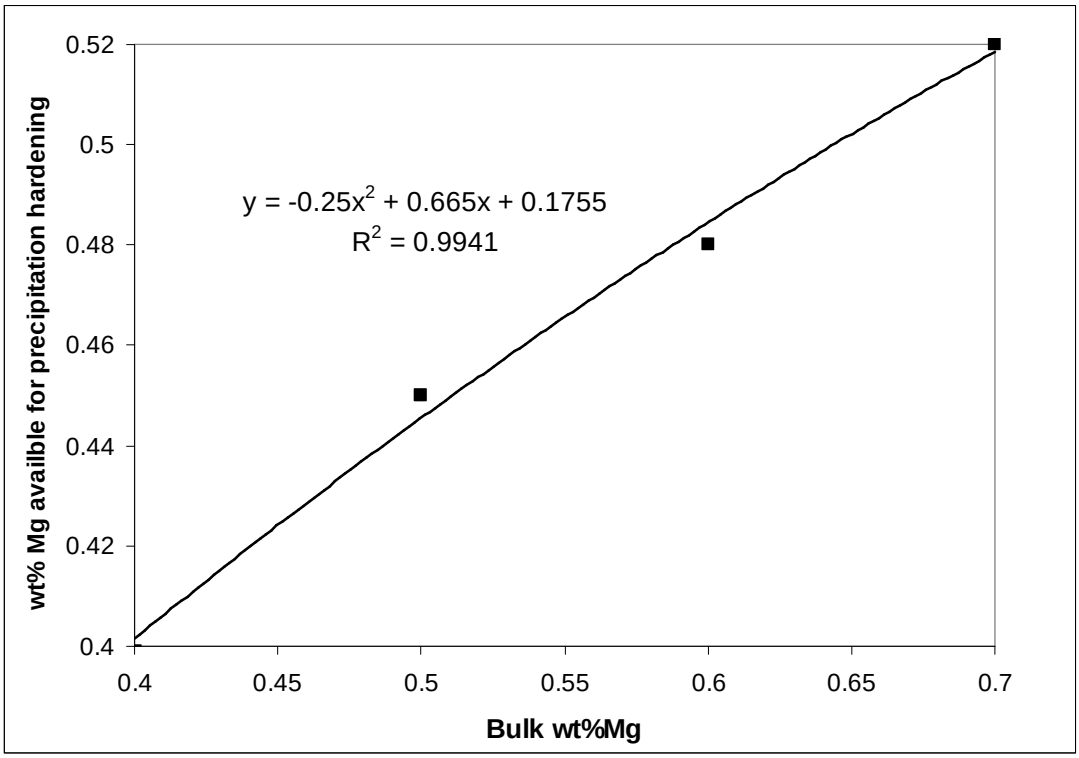

Figure 4.24: Estimation of Mg-content available for precipitation hardening for bulk Mg-contents of between 0.40 and 0.70% (Data points from Fig. 2.20 [48]).

The effects of Mg on the yield strength can be understood in terms of the age-hardening process. It is known [109] that the increment of the yield strength (ΔYS) is determined by the volume fraction (f) of shearable and non-shearable precipitates (eq. 4.6 - also see Chapter 6):

$$\Delta YS = \text{Constant} \times (f)^{1/2} \qquad (4.6)$$

Provided that all the Mg is available for precipitation hardening (i.e. calculated by equations 4.4 and 4.5 and converting from wt% to at% Mg), then ΔYS should be proportional to (at% Mg available for precipitation hardening)$^{1/2}$ – eq. 4.6 [109]. Therefore, taking the same YS data points in Fig. 4.20 and plotting it against (at% Mg available for precipitation hardening)$^{1/2}$, a linear relationship is obtained as shown in Fig. 4.25. Note that a good linear relationship is also found between YS and (at% Mg available for precipitation hardening) - i.e. not the square root of the at% Mg (Fig. 4.26) [HM8]. This occurs due to the fact that the mathematical function of $x^{1/2}$ vs x is almost linear in the composition range of x = 0.28-0.55at% Mg-available for

precipitation hardening in alloys A356/7 (Fig. 4.27). However, the YS-at%$Mg^{1/2}$ relationship in Fig. 4.25 is fundamentally the correct relationship.

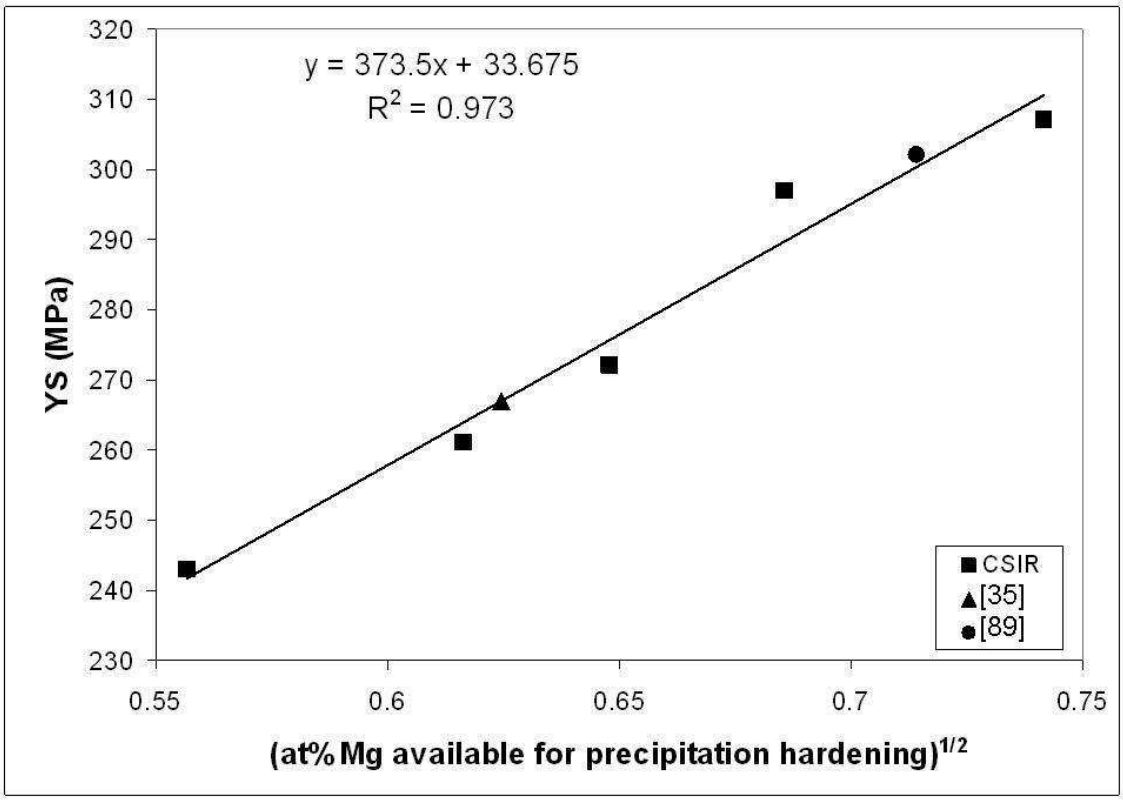

Figure 4.25: YS as a function of (at% Mg-concentration available for precipitation hardening)$^{1/2}$ for the traditional T6 heat treatment - same data points used as in Figure 4.20.

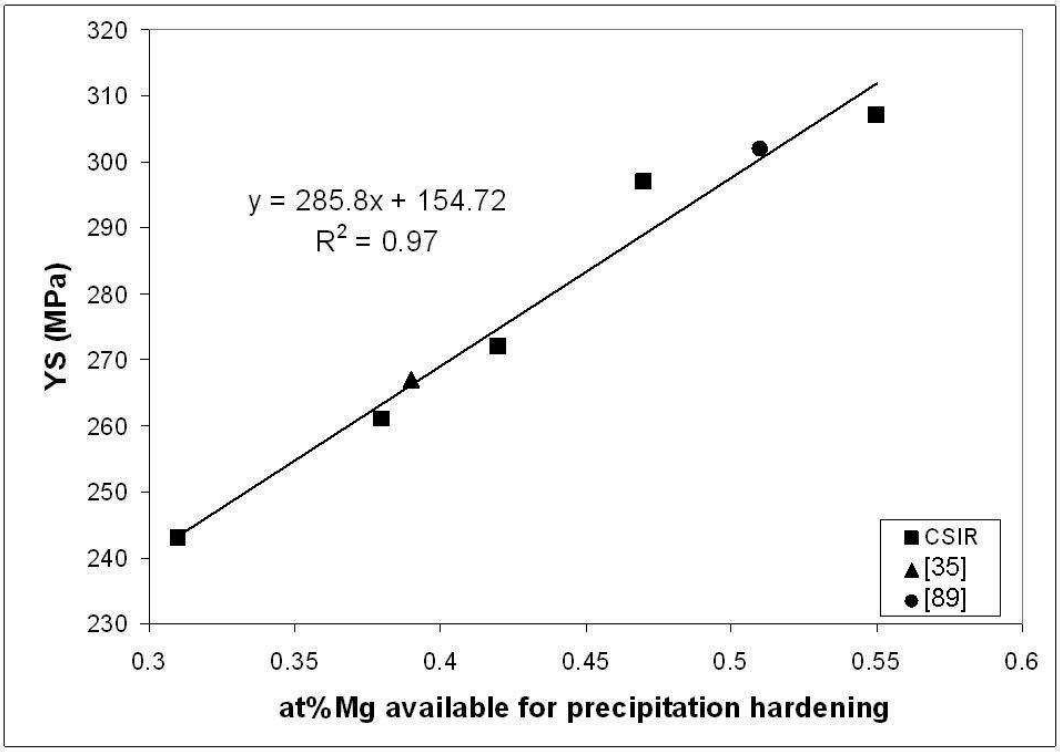

Figure 4.26: YS as a function of at% Mg-concentration available for precipitation hardening for the traditional T6 heat treatment - same data points used as in Figures 4.20 and 4.25.

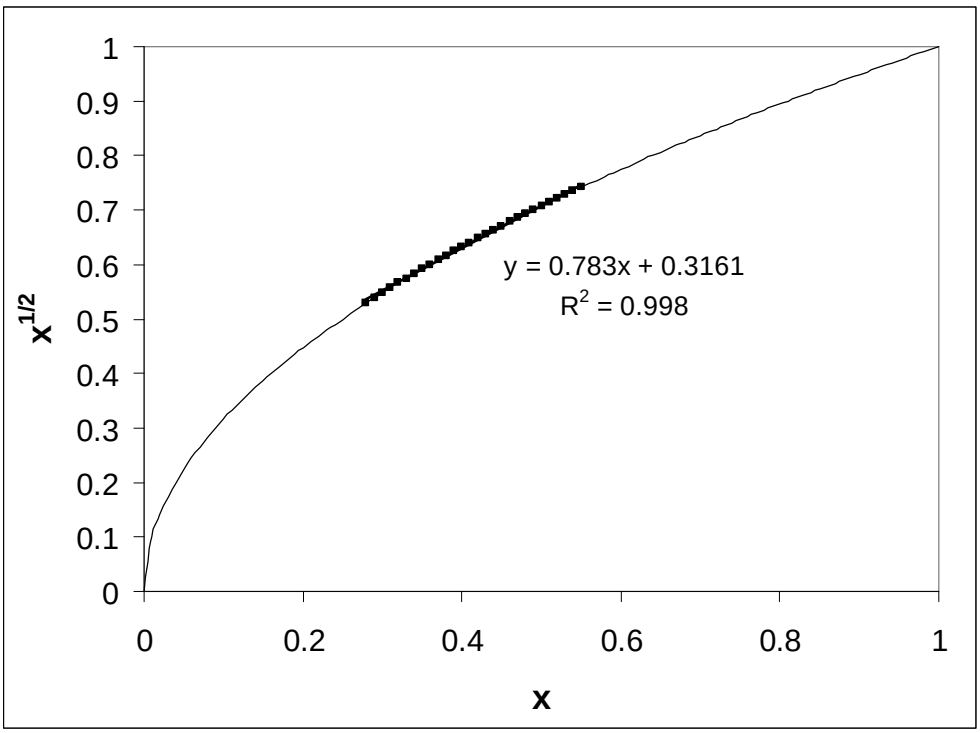

Figure 4.27: $(x)^{1/2}$ vs x mathematical function showing an almost linear relation in the typical range of x = 0.28-0.55at% Mg-available for precipitation hardening for alloys A356/7.

Figure 4.25 is applicable to the traditional T6 heat treatments. A similar approach was followed to determine if the Mg-content has a comparable effect on the CSIR heat treatment cycles (Figs. 4.28 to 4.33) [HM1]. The tensile properties of SSM-HPDC Al-7Si-Mg alloys with different Mg-contents in the CSIR heat treated T6 temper conditions are shown in Table 4.14.

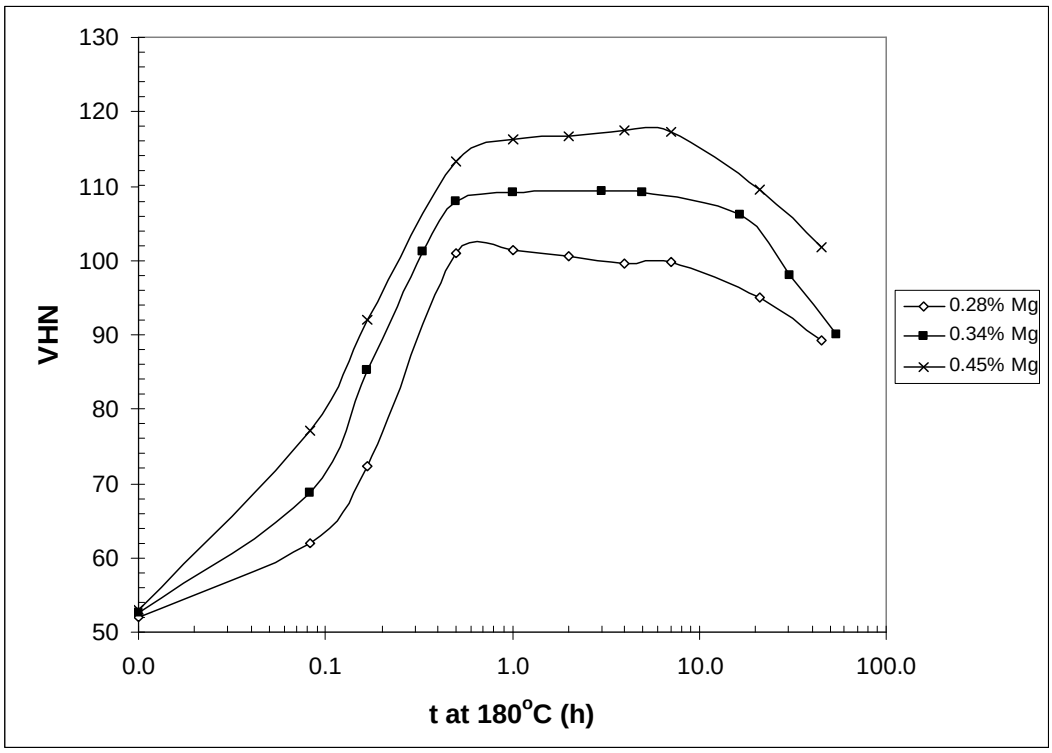

Figure 4.28: Artificial aging curves at 180°C for SSM-HPDC Al-7Si-Mg alloys after 0 h natural pre-aging.

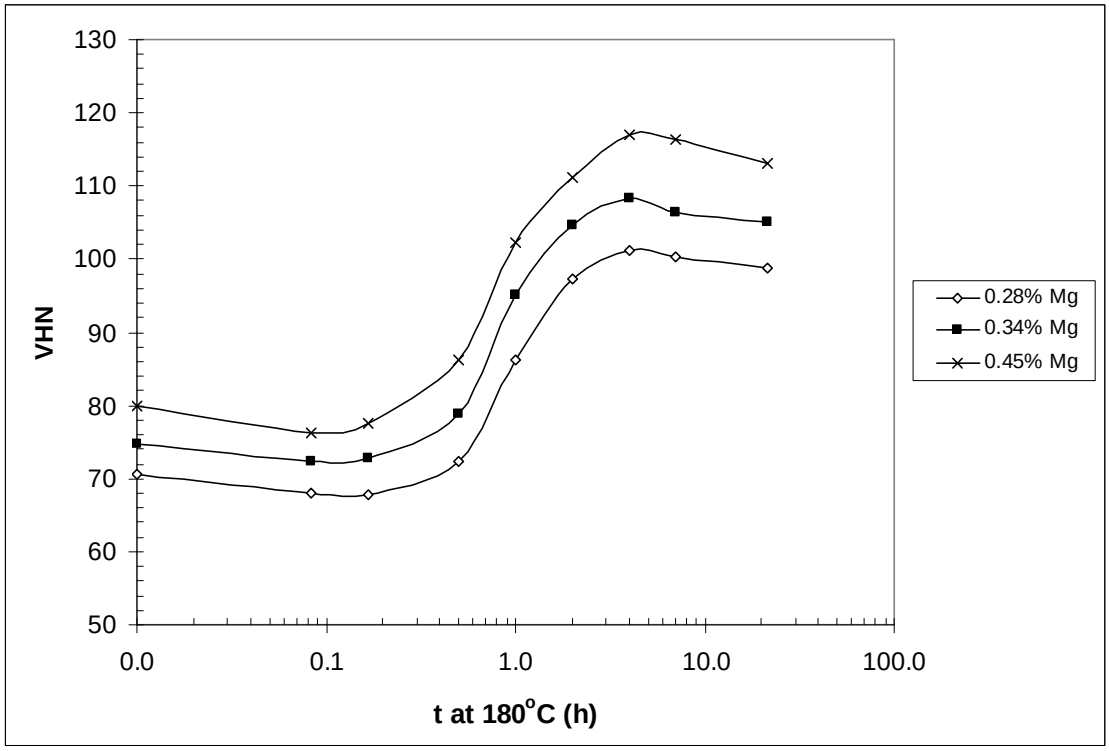

Figure 4.29: Artificial aging curves at 180°C for SSM-HPDC Al-7Si-Mg alloys after 20 h natural pre-aging.

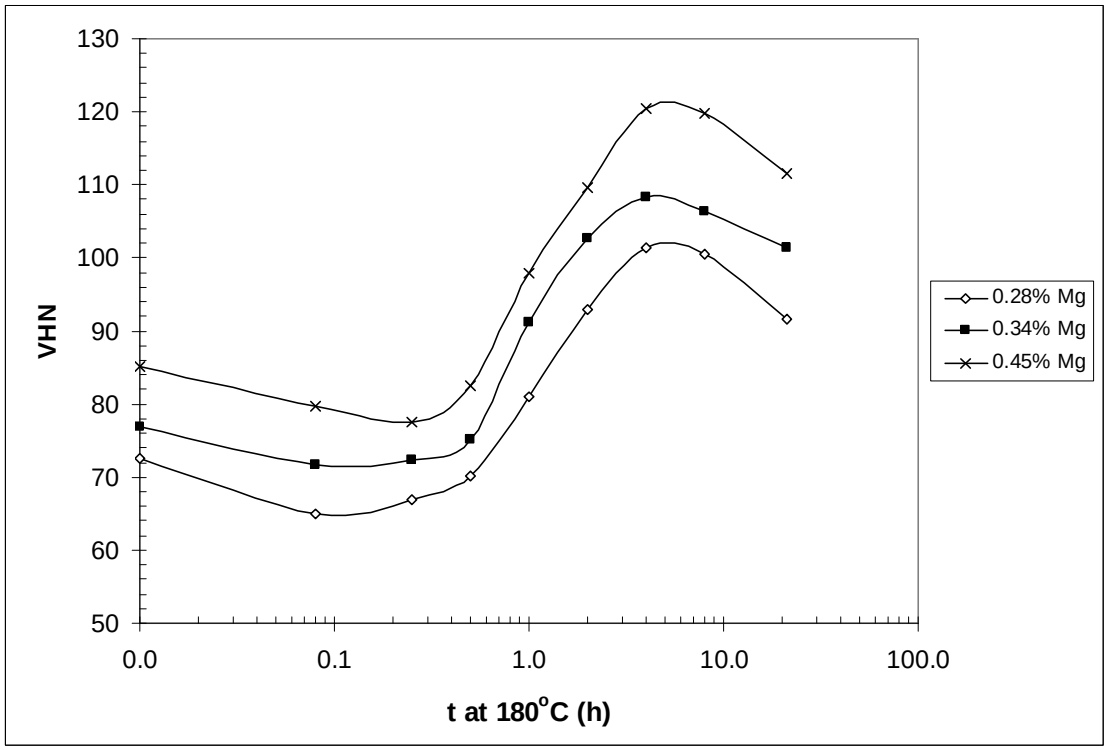

Figure 4.30: Artificial aging curves at 180°C for SSM-HPDC Al-7Si-Mg alloys after 120 h natural pre-aging.

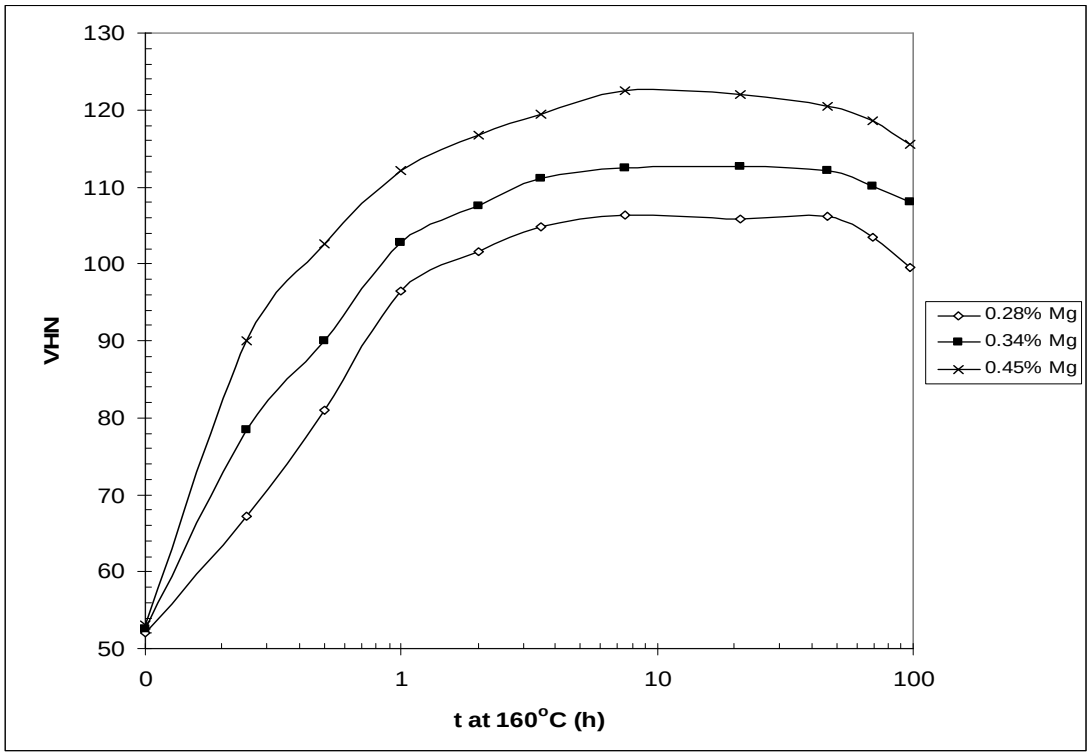

Figure 4.31: Artificial aging curves at 160°C for SSM-HPDC Al-7Si-Mg alloys after 0 h natural pre-aging.

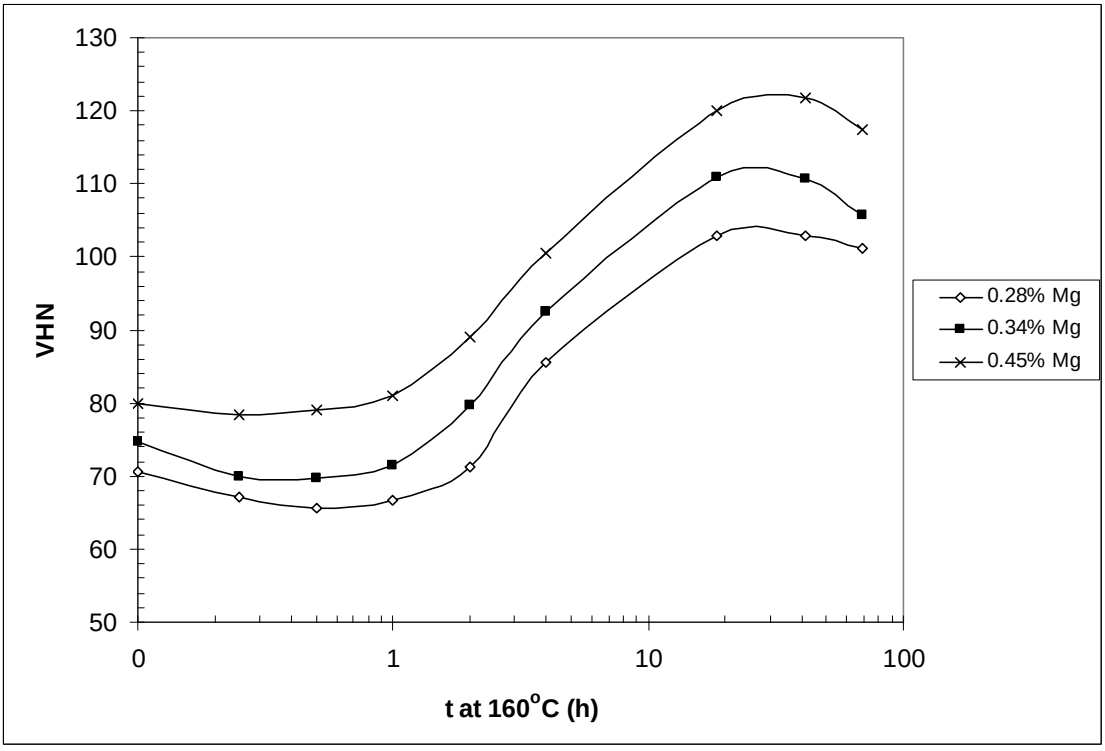

Figure 4.32: Artificial aging curves at 160°C for SSM-HPDC Al-7Si-Mg alloys after 20 h natural pre-aging.

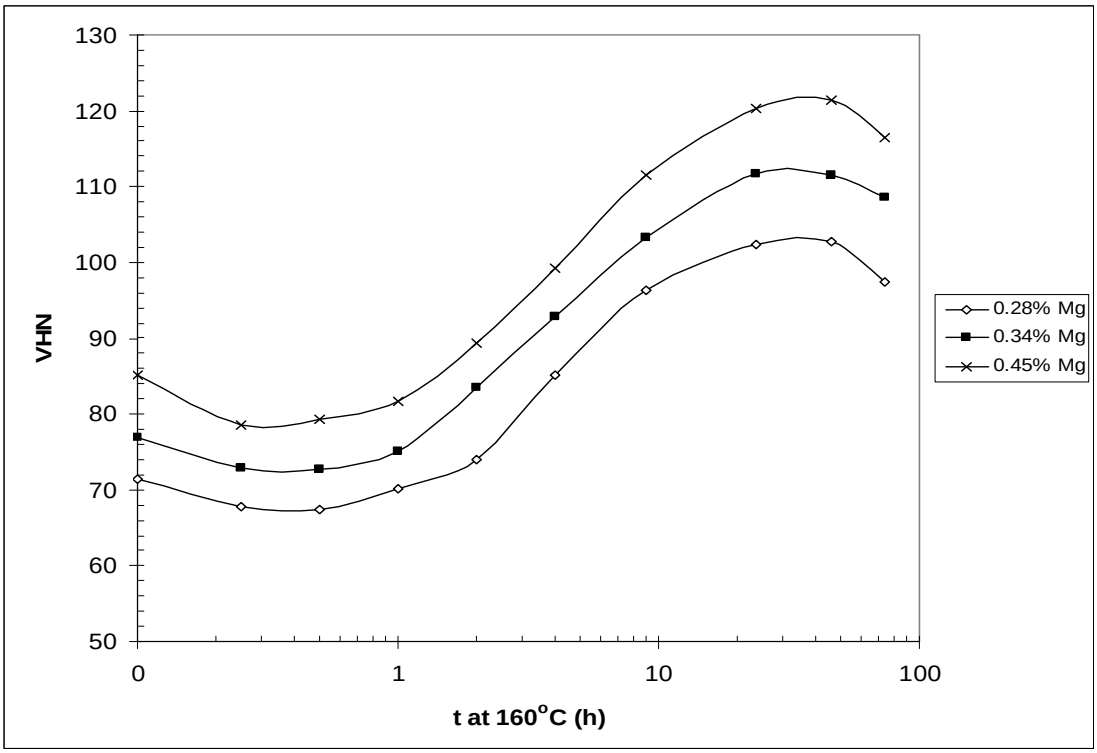

Figure 4.33: Artificial aging curves at 160°C for SSM-HPDC Al-7Si-Mg alloys after 120 h natural pre-aging.

Table 4.14: Yield strength (YS), UTS and % elongation after fracture of SSM-HPDC Al-7Si-Mg alloys (produced with the 50t HPDC machine) in the T6 temper condition (540°C-1h, {20-120}h NA, 180°C-4h). The standard deviation from five values for tensile properties is also indicated in brackets.

Mg-content (wt%)	Mg-content (at%)	YS (MPa)	UTS (MPa)	% Elongation
0.25	0.28	243 (1.4)	303 (1.5)	7.9 (0.7)
0.28	0.31	240 (2.8)	301 (3.1)	9.4 (0.9)
0.31	0.35	254 (6.1)	313 (7.3)	10.5 (0.9)
0.34	0.38	259 (5.2)	317 (7.1)	8.8 (1.4)
0.36	0.40	270 (5.5)	328 (5.8)	8.0 (2.2)
0.38	0.42	272 (5.1)	332 (4.4)	7.9 (1.5)
0.40	0.45	280 (5.2)	337 (6.0)	6.9 (1.8)
0.45	0.50	294 (5.8)	344 (3.1)	7.1 (1.4)
0.62	0.69	312 (4.1)	355 (3.9)	6.0 (1.3)

The data in Table 4.14 were processed in a similar manner to that in Fig. 4.25 to produce YS as a function of (at% Mg-concentration available for precipitation hardening)$^{1/2}$ for the short CSIR T6 heat treatment cycles (Fig. 4.34).

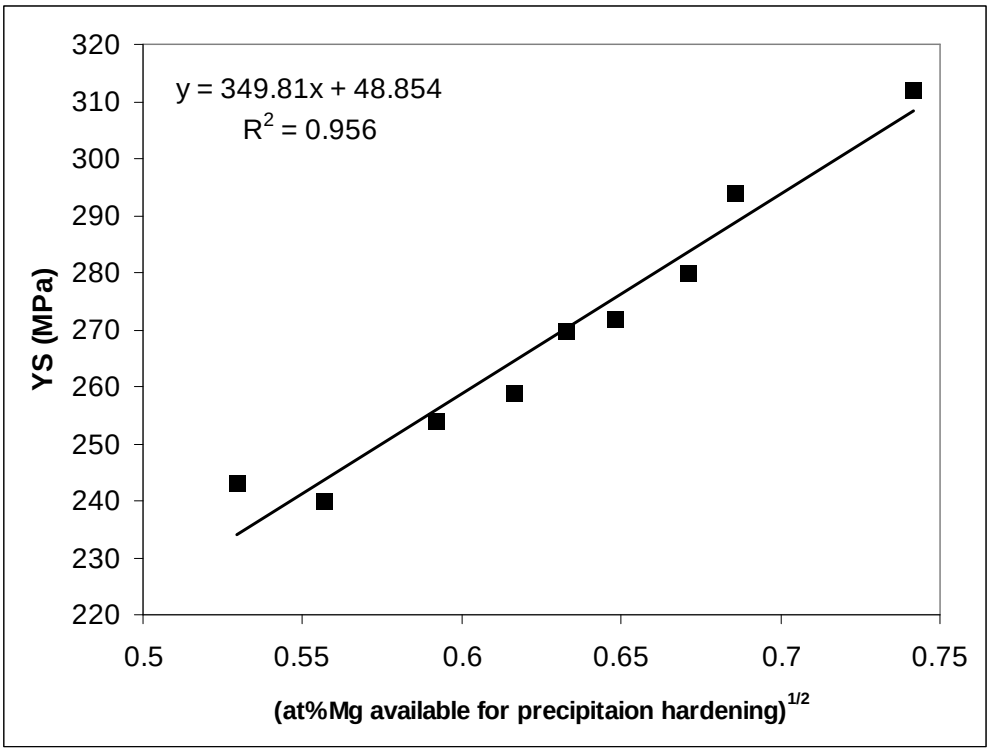

Figure 4.34: YS as a function of (at% Mg-concentration available for precipitation hardening)$^{1/2}$ for the short CSIR T6 heat treatment (540-1,{20-120}NA, 180-4).

As with Fig. 4.25, a reasonable linear relationship is also found in Fig. 4.34. Note that the data points in Figures 4.25 and 4.34 are only applicable for Al-7Si-Mg alloys containing ~ 0.1% Fe. Alloys with more than 0.1% Fe should result in the formation of more of the π-phase and vice versa.

The alloys with 0.62% Mg-0.10% Fe and 0.67% Mg-0.25% Fe in Table 3.1 were used to study the effects of Fe-levels above specification [HM9]. The calculated phase equilibria (minor phases) using Thermo-Calc for these two Al-alloys of alloy F357 are shown in Fig. 4.35. In this figure, the liquidus and solidus temperatures are indicated by arrows; "pi" refers to the π phase, "beta" is β–Al_5FeSi, and "alpha" is an Al-Mn-Fe-Si solid solution based on Al_8Fe_2Si. In all cases the major phases were liquid, Al-based FCC solid solution (the primary phase upon solidification), and Si (formed by

eutectic solidification). Comparing the two diagrams, it is seen that the predicted Mg_2Si content is slightly lower for the 0.62Mg-0.10Fe alloy than the 0.67Mg-0.25Fe alloy. This is to be expected, as the Mg-content of the former is lower than that of the latter. Based solely on the Mg-contents of the two alloys, the expectation is that the strength in the T6 temper of alloys from the 0.67Mg-0.25Fe alloy should be slightly higher (see the discussion on tensile properties later to see why this is not the case here – due to the effects of Fe). The higher Fe and Ni contents of the 0.67Mg-0.25Fe alloy lead to significantly higher predicted quantities of phases such as π-$Al_8FeMg_3Si_6$, β-Al_5FeSi and Al_9FeNi than for the 0.62Mg-0.10Fe alloy. Scanning electron microscopy (coupled with EDS to tentatively identify phases) was used to study the intermetallic phases in the T4 and T6 temper conditions (the intermetallics are similar in both temper conditions). Backscattered electron images of samples from both alloys are shown in Fig. 4.36. For the 0.62Mg-0.10Fe alloy (Fig. 4.36(a)), only β-Al_5FeSi and π-$Al_8FeMg_3Si_6$ could be identified in the eutectic (see typical EDS spectra in Fig. 4.37 for all qualitatively identified phases in the samples). However, for the 0.67Mg-0.25Fe alloy, apart from higher quantities of β-Al_5FeSi and π-$Al_8FeMg_3Si_6$, particles of Al_9FeNi could also be identified (Fig. 4.36(b) and Fig. 4.37(c)). Note that Si was also detected in the EDS of the Al_9FeNi particles. The maximum solubility of Si in this phase has been reported to be 4% [110]. The tensile properties of T4 and T6 heat treated samples were determined and the results are shown in Table 4.15.

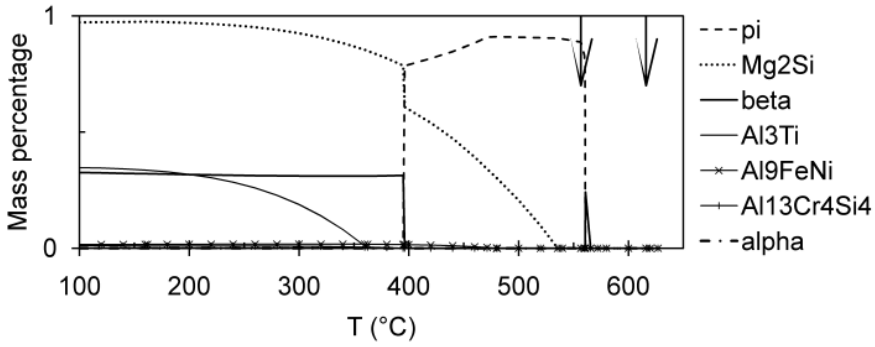

(a)

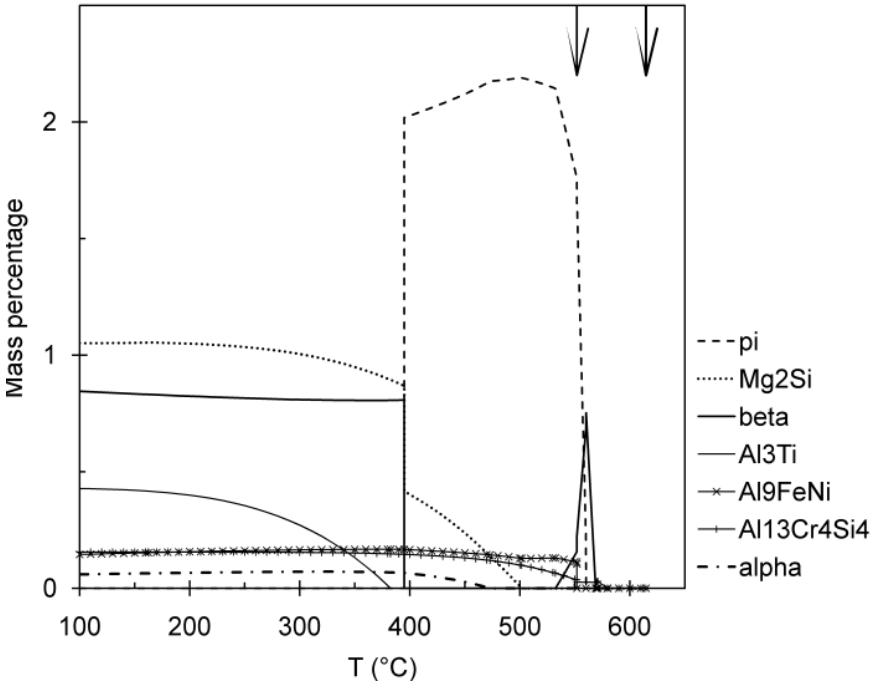

(b)

Figure 4.35: Calculated phase equilibria (minor phases) for Al alloys with compositions given in Table 3.1 corresponding to the (a) 0.62Mg-0.10Fe alloy and (b) 0.67Mg-0.25Fe alloy.

The expectation is that the 0.67Mg-0.25Fe should give higher strength than the 0.62Mg-0.10Fe alloy in both temper conditions based on Fig. 4.34. However, from Table 4.15 it can be seen that the strength (YS and UTS) of the two alloys are fairly similar. This can be related directly to the higher Fe-content of the 0.67Mg-0.25Fe alloy. The presence of high quantities of the Mg-containing π-phase in samples from this alloy (Fig. 4.36(b)) causes a reduction in the amount of magnesium in solid solution, which has a detrimental effect on the aging behaviour of samples from this

alloy. Note that the Mg-free particles such as β-Al_5FeSi and Al_9FeNi particles do not contribute to this effect.

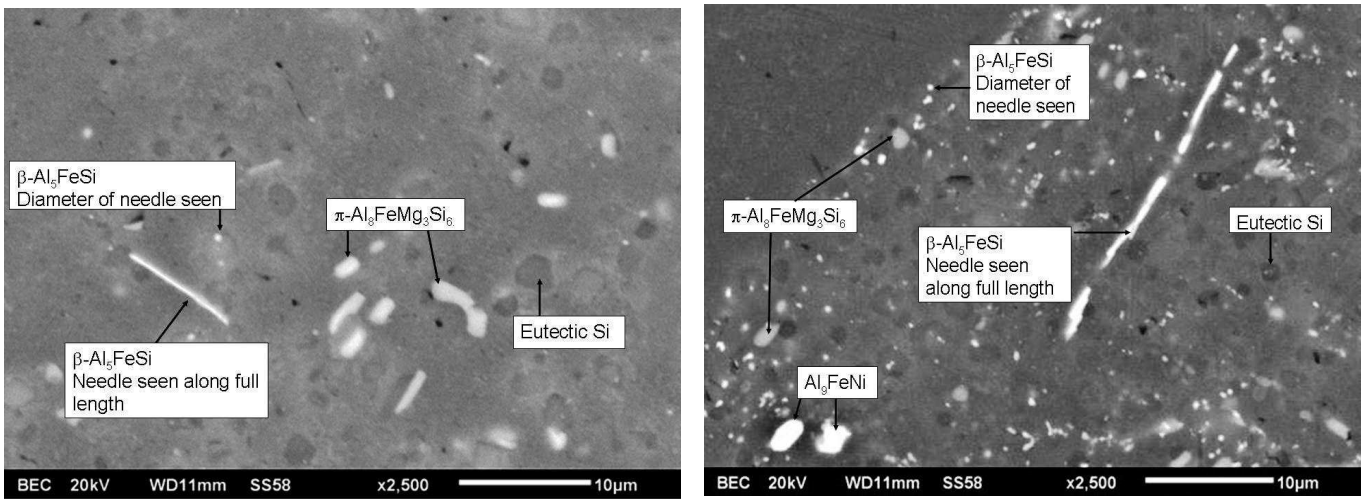

(a) **(b)**

Figure 4.36: Backscattered electron images of T6 samples of (a) 0.62Mg-0.10Fe alloy and (b) 0.67Mg-0.25Fe alloy.

Table 4.15: Yield strength (YS), ultimate tensile strength (UTS) and % elongation after fracture (%A) of T4 and T6 heat treated F357 samples. The standard deviation from five values for tensile properties is also indicated in brackets.

Alloy	YS (MPa)	UTS (MPa)	% A
T4 (540°C-1h, 120 h natural aging)			
0.62Mg-0.10Fe	172 (4.7)	297 (4.0)	17 (2.5)
0.67Mg-0.25Fe	169 (3.6)	285 (5.7)	8.2 (2.0)
T6 (540°C-1h, 20 h natural aging, 180°C-4h artificial aging)			
0.62Mg-0.10Fe	312 (4.1)	355 (3.9)	6.0 (1.3)
0.67Mg-0.25Fe	313 (2.2)	353 (5.0)	3.5 (0.64)

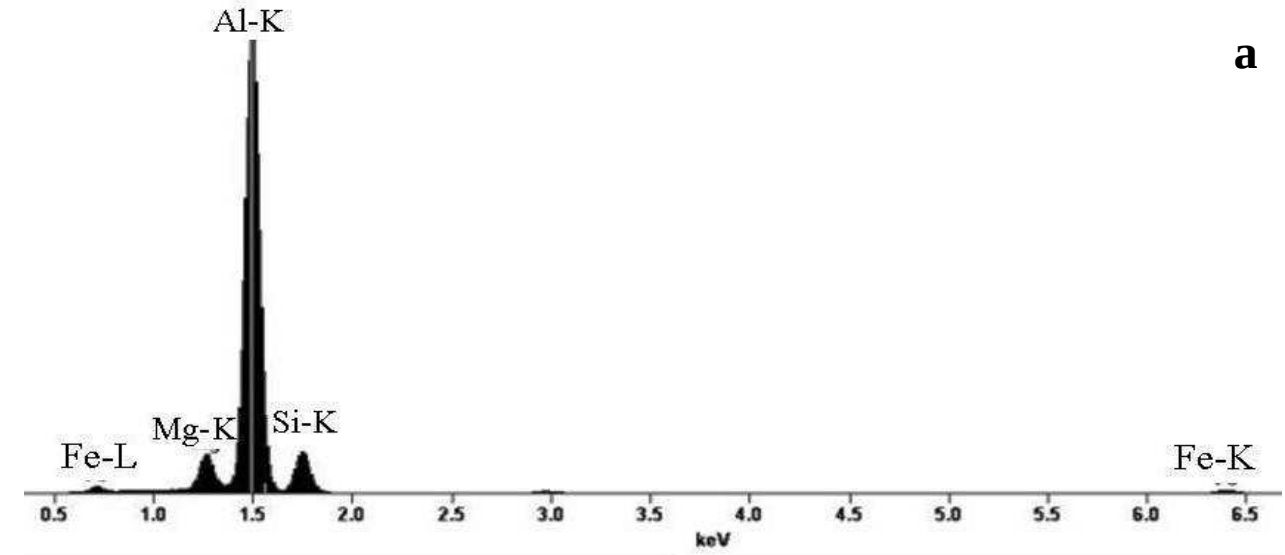
a
Al-K
Mg-K
Si-K
Fe-L
Fe-K
0.5 1.0 1.5 2.0 2.5 3.0 3.5 4.0 4.5 5.0 5.5 6.0 6.5
keV

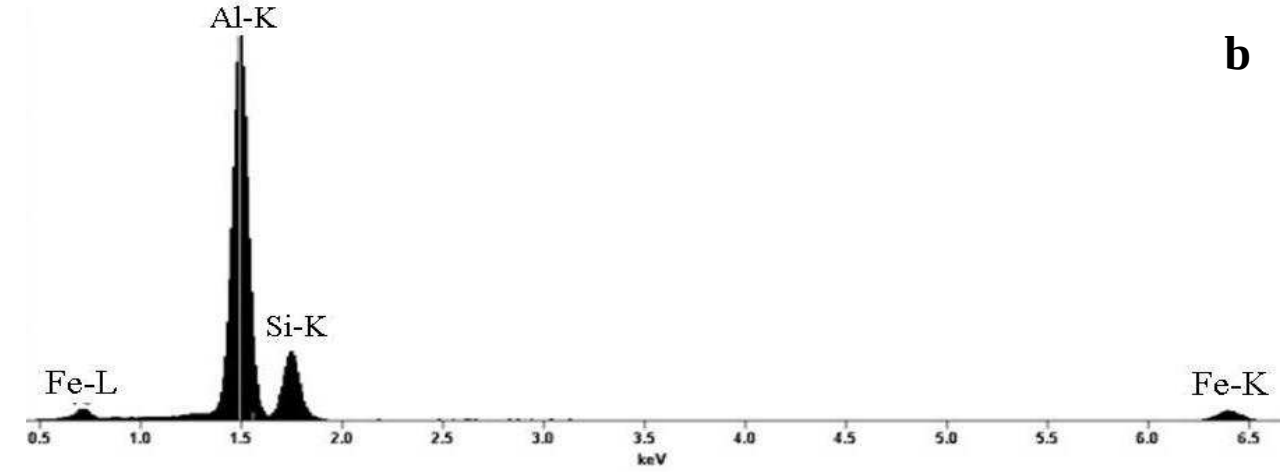
b
Al-K
Si-K
Fe-L
Fe-K
0.5 1.0 1.5 2.0 2.5 3.0 3.5 4.0 4.5 5.0 5.5 6.0 6.5
keV

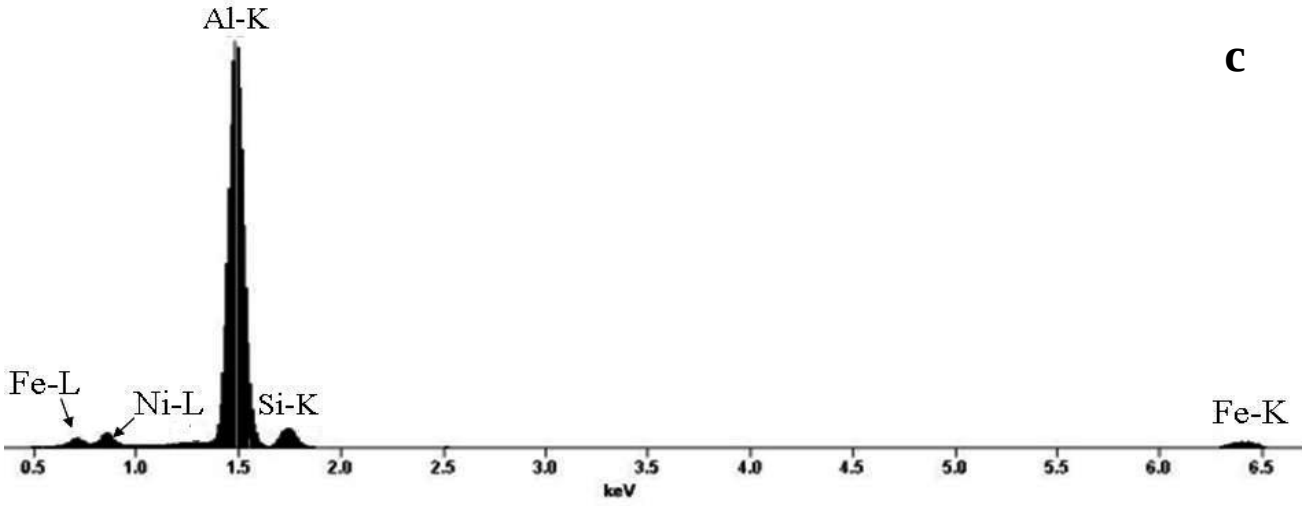
c
Al-K
Fe-L
Ni-L
Si-K
Fe-K
0.5 1.0 1.5 2.0 2.5 3.0 3.5 4.0 4.5 5.0 5.5 6.0 6.5
keV

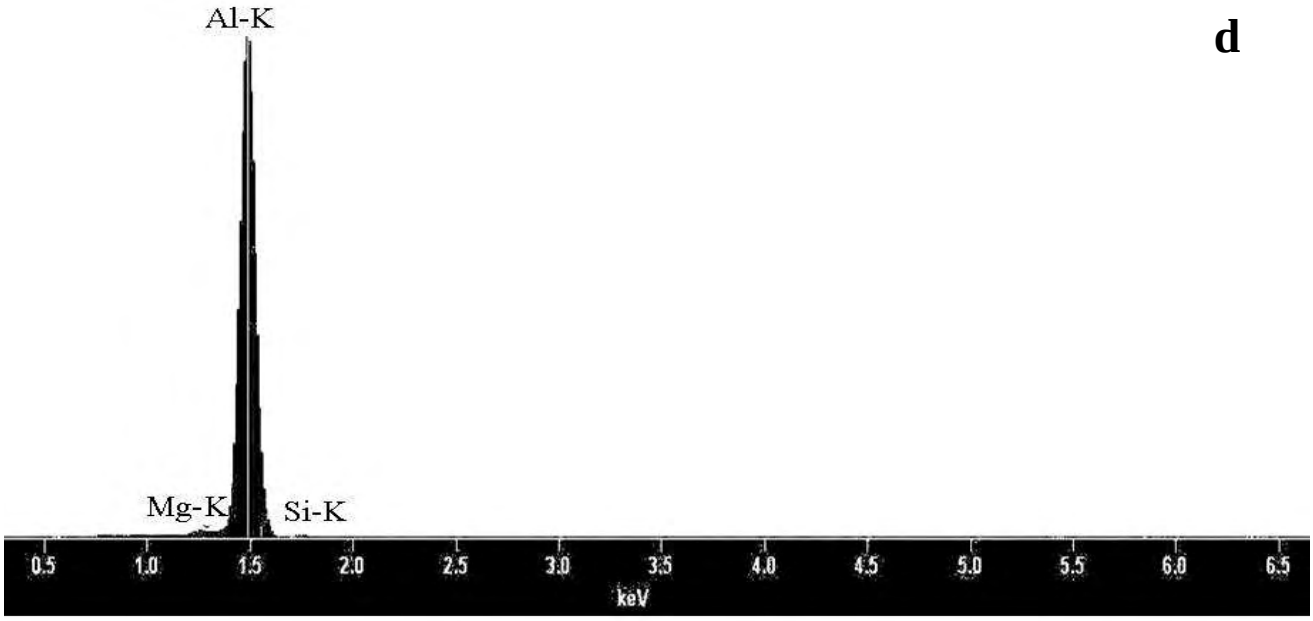

Figure 4.37: EDS spectra of qualitatively identified (a) π-$Al_8FeMg_3Si_6$, (b) β-Al_5FeSi (note the absence of a Mg-peak) and (c) Al_9FeNi particles (note the presence of a Ni-peak). The EDS spectrum in (d) is of a primary α-Al grain from a T4 sample as reference.

Even though the YS and UTS of the two alloys are fairly similar, the ductilities differ significantly (Table 4.15). The % elongation of samples from the 0.67Mg-0.25Fe is considerably lower in both temper conditions. Figure 4.38 shows a backscattered electron image of a sample from the 0.67Mg-0.25Fe alloy in the T6 condition after tensile testing. The fracture occurred to the right of the image and part of the fracture surface can be seen. Micro-cracking of the intermetallics can clearly be seen. Taylor and co-workers [48] also reasoned that any increase in the amount of hard, brittle π-intermetallics would lead to a decrease in elongation to fracture values in this alloy system.

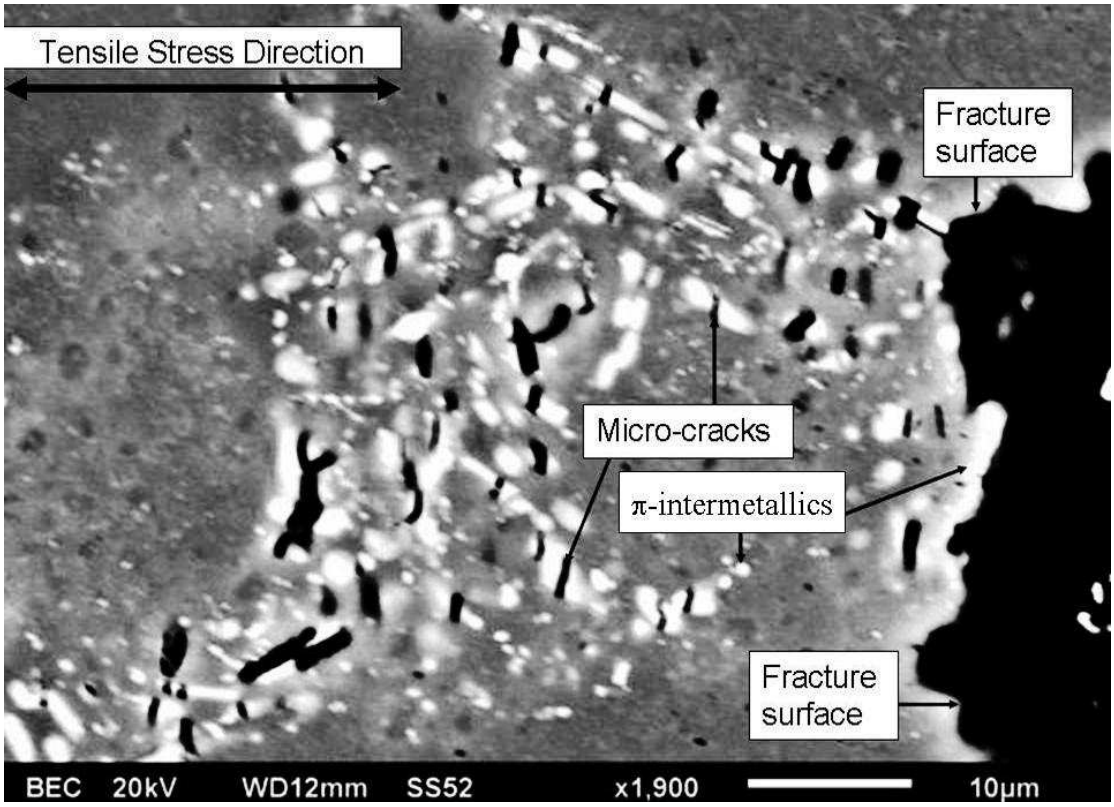

Figure 4.38: Backscattered electron image of T6 sample of the 0.67Mg-0.25Fe after tensile testing showing the fracture surface on the right, as well as micro-cracking of the π-intermetallics.

Another effect of the intermetallics in this alloy system (which was not studied in this work) is their influence on corrosion properties. Yang and co-workers [34] showed that intermetallic compounds play a major role in the pit initiation process of Al–7Si–Mg alloys. Micro-galvanic cells are produced, leading to corrosion attack along the interface between the intermetallic compounds and the aluminium alloy matrix. The 0.67Mg-0.25Fe alloy is therefore expected to have inferior corrosion resistance compared to the 0.62Mg-0.10Fe alloy.

4.7. Artificial aging and the T5 temper

The T5 temper is achieved by artificially aging as-cast material without a solution treatment (as opposed to the T4 and T6 temper conditions where a solution heat treatment is used).

Variables that affect the T5 properties are the cooling rate after casting (air or AQ and water or WQ), the natural aging period after quenching and the artificial aging

temperature and time. The tensile properties of differently T5-treated SSM-HPDC alloy F357 (with 0.63% Mg) are compared in Table 4.16 [HM6]. As expected, higher tensile properties are obtained by water quenching the alloy after SSM-HPDC rather than cooling in air. Also, it can be seen from Table 4.16 that there is a significant difference in tensile properties between the as-cast material that was cooled in air [F357-F(AQ)] and the F357-T5(AQ) sample. This implies that most of the elements are actually placed in solution during cooling with SSM-HPDC, rather than with the quench after SSM-HPDC. It has been shown that the solidification rate during HPDC is relatively high (Fig. 4.4).

Table 4.16: Yield strength (YS), ultimate tensile strength (UTS) and % elongation after fracture (%A) of SSM-HPDC F357 with 0.63% Mg. The standard deviation from 12 values for tensile properties is also indicated in brackets.

Quench after SSM-HPDC	Natural Aging (NA)	Artificial aging (AA)	YS (MPa)	UTS (MPa)	% A
Air (AQ)	25°C-120 h	-	117 (2.2)	229 (4.9)	9.9 (1.7)
Water (WQ)	25°C-120 h	-	124 (2.7)	241 (6.1)	9.4 (1.7)
Air (AQ)	25°C-120 h	180°C-4 h	170 (9.9)	256 (10.9)	7.2 (1.5)
Water (WQ)	-	180°C-4 h	186 (3.6)	273 (3.8)	6.6 (1.1)
Water (WQ)	25°C-120 h	180°C-4 h	188 (1.9)	278 (4.9)	6.4 (1.0)
Water (WQ)	25°C-120 h	160°C-28 h	205 (3.1)	290 (4.9)	6.1 (1.3)

Differences in the morphology of β-Mg_2Si in the F(AQ) and F(WQ) can be observed using backscattered electron imaging (Fig. 4.39(a,b)). The β-Mg_2Si is significantly coarser in the F(AQ) samples than in the F(WQ) samples, which corresponds to a slower cooling rate to room temperature in the former sample.

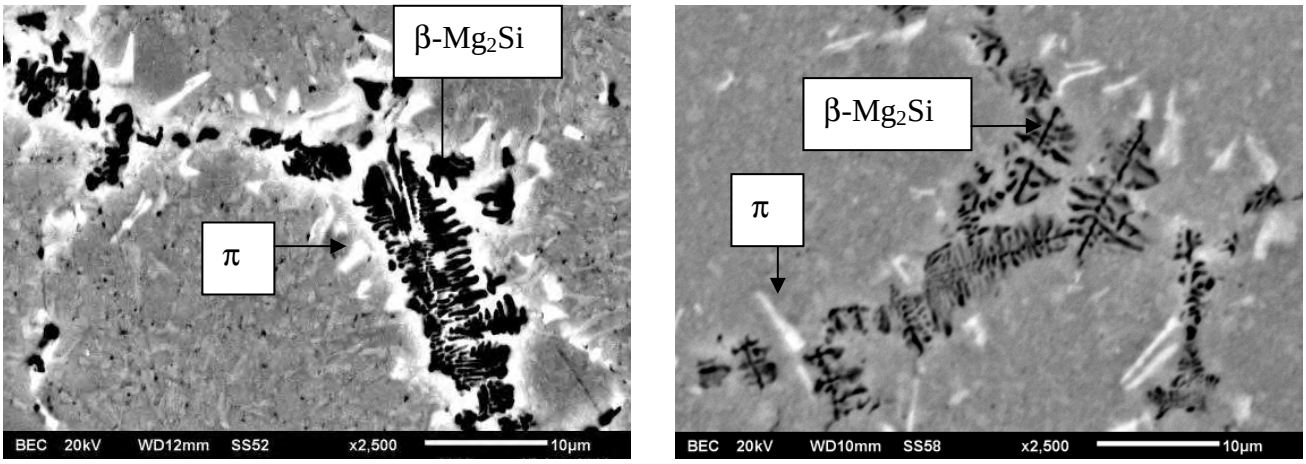

(a) **(b)**

Figure 4.39: Backscattered electron images (BEI) of SSM-HPDC F357 in (a) F(AQ) and (b) F(WQ) conditions.

Figure 4.39 indicates that significant quantities of undissolved β-Mg_2Si are in the F and T5 temper condition samples. The solution treatment of the T4 and T6 temper conditions dissolves the β-Mg_2Si phase and the supersaturation of solute is significantly higher. The artificial aging response for the T6 temper (e.g. Fig 4.18) is therefore considerably more pronounced than for the T5 temper (Fig. 4.40).

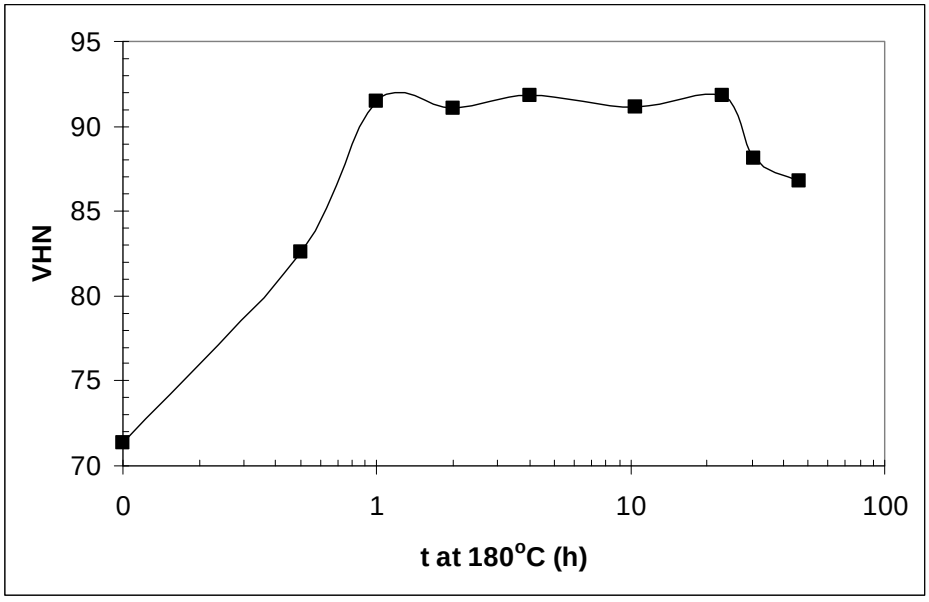

Figure 4.40: T5-artificial aging curve of an SSM-HPDC F357 plate (with 0.63wt% Mg) that was water quenched after casting, naturally aged for 120 h and artificially aged at 180°C.

Natural aging after the quench (0 or 120 h) does not have a meaningful influence on the T5 properties (Table 4.16), but, as already mentioned before, an artificial aging treatment of 180°C for 4 h also resulted in removing the effects of natural pre-aging in the T6 treated alloys (Fig. 4.18). Finally, as with the T6 temper (Fig. 4.17), a lower artificial aging temperature (160 vs 180°C) results in better mechanical properties. Unfortunately, due to the lower diffusion rates at 160°C, the time to attain these properties is reached after much longer times than with artificial aging at 180°C (Table 4.16).

4.8. Comparison between different temper conditions

The properties of SSM-HPDC Al-7Si-Mg alloys in different temper conditions were compared using the alloy with 0.38% Mg in Table 3.1 [HM7]. To make comparisons, solution treatment (for T4 and T6) was performed at 540°C for 1 hour, followed by a water quench (25°C). The T6 treated samples were then naturally aged for 20 hours, before artificial aging for 4 h at 180°C. The T4 treated samples were allowed to naturally age (at 25°C) for at least 120 h. The samples used for the T5 temper condition were quenched in water after SSM-HPDC and naturally aged for 120 h before artificial aging at 180°C for 4 h. Optical micrographs of SSM-HPDC A356 are shown in Figure 4.41 for the as-cast condition or F temper (Fig. 4.41(a)), T4 temper (Fig. 4.41(b)), T5 temper (Fig. 4.41(c)) and the T6 temper (Fig. 4.41(d)). The average Vickers microhardness values (50 g load) of the α-Al and eutectic in all the temper conditions are also shown in Figure 4.41. Heat treatment to the T4, T5 and T6 temper conditions results in an increase in the hardness of the primary α-Al grains and the eutectic regions relative to the A356-F condition. The increase of the hardness of the eutectic component with aging suggests that precipitation hardening also occurs within the α-Al phase of the eutectic. The fibrous silicon particles in A356-F are spheroidised by the solution treatment applied on A356-T4 (Fig. 4.41(b)) and A356-T6 (Fig. 4.41(d)). For A356-T5, no solution treatment is used, and it is seen from Figure 4.41(c) that the artificial aging temperature is too low to cause any spheroidisation of the eutectic silicon particles.

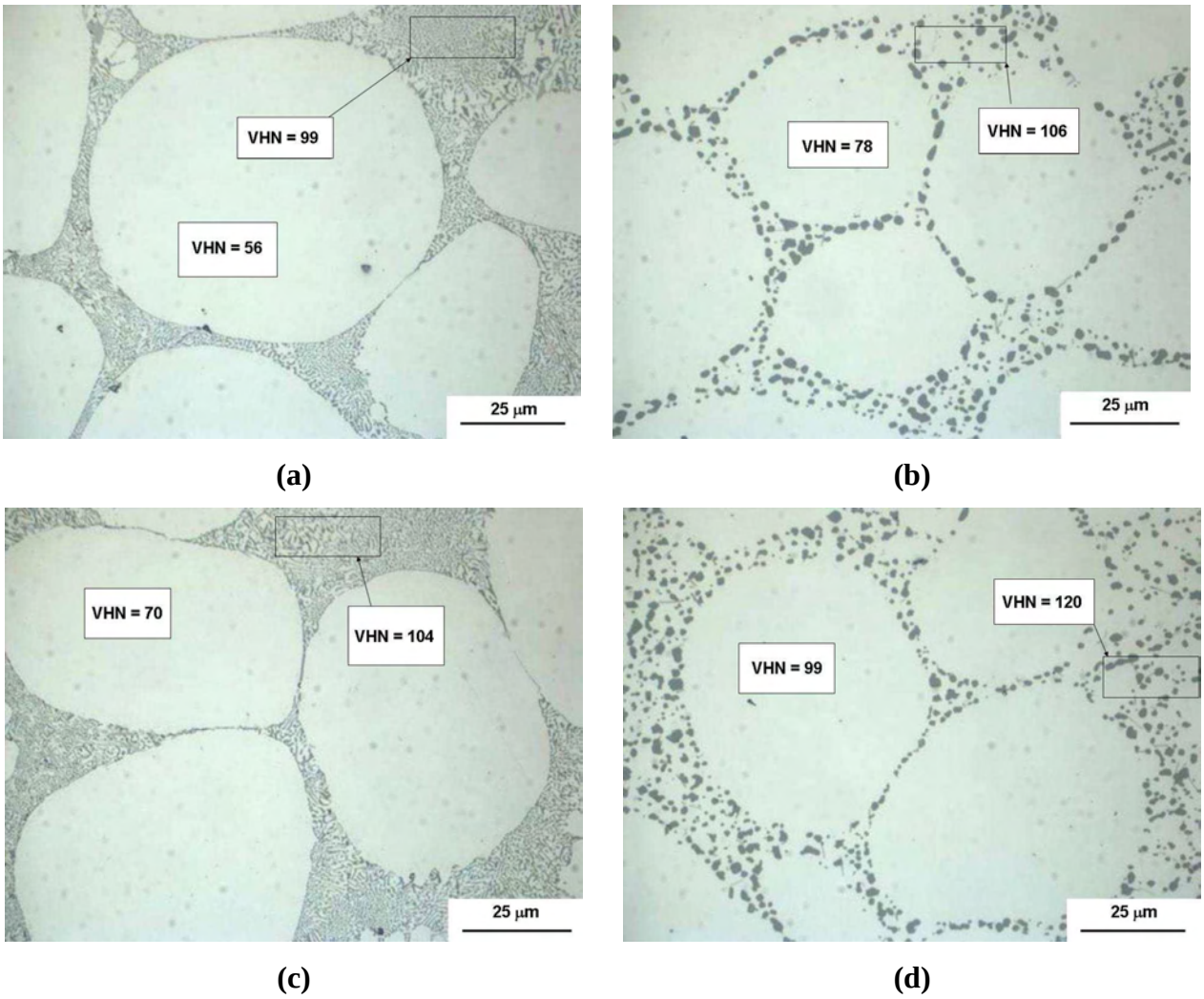

Figure 4.41: Optical micrographs of SSM-HPDC A356 in the (a) F, (b) T4, (c) T5 and (d) T6 temper conditions.

The macrohardness (Fig. 4.42) and tensile properties of this alloy in different temper conditions are shown in Table 4.17. The importance of the solution treatment in dissolving all the solutes for precipitation hardening during artificial aging can clearly be seen by comparing the lower tensile properties of A356-T5 with those of A356-T6. On the other hand, the beneficial effect of artificial aging after solution treatment (A356-T6) rather than natural aging (A356-T4) is also evident. The Quality Index (QI) for SSM-HPDC alloy A356 in different temper conditions is shown in Table 4.17. It is seen that the high ductility of A356-T4 and high strength of A356-T6 result in high QI values for these two temper conditions.

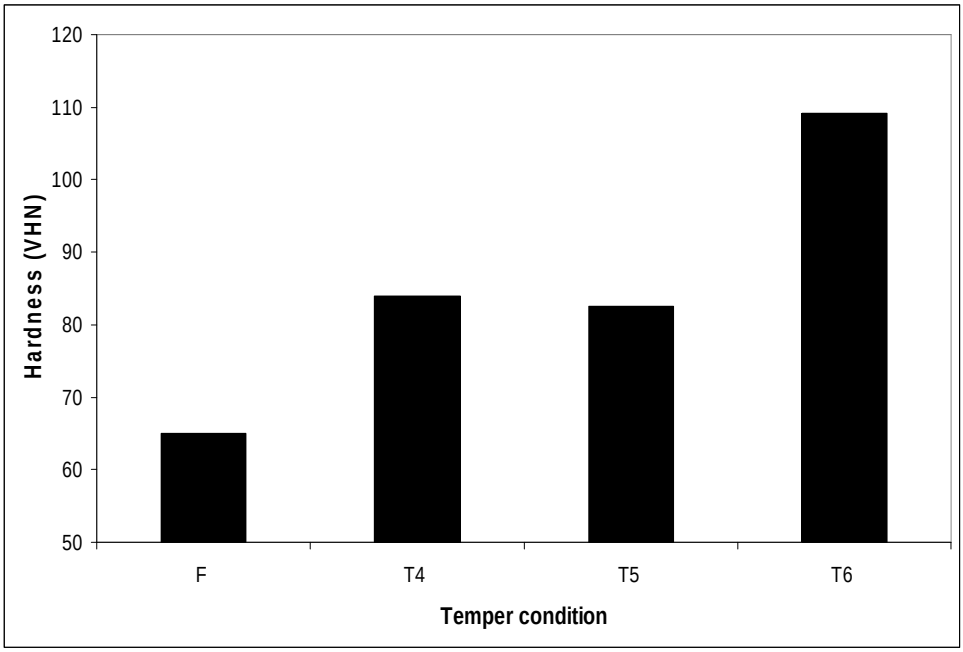

Figure 4.42: Vickers macrohardness (20 kg) of SSM-HPDC A356 in different temper conditions.

Table 4.17: Yield strength (YS), ultimate tensile strength (UTS), % elongation after fracture and Quality Index (QI) of heat treated A356 samples with 0.38% Mg. The standard deviation for tensile properties (from 5 samples/temper condition) is also indicated in brackets.

Temper	YS (MPa)	UTS (MPa)	% Elongation	QI (MPa)
F	113 (3.0)	218 (2.5)	10.6 (1.6)	372 (10.6)
T4	152 (2.1)	268 (3.9)	14.5 (1.4)	442 (7.2)
T5	168 (2.2)	258 (4.0)	8.4 (0.9)	396 (10.2)
T6	272 (5.1)	332 (4.4)	7.9 (1.5)	466 (12.7)

The drop weight impact energies for A356 in different temper conditions are shown in Figure 4.43. Alloy strength (Fig. 4.13) and silicon morphology have the largest effects on the impact properties of this material. The influence of strength of the alloys on the impact properties can be determined by comparing temper conditions in which the silicon morphologies are similar. In both A356-T4 and A356-T6, spheroidised silicon is found. However, the impact strength of the material is slightly higher for A356-T4 than A356-T6. This difference can be related to the lower strength (hardness) of the material in the T4 condition compared to the T6 condition.

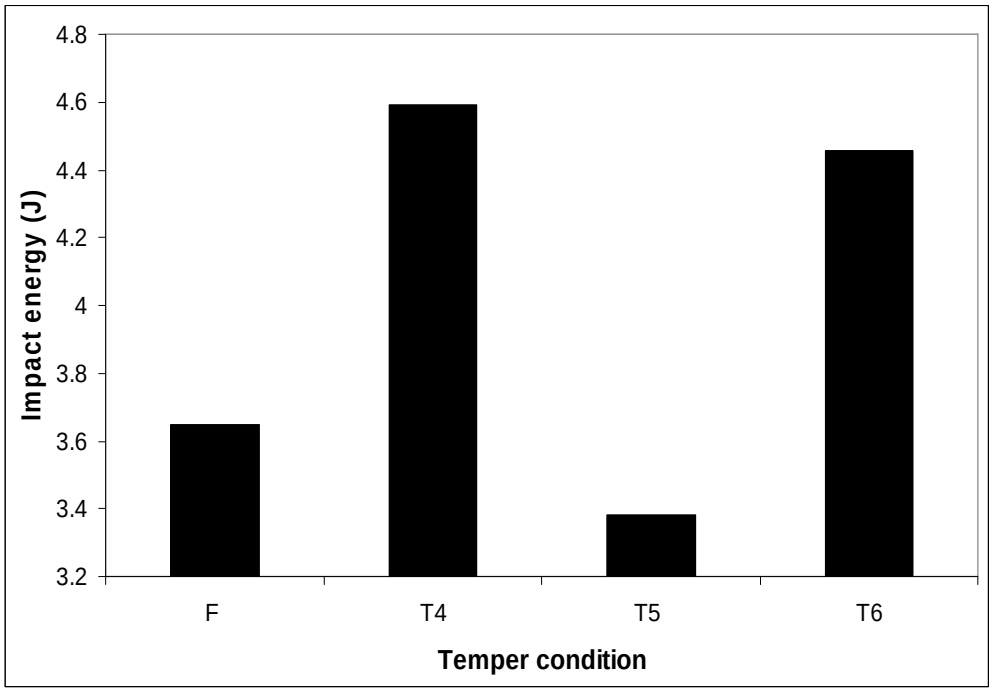

Figure 4.43: Drop weight impact energies for SSM-HPDC A356.

In both A356-F and A356-T5, fibrous silicon is found. Again, the impact strength of the material is slightly higher for the lower strength (hardness) A356-F than A356-T5. The influence of silicon morphology on the impact properties can be determined by comparing temper conditions in which the silicon morphologies are different (and considering the differences in strength too). The impact strength of A356-F and A356-T5 (with fibrous Si) is significantly lower than that of A356-T4 and A356-T6 (with spheroidised Si). The tips of fibrous silicon particles most likely act as stress concentrators causing much lower impact strengths than when the silicon particles are spheroidised.

The impact load as a function of time was measured and is presented in Figure 4.44. The first peak (maximum load) in Figure 4.44 corresponds to crack initiation, whereas the rest of the curve corresponds to crack propagation. The total time to complete fracture (time-to-zero-load in Figure 4.44) is longer for T4 compared to T6 and F compared to T5. This confirms that crack propagation occurs more rapidly in the harder materials.

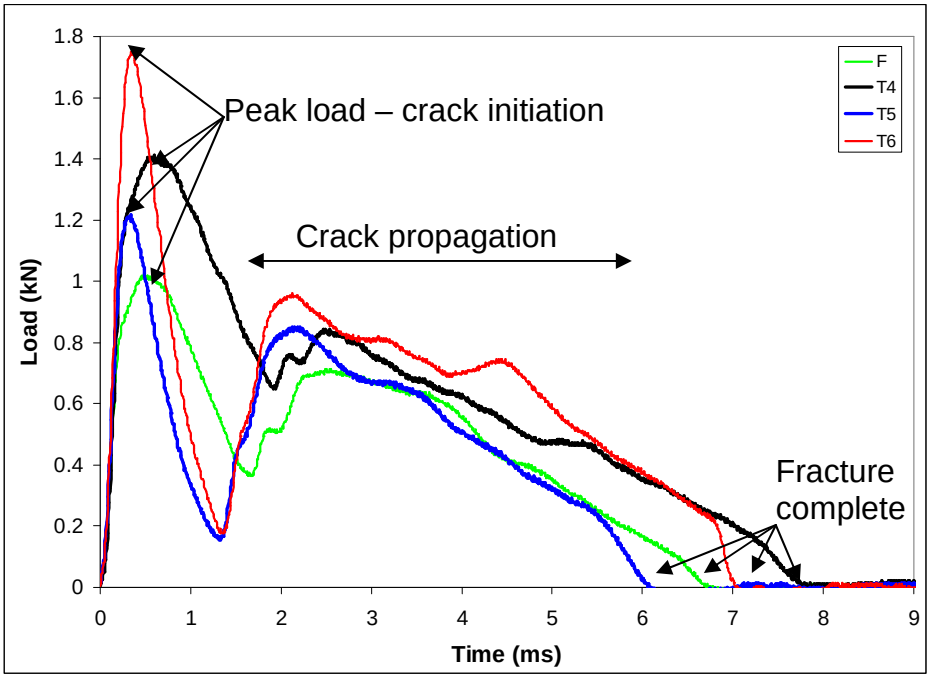

Figure 4.44: Impact load as a function of time during drop weight testing of SSM-HPDC A356.

The impact load as a function of deflection is shown in Figure 4.45. The total energy (in Figure 4.43) is the area beneath this load vs deflection curve.

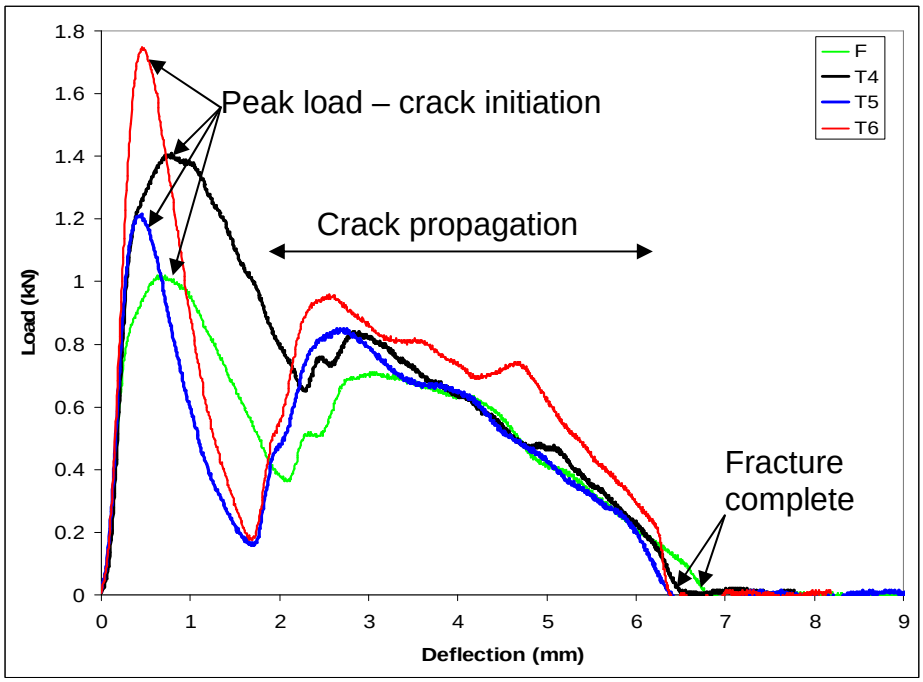

Figure 4.45: Impact load as a function of deflection during drop weight testing of SSM-HPDC A356.

The impact energy as a function of time is shown in Figure 4.46. The narrow peak widths of the T5 and T6 temper conditions (Figures 4.44 and 4.45) result in the inflection points at around 1.5 ms in Figure 4.46.

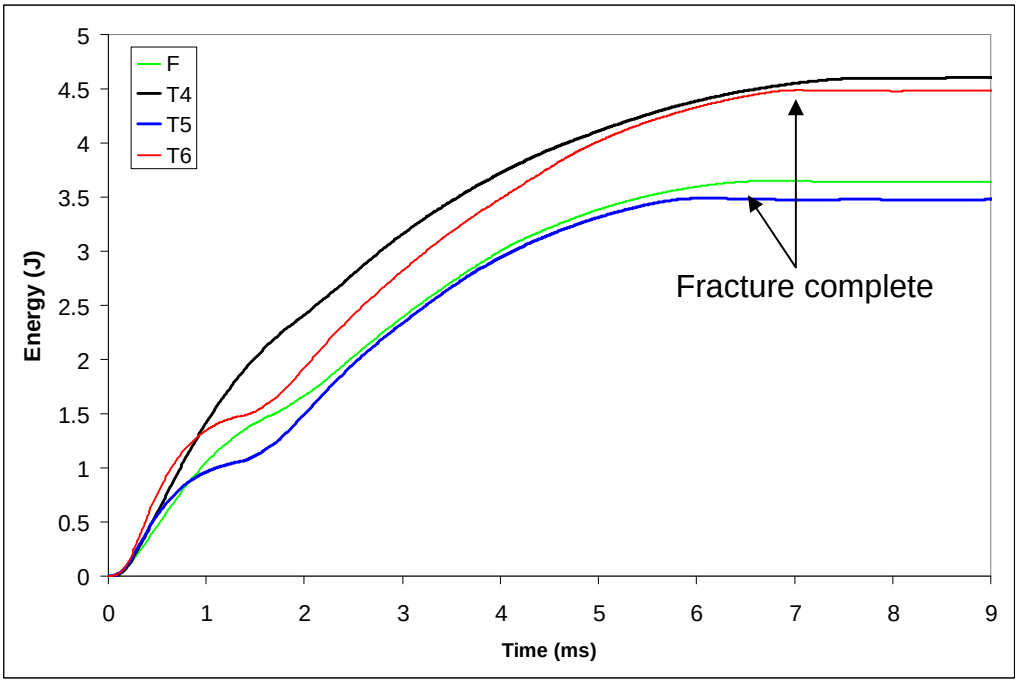

Figure 4.46: Impact energy as a function of time during drop weight testing of SSM-HPDC A356 – fracture is complete once the lines become horizontal.

The peak load value (Figure 4.47) for the T6 condition is higher than for the T4 condition, but the width of the peak is narrower. This is most likely due to the higher strength (hardness) of the T6 material, requiring a higher impact load to initiate the crack. However, after crack initiation, its propagation is much easier through the harder material, causing the narrow peak width compared to the softer T4 material. A similar mechanism is operative when comparing the T5 and F (both with fibrous silicon) temper conditions.

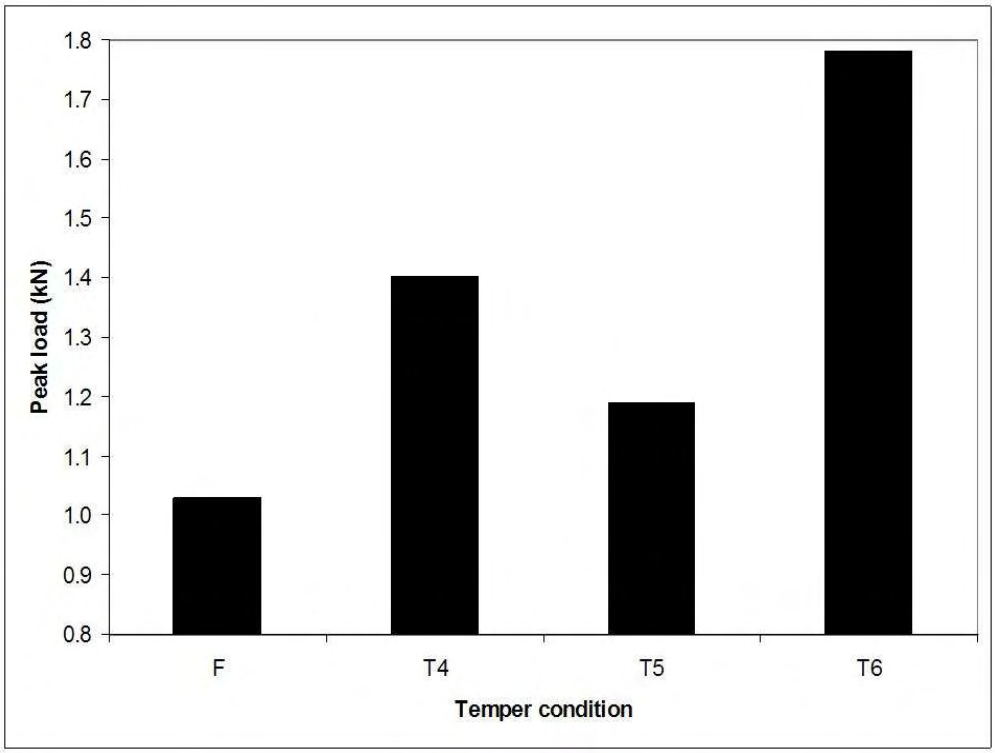

Figure 4.47: Peak load measured during drop weight testing of SSM-HPDC A356.

The cross-section of the fracture surfaces of the tensile and impact tested samples were studied using optical microscopy. It was found that the fracture paths for the different tests in the different temper conditions were similar and, therefore, only the results of A356-T6 are presented. Figure 4.48(a) shows that the crack propagates preferentially through the eutectic regions and not through the softer α-Al globules. Figure 4.48(b) shows a higher magnification micrograph where the fracture completely bypassed an α-Al grain.

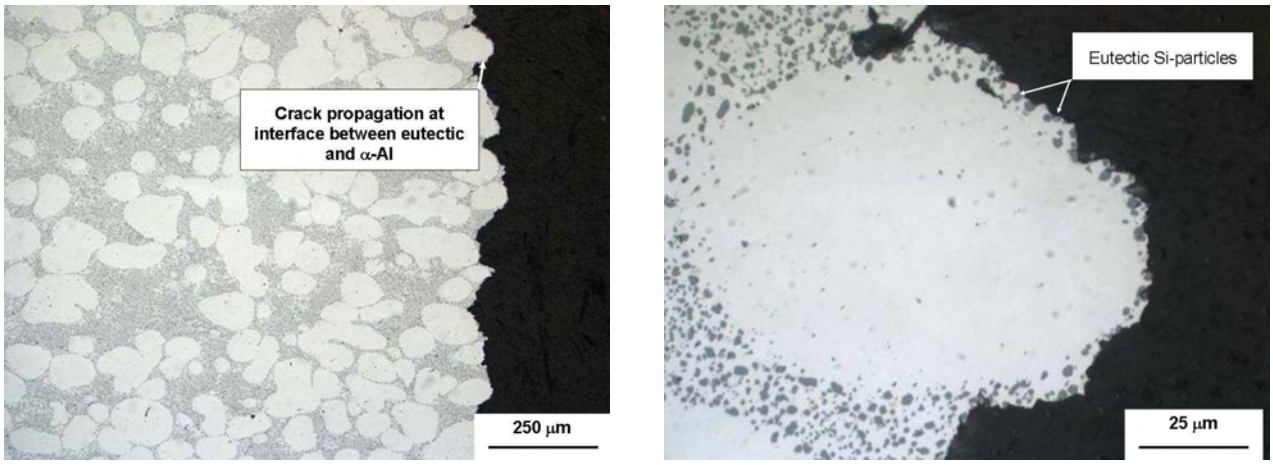

(a) **(b)**

Figure 4.48(a): Fracture path in SSM-HPDC A356-T6 tensile specimen (cross-section of tensile fracture surface) and (b) higher magnification micrograph showing fracture bypassing primary α-Al grain.

Quality Index values of SSM-HPDC A356 (with 0.38% Mg) and F357 (with 0.63% Mg) in different temper conditions are compared in Fig. 4.49. The QI values are higher for alloy F357 than A356 in all the temper conditions. This is due to the higher strengths that can be obtained using the higher Mg-containing alloy F357. The QI values are, however, only marginally higher than for A356. This can be related to the lower ductility achieved for alloy F357 compared to A356 (due, in part, to the higher strength of F357 compared with A356, but also due to the presence of the π-phase in alloy F357 which causes a reduction in ductility).

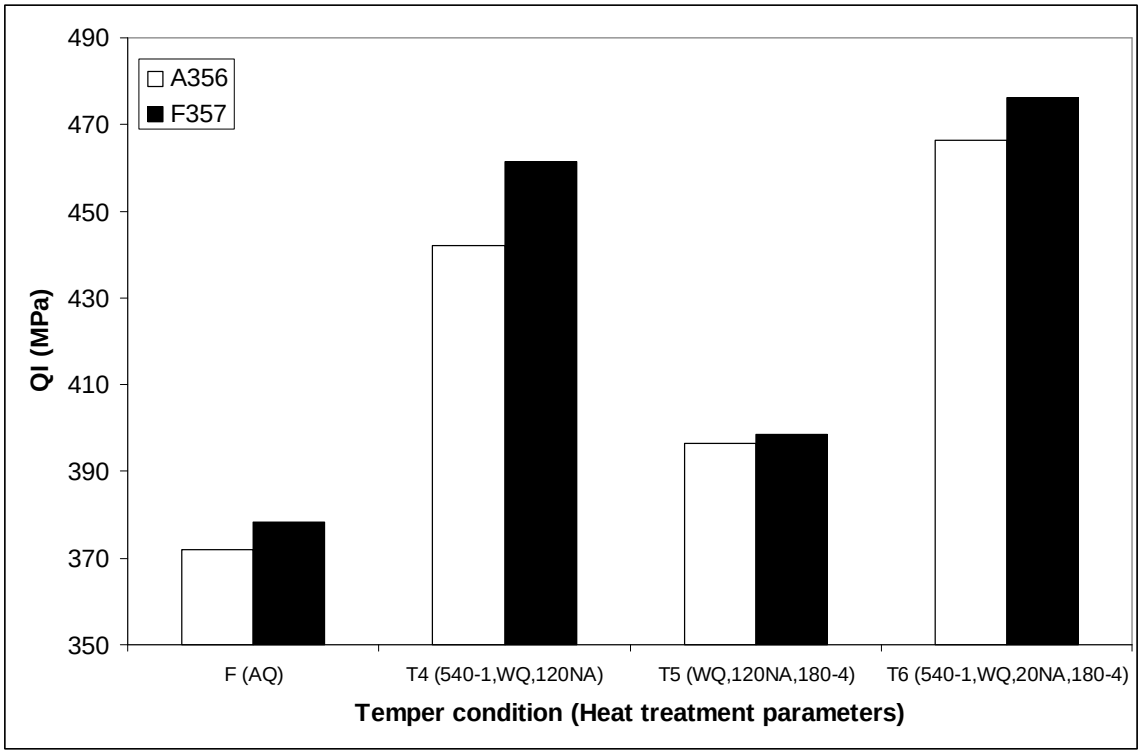

Figure 4.49: Quality index (QI) values for SSM-HPDC Al-7Si-Mg alloys in different temper conditions.

4.9. Surface liquid segregation in SSM-HPDC castings

The surface liquid segregation (SLS) phenomenon in SSM-HPDC castings was studied by using plates with 0.36% Mg in Table 3.1 [HM5]. Chemical analysis depth profiles of the main alloying elements determined using OES, are shown in Figure 4.50. Two regions on the plate were investigated, close to the top of the plate and close to the gate (Fig. 4.51).

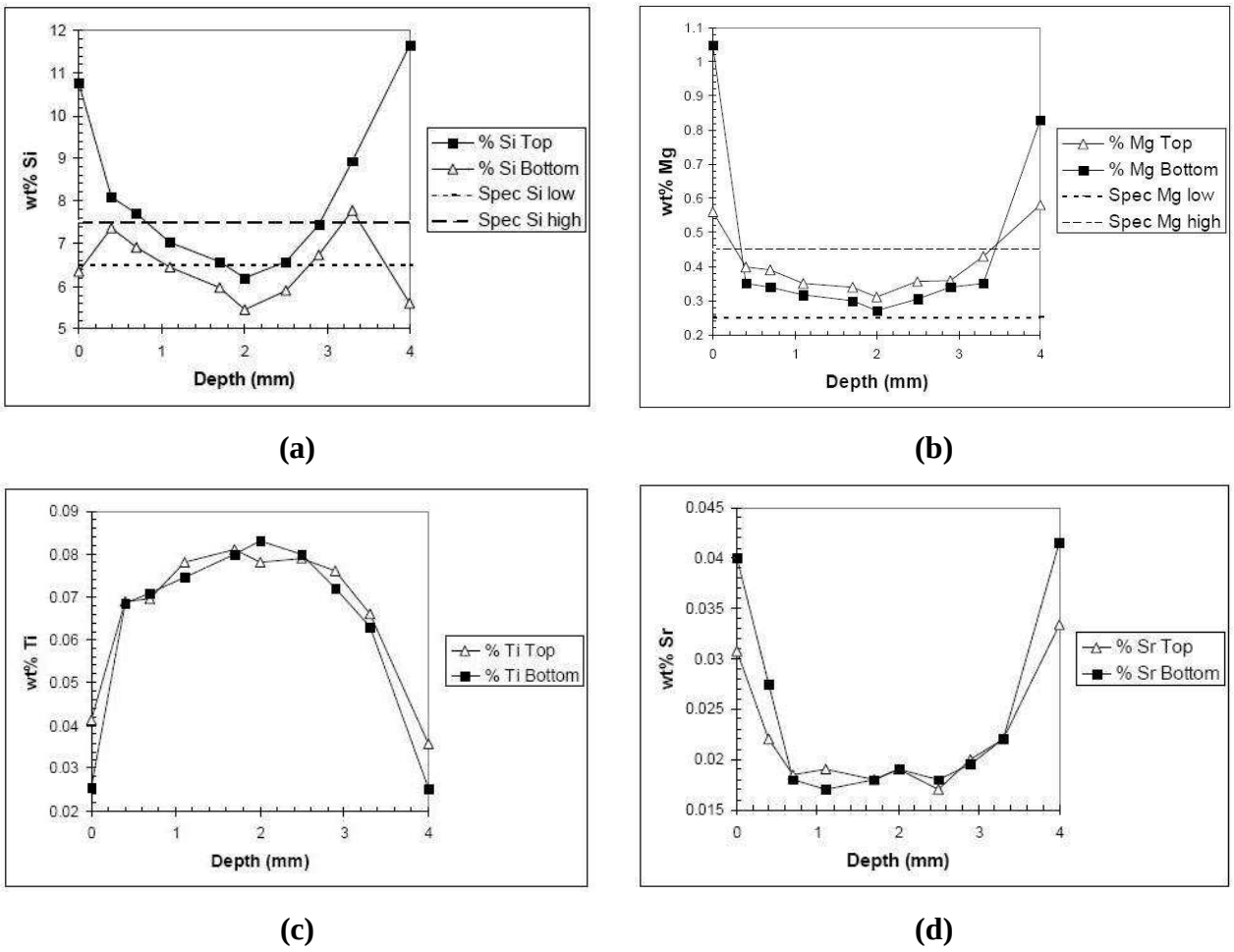

Figure 4.50: OES chemical analyses depth profiles for (a) Si, (b) Mg, (c) Ti and (d) Sr.

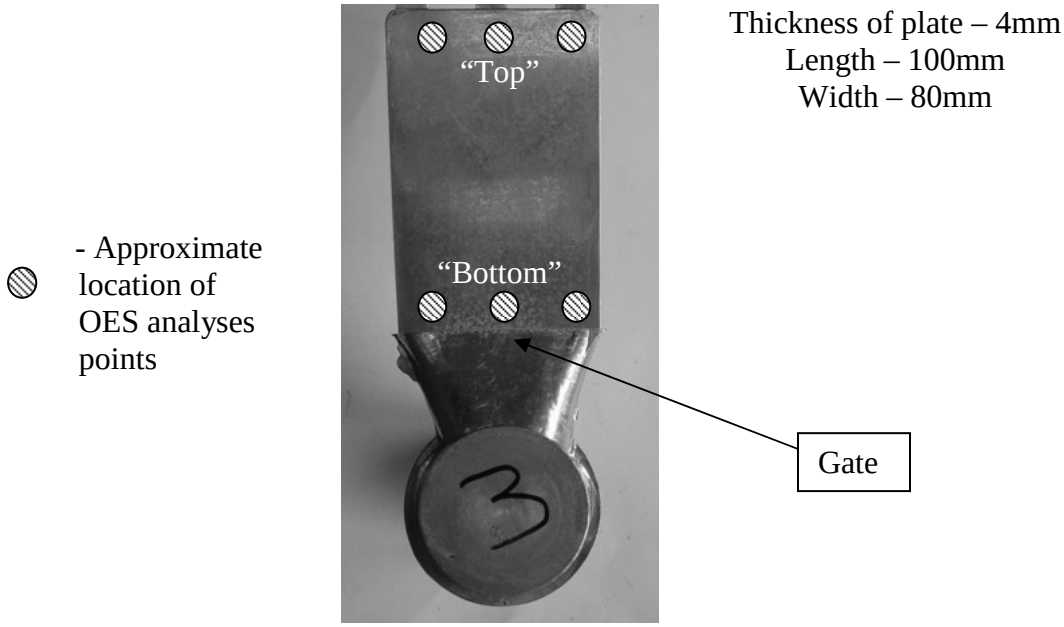

Figure 4.51: Image of a SSM-HPDC plate showing the approximate location for the OES analyses

In the region close to the top of the plate the surface Si, Sr and Mg contents were relatively high while Ti content was relatively low. The Si content drops significantly towards the centre of the plate, dropping below the minimum specification for the alloy. Si, Sr and Mg are typical alloying elements that would be found in the eutectic of the A356 alloy, hence indicating that the regions with high content of these alloying elements were regions of high liquid content. Using the Si high specification as the criteria, it can be seen that the liquid segregation layer can be as high 1.1 mm (measured at the top of the plate). The Ti content displayed the opposite behaviour. This had occurred since Ti was a grain refiner for the primary α-phase and would hence be present where the α grains would be of highest density. At the bottom of the plate, close to the gate, the silicon content was found to be relatively low at the surface, increasing to peak at a depth of approximately 0.4mm on one side of the plate and 0.7mm on the opposite side. The Si content distribution profile through the balance of the cross-section was very similar to that observed at the top. The segregation behaviour observed is as a result of a combination of the gate shape and injection parameters used; these were not optimised for minimising or eliminating liquid segregation for this particular study.

It is evident from these results that the segregation effect is a general phenomenon that occurs on the surface of the component. The region close to the gate shows a slightly different behaviour with a liquid segregation band 0.4-0.7mm below the surface (Fig. 4.50(a)). This had occurred because of a poor gate design resulting in poor filling characteristics around the gate region.

Microstructural analysis of cross-sections close to top and bottom of the castings (Fig. 4.52(a,b)) reveals the presence of the liquid segregation band. The region close to the surface was composed of mainly eutectic while closer to the centre of the casting microconstituents were mainly globular α primary grains and smaller amounts of eutectic. The microstructure at the centre of the casting was more homogenous. It was evident from the solution heat treatments that homogenisation of the surface segregation effects was not possible. Microstructural analysis of the region close to the surface after a T4 heat treatment showed (Fig. 4.52(c)) that there was a structural change in the eutectic structure only, namely spheroidisation of the Si.

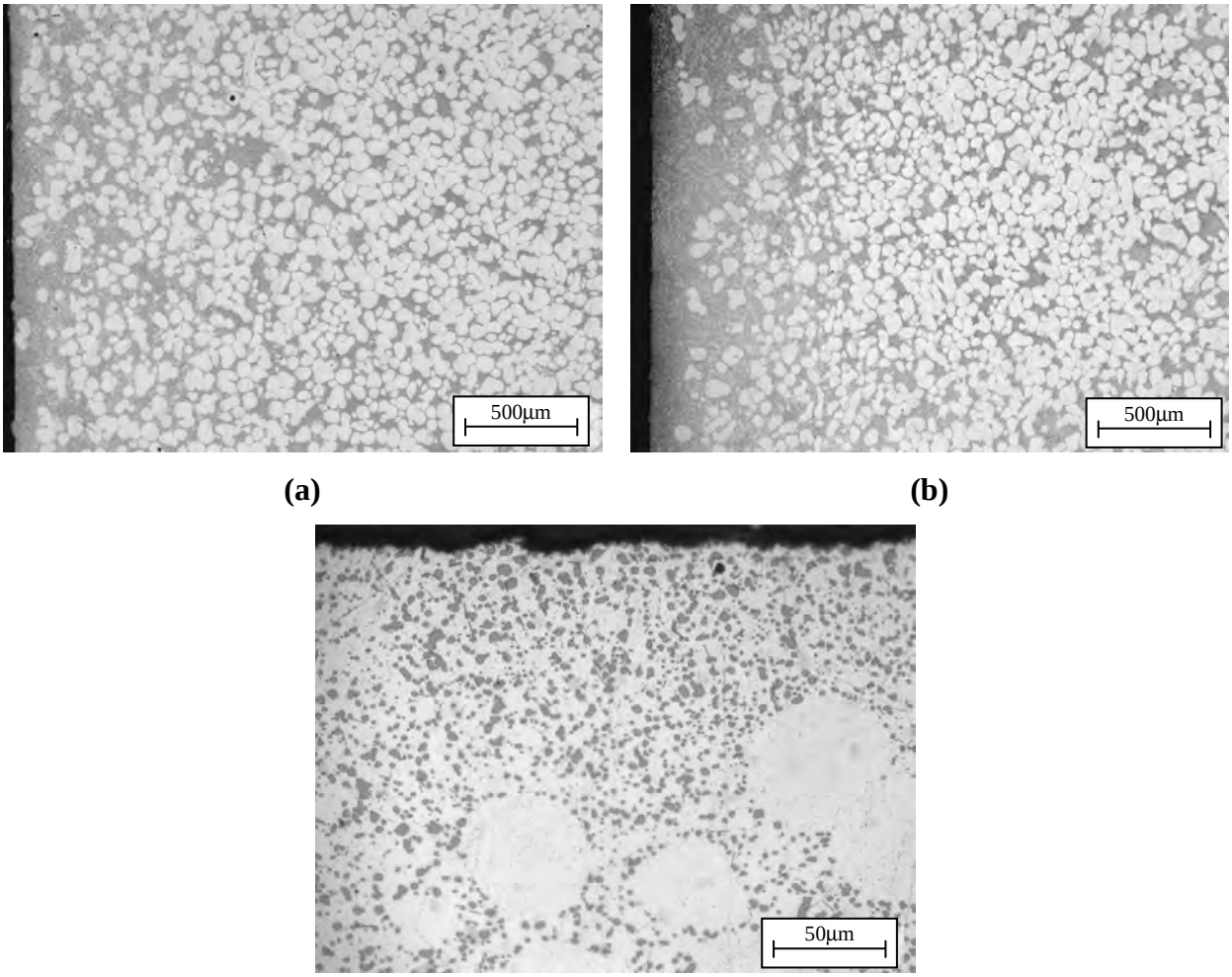

(a) **(b)**

(c)

Figure 4.52: Micrographs of cross-sections (a) close to the top, (b) close to the bottom and (c) after T4 heat treatment (540ºC for 6 h followed by natural aging for 120 h).

It has also been reported that the surface regions of conventional liquid HPDC components is of higher solute content than the centre [111]. This has been ascribed to the presence of externally solidified grains (ESG's). ESG's are large dendritic grains that are formed in the shot sleeve during conventional liquid HPDC, with fine grains solidifying inside the die cavity. These two grain populations mix in dissimilar proportions across the casting cross section, with a prevalence of the fine grains near the surface (skin) and the ESG's at the centre (core) [112]. The distribution of large ESG's at the centre of the cross section of HPDC castings is thought to be due to shear-induced migration of the ESG's during die filling from regions of high to low shear rate (i.e. toward the core of the casting) [111]. The ESG's have a low solute content and their migration to the centre results in surfaces with higher solute content.

Additional macrosegregation in HPDC components has also been ascribed to a combination of inverse segregation and exudation [111]. Inverse segregation is caused by the backflow of enriched liquid through the mushy zone in the dominant direction of heat flow (i.e. to the casting surface) to compensate for solidification shrinkage. With exudation, enriched liquid is drawn to the casting surface due to a pressure differential between the interior and the surface that occurs as the surface pulls away from the die wall during solidification.

With SSM-HPDC, the purpose of rheoprocessing is to form solid globular grains before the billet is transferred to the HPDC machine. In other words, these globular grains can be considered as ESG's that are formed, not in the shot sleeve, but deliberately during the rheopressing step. Additionally, the globular nature of the solid grains should result in a more suitable pathway for enriched liquid to flow to the surface than an interdendritic pathway in conventional HPDC and the surface layer (as shown in Fig. 4.52) is therefore more pronounced in SSM-HPDC components.

Vickers hardness tests of the as-cast surface and core of the casting (Table 4.18) showed a significant difference. This indicates that the mechanical properties of the surface of the casting will be significantly different to the core of the casting and hardness values therefore performed on the surface of a casting does not give a true indication of bulk hardness properties.

Table 4.18: Hardness of the plates without removing the segregation layer and after the surface segregation was removed.

Temper	Surface VHN	Centre VHN
F	80	77
T4	89	80
T6	122	106

4.10. SSM-HPDC of automotive brake callipers

Automotive brake callipers were also produced with SSM-HPDC (Table 3.3) to determine whether the heat treatment cycles that were developed for the small rectangular plates could also be applied successfully to a larger (and more complex) casting [HM10]. The hardness profiles through a cross section of SSM-HPDC brake calliper side-arms (Fig. 3.13) with 0.31% Mg in different temper conditions (F or as-cast, T4, T5 and T6) are shown in Fig. 4.53. The thickness of the side-arm at this selected position is seen to be 20 mm. The hardness values of the surface (at depths of 0 and 20 mm respectively) are significantly higher than the interior (which is constant for all temper conditions from depths of approximately 2-18 mm). The higher surface hardness is due to surface liquid segregation that occurs with SSM-HPDC (Fig. 4.54).

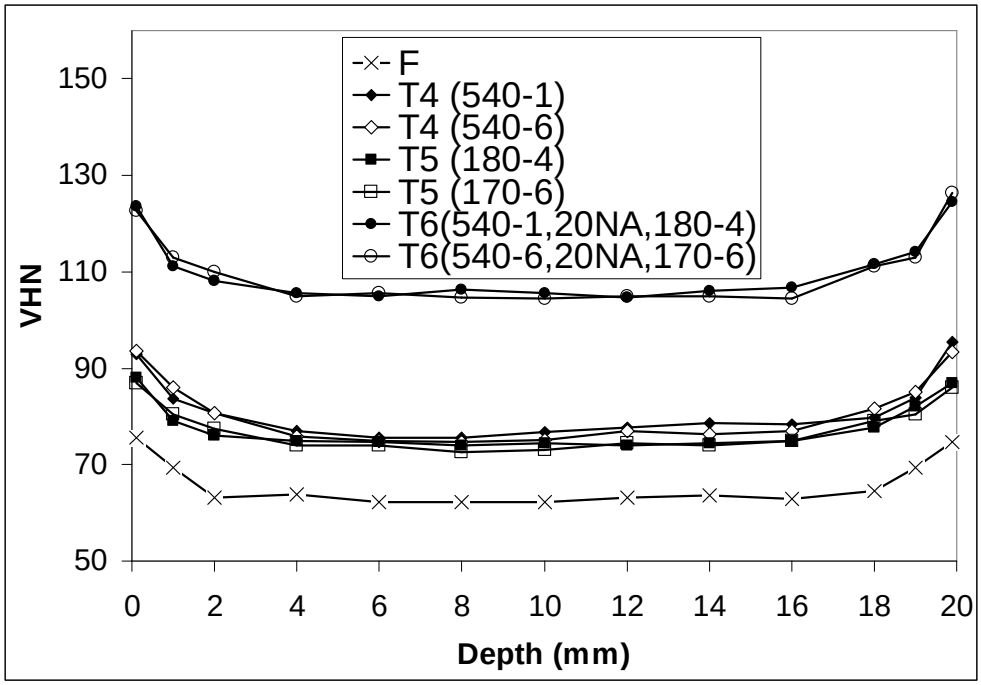

Figure 4.53: Hardness profiles through a cross section of SSM-HPDC brake callipers heat treated to various temper conditions by short cycles and longer "traditional" cycles.

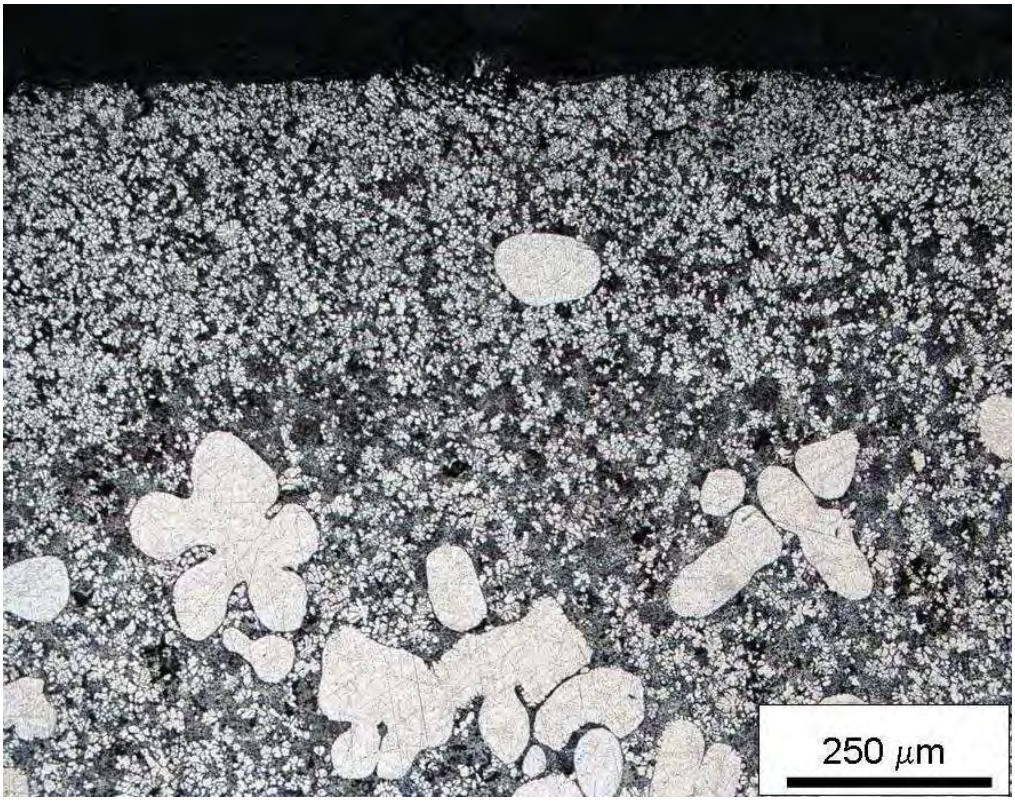

Figure 4.54: Optical micrograph showing the eutectic surface layer found in SSM-HPDC brake callipers.

The hardness profile in the T4 temper condition using the short cycle (540^{o}C for 1 h, quench and natural aging (NA) for 5 days) is very similar to when the longer "traditional" cycle is used (540^{o}C for 6 h, quench and NA for 5 days). Similarly, the shorter T5 cycle (artificial aging (AA) at 180^{o}C for 4 h) results in a comparable hardness profile to the longer "traditional" T5 cycle (AA at 170^{o}C for 6 h). Finally, the short CSIR T6 cycle (540^{o}C for 1 h, quench, NA for 20 h, AA at 180^{o}C for 4 h) results in an almost identical hardness profile than for the "traditional" T6 cycle (540^{o}C for 6 h, quench, NA for 20 h, AA at 170^{o}C for 6 h). Figure 4.53 illustrates that shorter heat treatment cycles can be employed on larger castings to obtain significant energy savings and increased productivity without the loss of properties.

4.11. Comparison of aging response of globular and dendritic Al-7Si-Mg alloys

4.11.1. SSM-HPDC and GDC automotive brake callipers

The investigation entailed comparing SSM-HPDC brake callipers (globular) to gravity die cast (GDC) brake callipers (dendritic) [HM10]. From Table 3.3 it can be seen that the Mg-contents of these brake callipers are similar (0.35 and 0.36% respectively).

The Mg-content controls the response to age hardening (Fig. 4.34), so for direct comparison of strength after heat treatment, the Mg-composition of the different brake callipers needs to be similar. The Fe-content of the SSM-HPDC callipers is, however, lower than for the GDC callipers, which is actually above the upper limit of the specification (Table 3.3). Iron tends to form intermetallics which have a negative influence on ductility (Fig. 4.38). The microstructures achieved with SSM-HPDC and GDC differ significantly. The SSM-HPDC brake callipers have a globular microstructure (Fig. 4.55(a)), whereas the GDC brake callipers have a dendritic microstructure (Fig. 4.55(b)). It is evident from Fig. 4.55 that GDC produces a much finer microstructure than SSM-HPDC. Image analysis revealed an average secondary dendrite arm spacing (SDAS) of 21µm (standard deviation of 3.6 from 30 manual measurements) in the GDC callipers, whereas the average globule size in CSIR SSM-HPDC callipers was 62µm (standard deviation of 21 from 635 measurements using Image–Pro MC v6.0 imaging software).

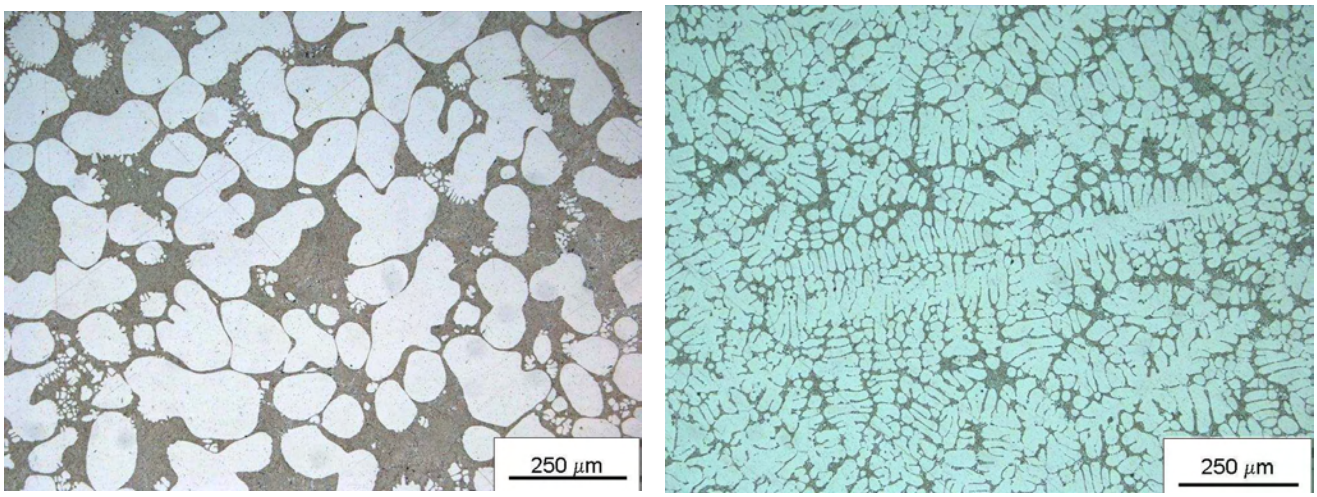

(a) **(b)**

Figure 4.55: Optical micrographs showing the as-cast (F temper) microstructures with MR = 5 (Table 2.2) of automotive brake callipers produced by (a) SSM-HPDC and (b) GDC.

Solution treatment at 540°C for 1 h results in the spheroidisation of the eutectic silicon particles in both the SSM-HPDC and GDC brake callipers (Fig. 4.56).

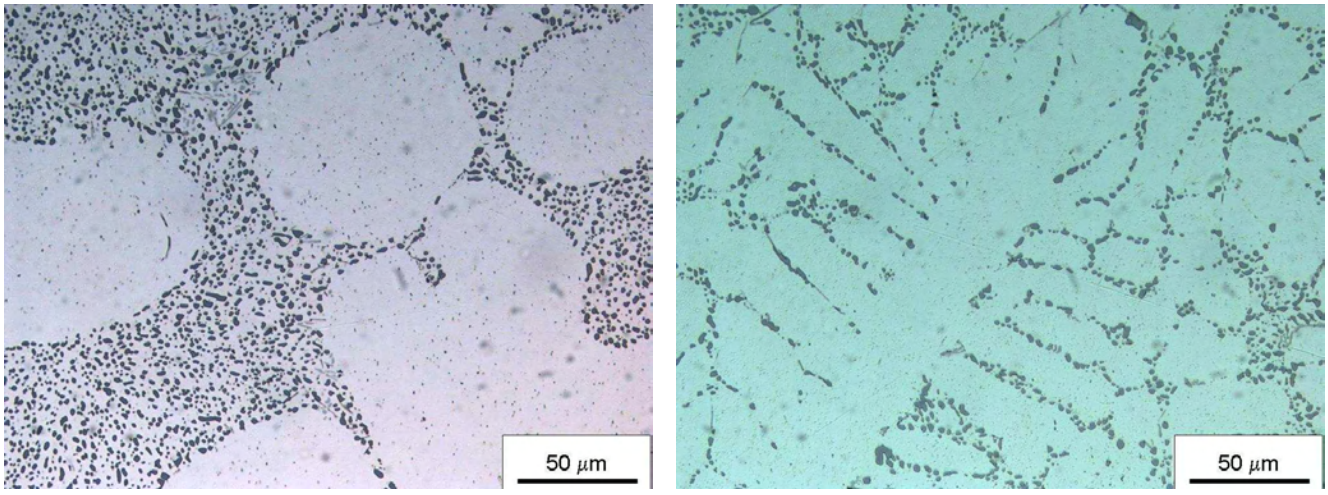

(a) **(b)**

Figure 4.56: Optical micrographs showing the T6 (540°C-1h, 20h NA, 180°C-4h) microstructures of automotive brake callipers produced by (a) SSM-HPDC and (b) GDC.

The Vickers hardness values (VHN) of SSM-HPDC and GDC brake callipers are compared in Fig. 4.57. It can be seen that the hardness values are very similar in both the as-cast (F temper) and T6 temper conditions.

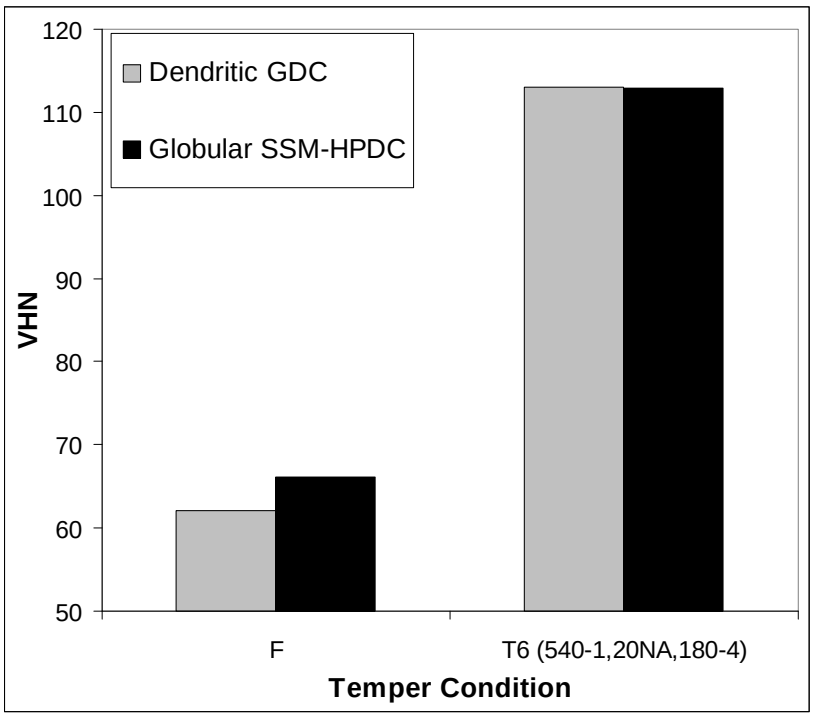

Figure 4.57: Vickers hardness of SSM-HPDC and GDC brake callipers in the as-cast (F temper) and T6 temper conditions.

Also, note that the T6 hardness values are slightly higher than was obtained for the SSM-HPDC brake callipers with 0.31% Mg (Fig. 4.53). This is due to the slightly higher Mg-contents of 0.35 and 0.36% of the alloys in Fig. 4.57.

Comparison of the tensile properties of GDC and SSM-HPDC T6 (540^{o}C-1h,20h NA,180^{o}C-4h) callipers in Table 4.19 confirm the hardness results of Fig. 4.57: the 0.2% yield strengths (YS) and ultimate tensile strengths (UTS) are similar. This result is significant as it shows that dendritic and globular A356 components respond similarly to heat treatment. The lower % elongation after fracture of the GDC calliper as compared to the SSM-HPDC callipers is noteworthy. It is most likely due to the higher Fe-content (Table 3.3) of the GDC calliper, which has an adverse effect on ductility (Fig. 4.38). The differences in Fe-content between the brake callipers make it virtually impossible to determine the effects of globular versus dendritic microstructure on the ductility of A356 in this case.

Table 4.19: Yield strength (YS), ultimate tensile strength (UTS) and % elongation after fracture (%A) of T6 heat treated A356 brake calliper samples. The standard deviation (from 4 values) for tensile properties is also indicated in brackets.

Brake calliper	YS (MPa)	UTS (MPa)	% Elongation
SSM-HPDC (0.35% Mg)	261 (1.4)	317 (3.6)	6.7 (1.9)
GDC (0.36% Mg)	268 (2.1)	315 (4.9)	3.2 (1.6)

Figure 4.34 is redrawn in Fig. 4.58 by also including the data points of the brake callipers in Table 4.19. The data points of the brake callipers correlate well with the data points of the SSM-HPDC plates.

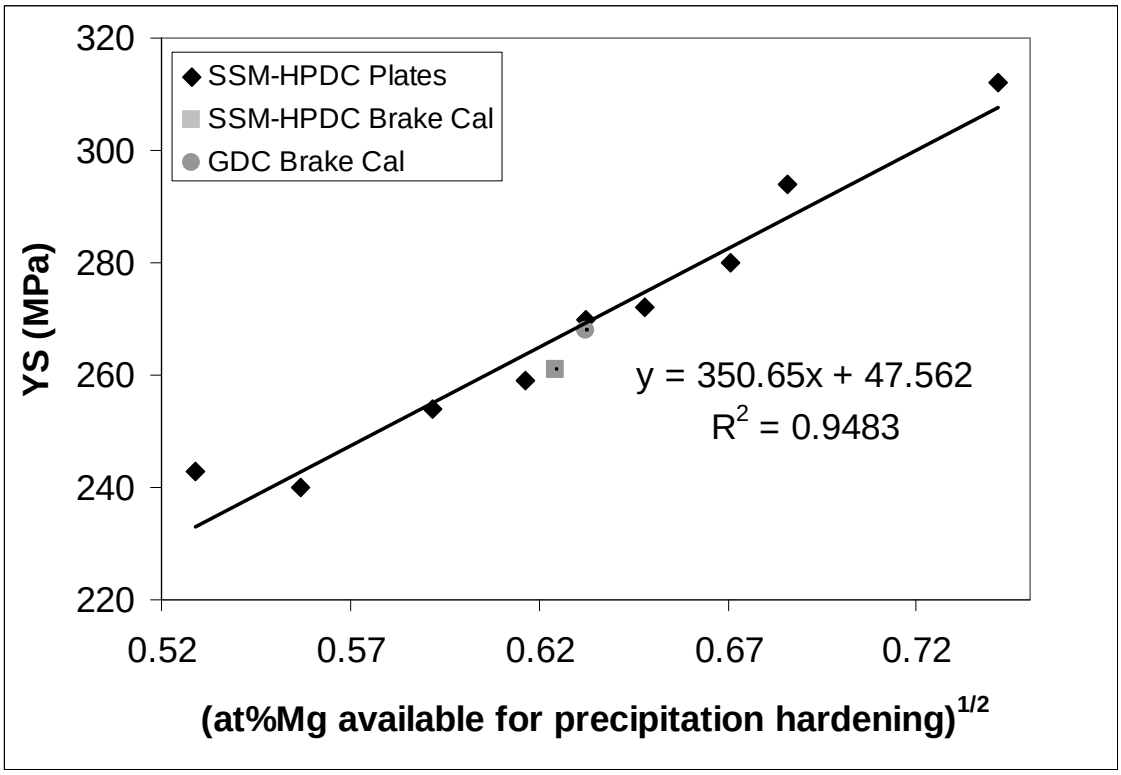

Figure 4.58: YS as a function of (at% Mg-concentration available for precipitation hardening)$^{1/2}$ for the (540-1, {20-120}NA, 180-4) heat treatment applied to SSM-HPDC plates and brake callipers, as well as GDC brake callipers.

4.11.2. Investment cast (IC) plates

Rectangular plates (Fig. 3.10) with composition given in Table 3.4 were cast using investment casting (IC) to obtain a coarser dendritic microstructure than achieved in the brake calliper cast using GDC [HM12]. Optical micrographs for IC-A356 are shown in Fig. 4.59 in the (a) as-cast and (b) T6 temper conditions respectively.

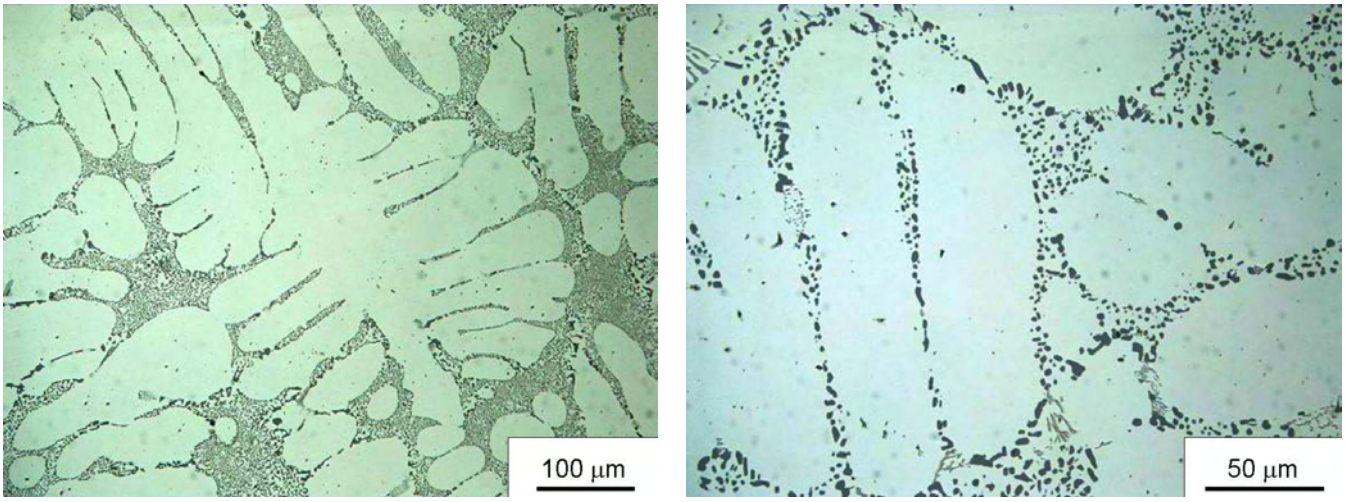

(a) **(b)**

Figure 4.59: Optical micrographs of IC-A356 in (a) the as-cast and (b) T6 temper conditions.

It is evident from Figures 4.55 and 4.59 that IC produced a coarser microstructure than GDC. Image analysis revealed an average secondary dendrite arm spacing (SDAS) of 32µm in the IC callipers (standard deviation of 4.0 from 30 manual measurements), whereas the average SDAS of the GDC plates was 21µm (see section 4.11.1). Solution treatment at 540^{o}C for 1 h resulted in the spheroidisation of the eutectic silicon particles in the IC-A356 (Fig. 4.59(b)). Due to the slow cooling rate during solidification of these plates, a Sr-addition of 300 ppm was necessary to achieve modification of the eutectic Si-particles (Table 3.4). However, the microstructure in Fig. 4.59(a) corresponds to a MR number (Table 2.2) of 4, since some acicular particles are still present.

Figure 4.60 shows artificial aging curves that were determined for SSM-HPDC and GDC brake callipers, as well as IC plates after solution treatment at 540^{o}C for 1 hour, water quenching and no natural pre-aging. The artificial aging response is similar to what was presented in Fig. 4.18 and appears to be independent of whether the microstructure is globular or dendritic. Note that the hardness values are significantly lower for the IC plates than for the brake callipers due to the low Mg-content of the IC plates of only 0.25% (Table 3.4). Artificial aging curves were also determined for these alloys after solution treatment at 540^{o}C for 1 hour, water quenching and 120 hours natural pre-aging, followed by artificial aging (Figure 4.61). Again, the curves are similar to those presented in Fig. 4.18.

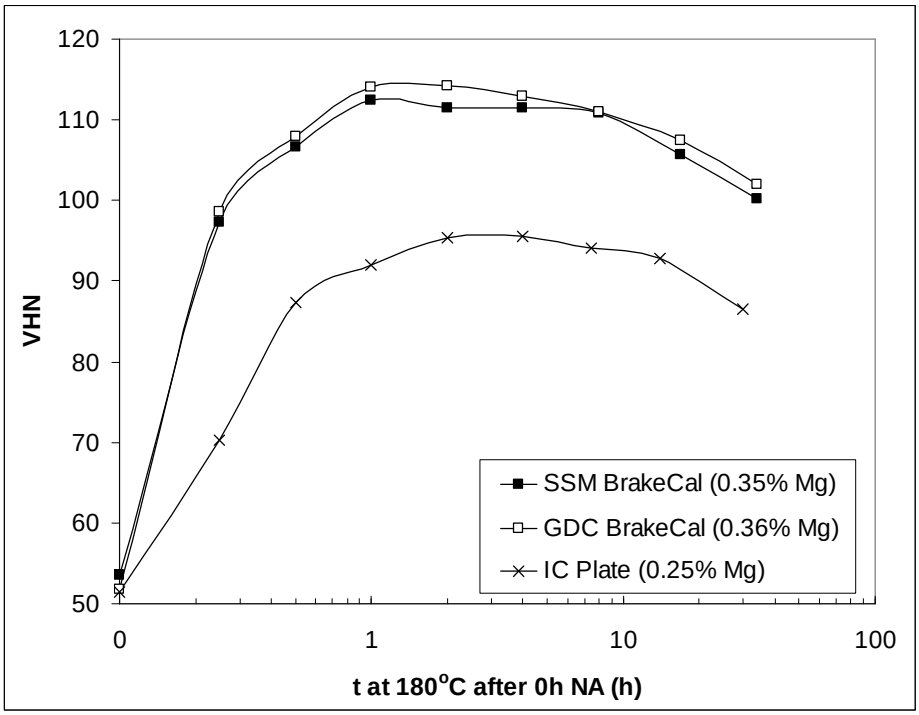

Figure 4.60: Artificial aging curves at 180°C for alloy A356 cast using different casting techniques (after 0 h natural pre-aging time).

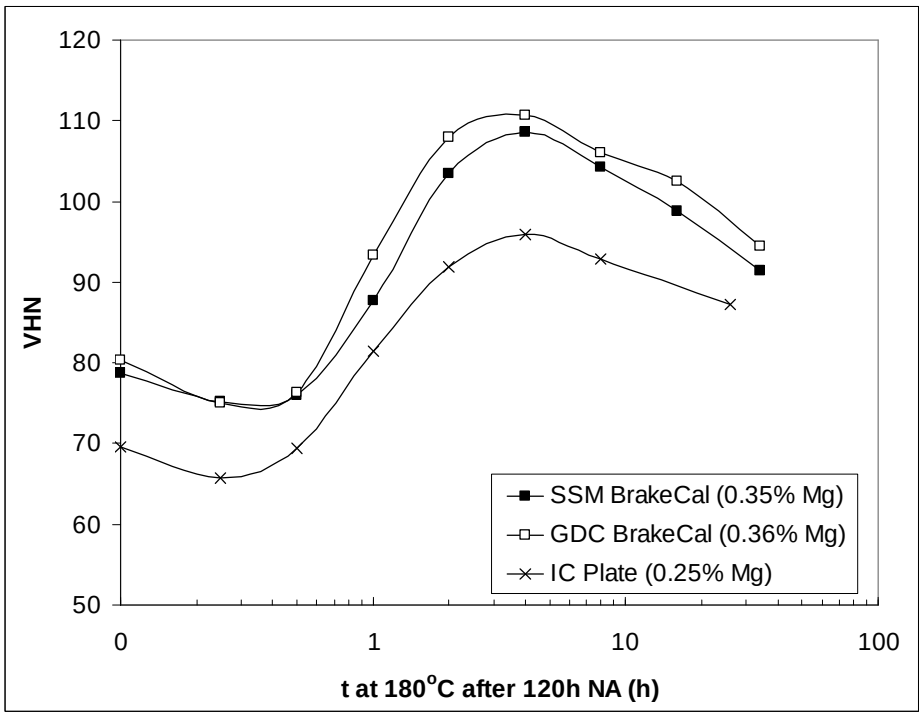

Figure 4.61: Artificial aging curves at 180°C for alloy A356 cast using different casting techniques (after 120 h natural pre-aging time).

No tensile testing could be performed on the IC-A356 plates due to constraints on sample size. In order to make comparisons between the different plates and brake

callipers, hardness was used instead of yield strength (as was done in Fig. 4.58) and the results are shown in Fig. 4.62. Hardness generally correlates better with UTS than with YS since significant plastic deformation occurs with both hardness and UTS determination [82] (see section 4.12). Figure 4.62 is therefore only used as a convenient method of making comparisons of the heat treatment response of Al-7Si-Mg castings produced by different casting techniques. It can be seen that an excellent linear correlation is achieved in Fig. 4.62.

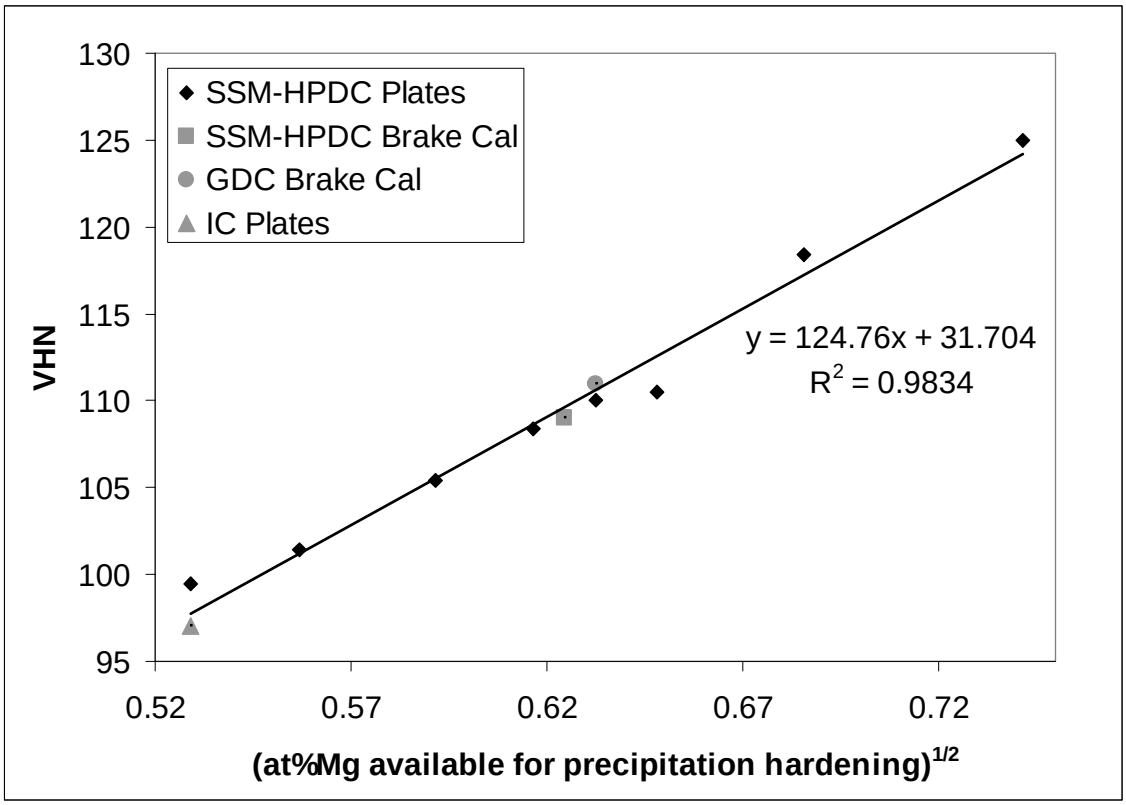

Figure 4.62: VHN as a function of (at% Mg-concentration available for precipitation hardening)$^{1/2}$ for the (540-1, {20-120}NA, 180-4) T6 heat treatment applied to SSM-HPDC plates and brake callipers, as well as GDC brake callipers and IC plates.

4.12. Correlations between hardness, yield strength and UTS in Al-7Si-Mg alloys

As mentioned earlier, direct correlations between yield strength and hardness generally contain an appreciable amount of scatter. This is due to the fact that strain associated with a Vickers indentation is approximately 8% for a variety of strain hardening alloys and hardness therefore generally correlates better with UTS than with YS (where only 0.2% plastic strain has occurred) [82].

The YS and UTS as a function of the Vickers hardness for this work (F, T4, T5 and T6 temper conditions) are plotted in Figures 4.63 and 4.64 respectively.

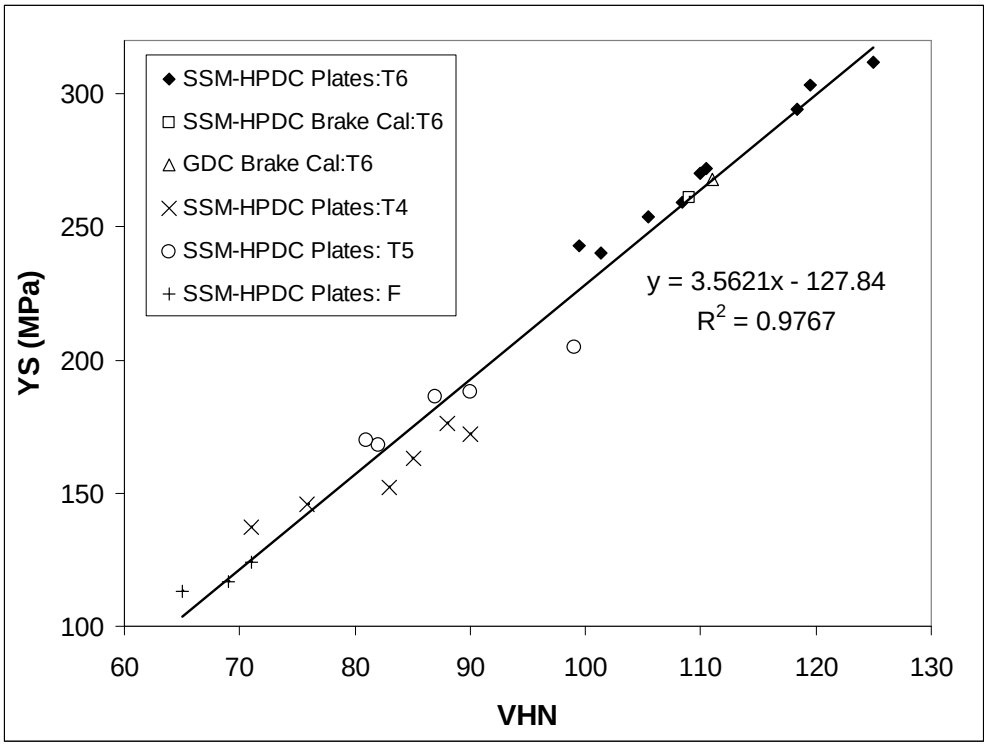

Figure 4.63: Correlation between YS and VHN for Al-7Si-Mg alloys in the F, T4, T5 and T6 temper conditions used in this study.

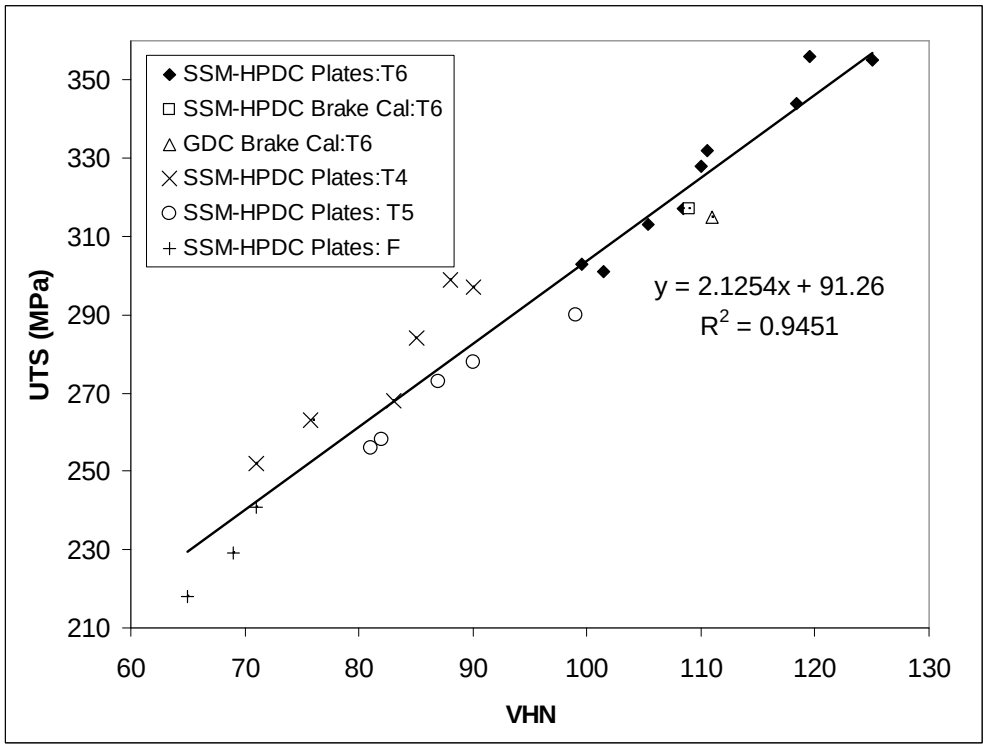

Figure 4.64: Correlation between UTS and VHN for Al-7Si-Mg alloys in the F, T4, T5 and T6 temper conditions used in this study.

From Figure 4.63 it is seen that the correlation between YS and hardness is rather reasonable in the range of hardness and yield strengths tested. From Figure 4.64 it is seen that the correlation between UTS and hardness is comparable to that of YS and hardness in Fig. 4.63. The reason why better correlation with UTS is not obtained with Al-7Si-Mg alloys is most likely due to the fact that UTS is influenced by the degree of spheroidisation of the eutectic Si particles in these alloys. Spheroidised Si-particles tend to result in a higher % elongation, which in turn gives a higher UTS as necking generally does not occur (compare for instance UTS and the % elongation after fracture of the T4 and T5 samples in Table 4.17). The data points in Fig. 4.64 include alloys in which the eutectic Si particles are fibrous (F and T5) and spheroidised (T4 and T6), resulting in a worse-than-expected correlation between UTS and VHN. This suggestion is supported by the fact that most of the F and T5 data points lie below the trend line in Fig. 4.64, whereas the T4 (and to a lesser extent the T6) data points are above the trend line.

Rometsch and Schaffer [82] have proposed an equation (4.7) to convert Brinell hardness (HB) of alloys A356 to A357 to YS by employing the strain hardening exponent (n):

$$\mathbf{YS = 2.95 \times HB \times [0.065]^n} \qquad \mathbf{(4.7)}$$

Accurate n-values from experimental data in this study could not be obtained due to the removal of the extensometer during tensile testing after reaching the 0.2% plastic strain value. However, assuming that the strain hardening exponent is constant over the plastic strain range up to the point of necking during tensile testing of these alloys, an expression for YS/UTS in terms of n alone may be found (eq. 4.8):

$$\mathbf{YS_{0.2\%}/UTS \approx \{(0.002)^n (\exp n)\} /(n)^n} \qquad \mathbf{(4.8)}$$

Equation 4.8 is derived from the Hollomon equation ($\sigma = K\varepsilon^n$), as well as from the conversion equations for engineering strain (e) to true strain (ε) [$\varepsilon = \ln (e+1)$], engineering stress (s) to true stress (σ) [$\sigma = s(e+1)$] and the equivalence of true strain at necking = n [113]. Using the data points in Fig. 4.63 and their respective UTS

values in Fig. 4.64, average n-values for each temper condition can be calculated (Table 4.20).

Table 4.20: Average n-values for Al-7Si-Mg alloys in this study in different temper conditions

Temper condition	Average n-value	Standard deviation
F	0.188	0.0015 from 3 values
T4	0.165	0.0065 from 6 values
T5	0.125	0.0071 from 5 values
T6	0.072	0.0083 from 11 values

The n-values presented in Table 4.20 correspond well to those that could be found in the literature, validating the use of eq. 4.8. Bogdanoff and Dahlström [114] found n-values of 0.17-0.22 for as-cast A356. The evaluated strain hardening exponent for A356/7-T6 according to Wang [115] ranged from 0.045-0.095 depending on the secondary dendrite arm spacing. Rometsch and Schaffer [82] found n-values of 0.088 and 0.078 for their A356 and A357 alloys in the T6 temper condition respectively.

Adapting equation 4.8 slightly to use Vickers hardness rather than Brinell hardness, also minimising $\Sigma(YS_{Measured} - YS_{Predicted})^2$ and ensuring that the intercept of the line of best fit passes through the origin, equation 4.9 is proposed:

$$\mathbf{YS = 3.03 \times VHN \times [0.055]^n} \qquad \mathbf{(4.9)}$$

The predicted YS-values using this equation correlate very well with the measured YS-values (Fig. 4.65).

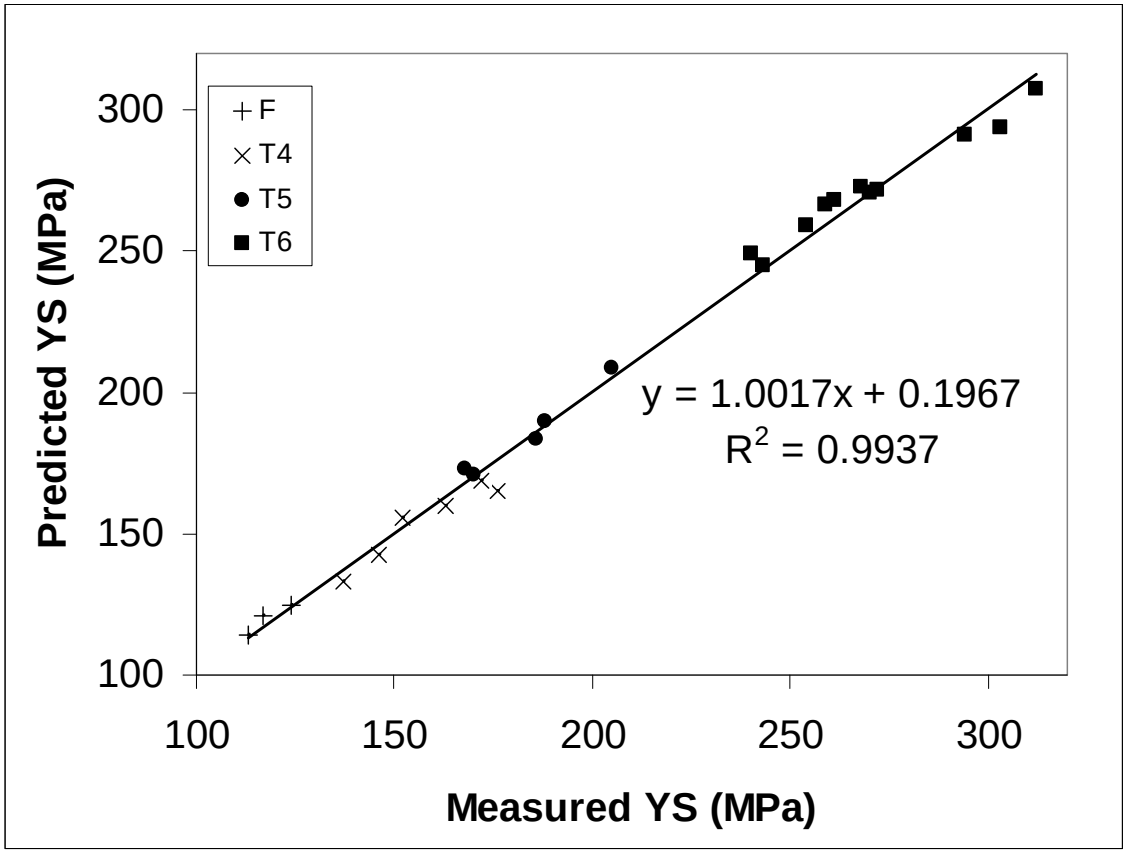

Figure 4.65: Plot of predicted YS (eq. 4.9) against measured YS for Al-7Si-Mg alloys in the F, T4, T5 and T6 temper conditions used in this study.

4.13. Comparison of aging response of SSM-HPDC Al-7Si-Mg alloys with SSM-HPDC 6000 series Al-Mg-Si wrought alloys

Both conventional casting alloys A356/7 and the conventional Al-Mg-Si 6000 series wrought alloys are strengthened by β″, but the influence of especially the high Si content in the casting alloys compared to the wrought alloys is of interest [HM14]. One of the main advantages of SSM-processing is that it is also possible to produce near net-shape components from alloys that are conventionally wrought such as the 6000 series [10,116,117]. By employing SSM-HPDC to A356/7 and the 6000 series alloys, comparable globular microstructures in both series can be obtained. The chemical compositions of alloys 6082 and 6004 can be found in Table 3.6.

Optical micrographs of SSM-HPDC alloys 6082 and 6004 in the as-cast condition are shown in Figure 4.66 (a) and (b) respectively. The globular α-Al that is a prerequisite for SSM-processing is clearly visible in both samples. The inter-globular regions (i.e. the part that was liquid during SSM-processing) of the wrought alloys consist mainly

of fine α-Al (Fig. 4.67), in contrast to the inter-globular regions of the casting alloys which consist mainly of eutectic (α-Al and Si) (Fig. 4.10) due to the high Si content of ~ 7%.

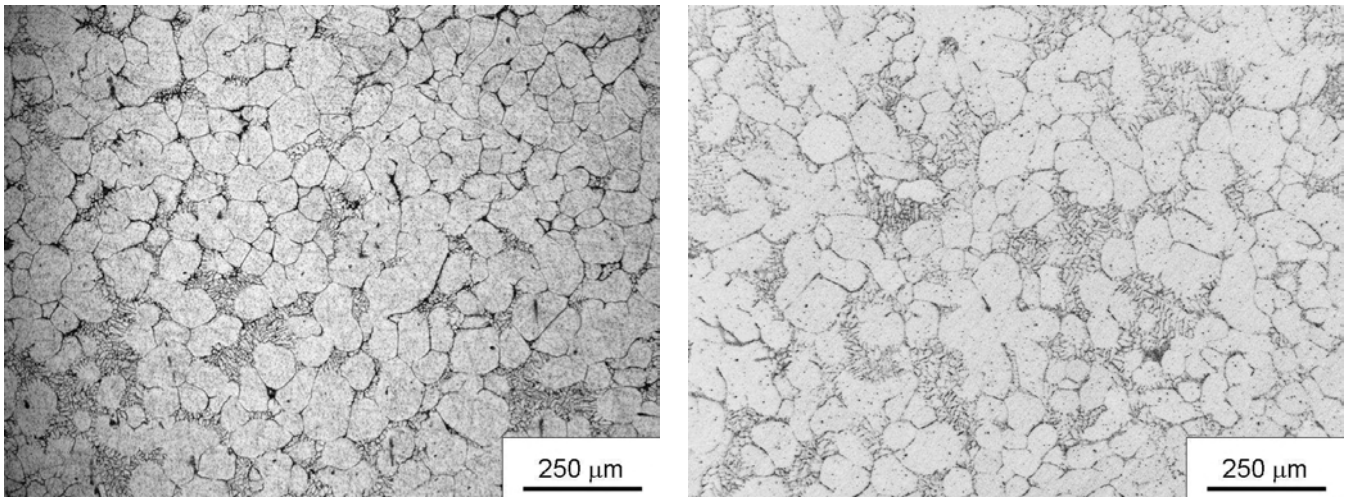

(a) **(b)**

Figure 4.66: Optical micrographs of SSM-HPDC alloys in the as-cast condition for (a) 6082 and (b) 6004.

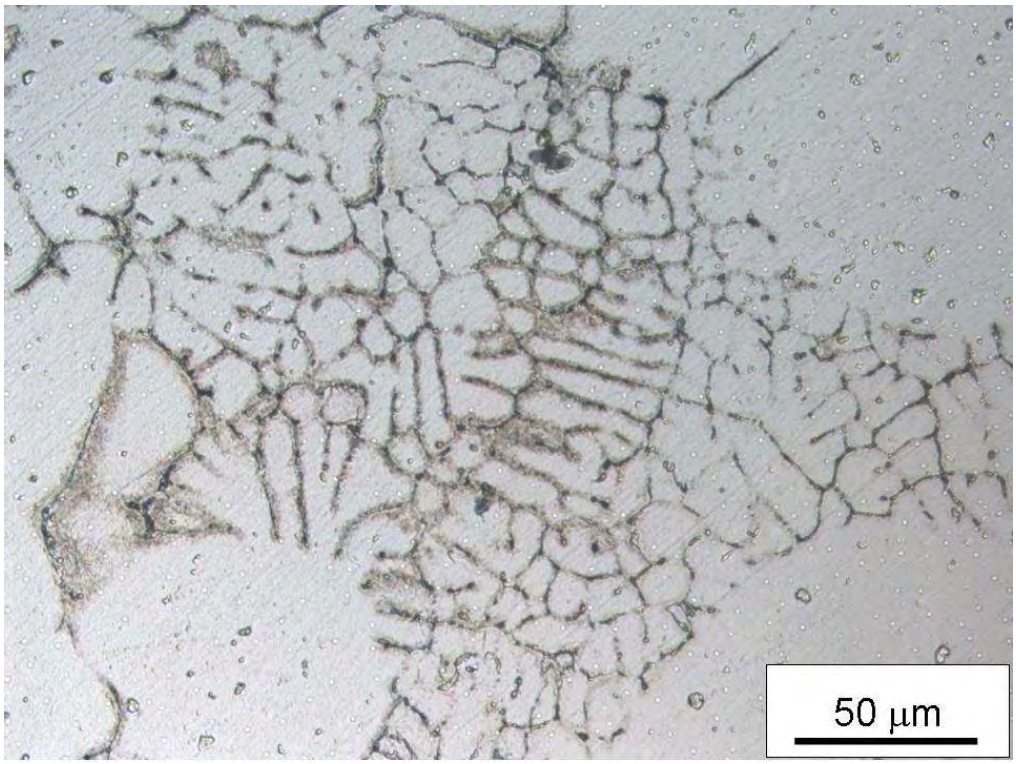

Figure 4.67: High magnification optical micrograph of SSM-HPDC alloy 6004 in the as-cast condition showing the inter-globular regions.

Optical micrographs of SSM-HPDC alloys 6082 and 6004 in the T6 condition are shown in Figure 4.68 (a) and (b) respectively. The globular α-Al structure is retained in the samples during heat treatment.

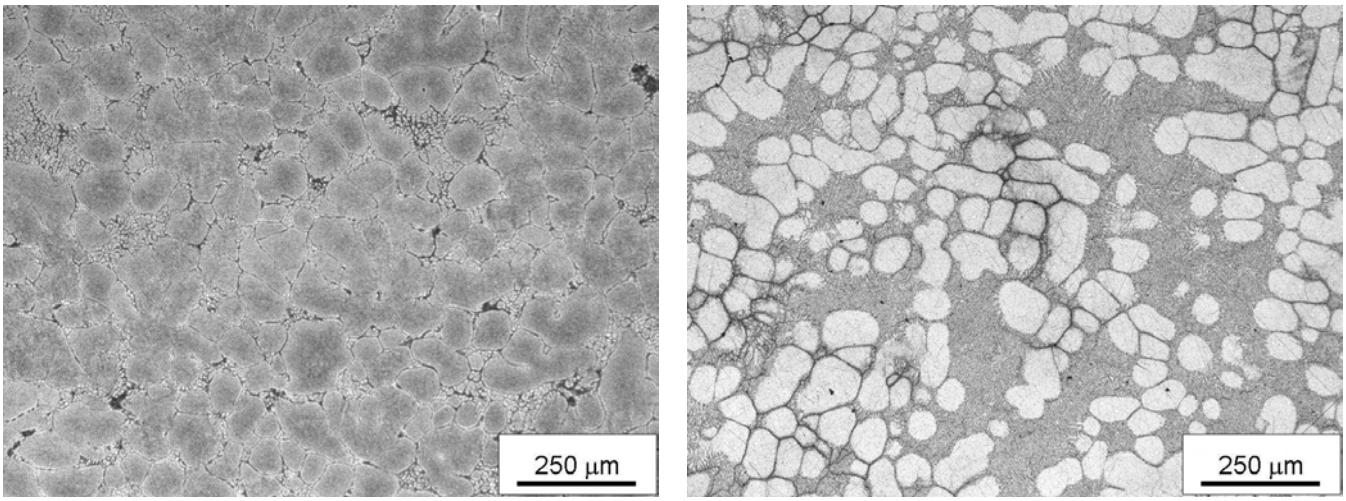

(a) **(b)**

Figure 4.68: Optical micrographs of SSM-HPDC alloys in the T6 temper condition for (a) 6082 and (b) 6004.

As was shown in section 4.9, the nature of the SSM slurry with solid spherical grains suspended in liquid makes it susceptible to liquid segregation during forming processes. An example of the surface liquid segregation (SLS) layer found in alloy 6004-T6 is shown in Figure 4.69. The solution treatment step during the T6 heat treatment has been found to dissolve the majority of the intermetallic phases, however, it does not reduce segregation of elements in the casting [HM11]. As with the A356 and F357 alloys in this study, this surface layer was removed by grinding before all hardness measurements were performed.

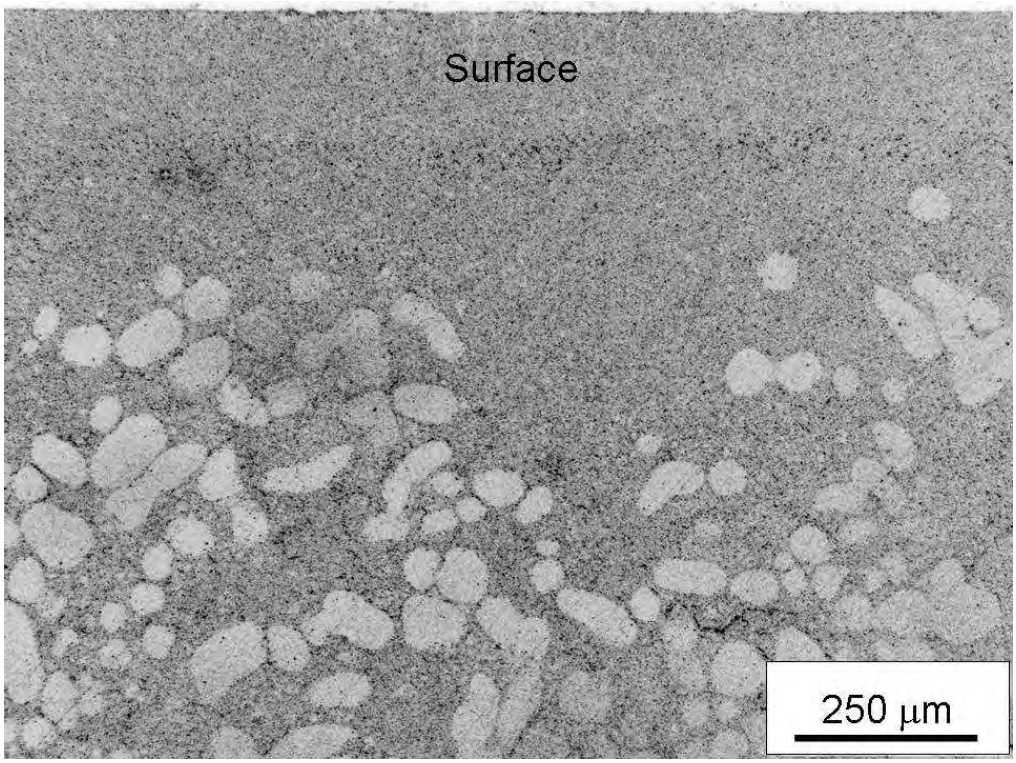

Figure 4.69: Optical micrograph showing the SLS layer in SSM-HPDC alloy 6004-T6.

Figure 4.70 shows artificial aging curves that were determined for the castings at 180^{o}C after solution treatment at 540^{o}C for 1 hour, water quenching and either no or 120 h natural pre-aging. For the casting alloys, aging curves are shown for A356-0.36% Mg (Table 3.1). Considering the effects of prior natural aging on subsequent artificial aging first, it has been shown already that the same maximum hardness can be achieved in A356 regardless of the natural pre-aging time period (Fig. 4.18). Alloy 6082 shows a negative effect of prior natural aging, with the maximum hardness significantly lower when prior natural aging had occurred than without natural aging. This effect is well known for wrought 6082 alloys [84]. Alloy 6004 shows the opposite behaviour, with the maximum hardness being higher when natural aging occurs before artificial aging. This has also been shown to occur before for wrought 6000 series alloys with relatively low Mg and Si contents [85].

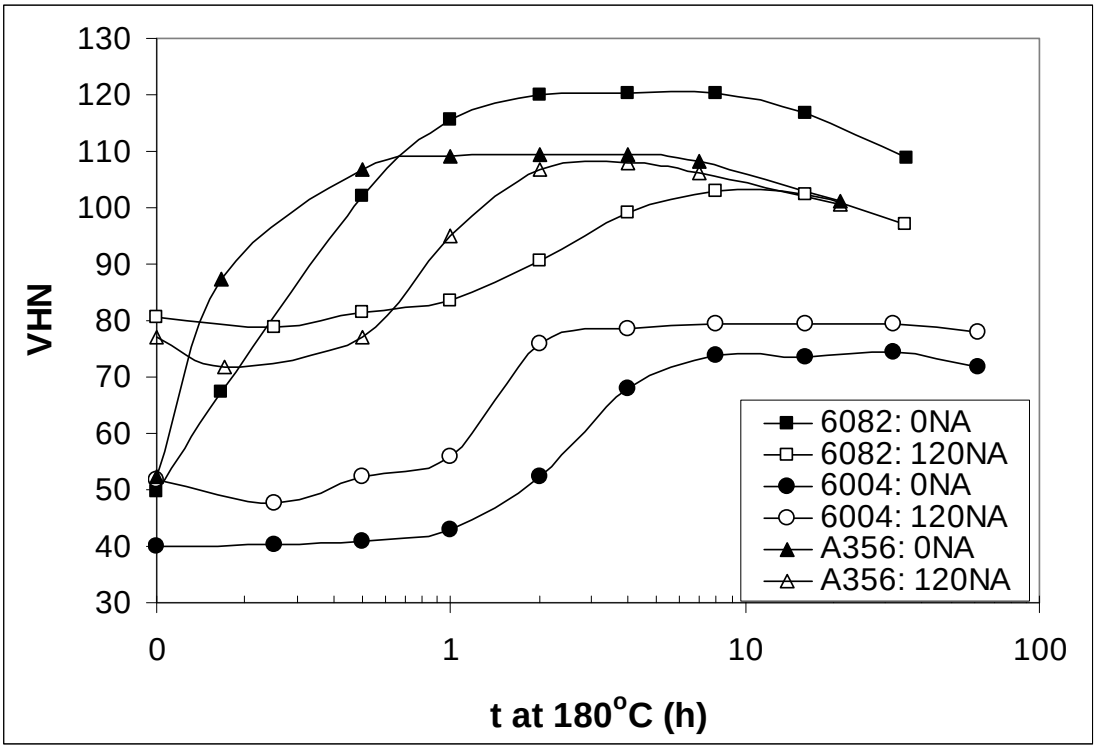

Figure 4.70: Artificial aging curves at 180°C for SSM-HPDC alloys 6082, 6004 and A356 (after either 0 or 120 h natural pre-aging time).

The tensile mechanical properties of SSM-HPDC alloys 6082, 6004 (and A356-0.36% Mg and F357-0.62% Mg for convenience) are shown in Table 4.21. Artificial aging time to peak hardness at 180°C of 4 h was used for A356 and F357 and 8 h for 6082 and 6004 (Fig. 4.70). The tensile mechanical properties are compared for samples that had been naturally aged for 0 or 20-120 h before artificial aging. The tensile results in Table 4.21 are in agreement with the aging curves of Figure 4.70. The strength of SSM-HPDC 6082 is decreased significantly by a prior natural aging period, whereas alloy 6004 displays the opposite behaviour. The strength (YS and UTS) of the casting alloys A356 and F357 are not influenced significantly by a prior natural aging period. It can also be seen from Table 4.21 that alloy 6082 has a strength comparable to alloy F357 when no natural aging of the 6082 occurs and a strength similar to A356 once natural aging occurs. However, this strength is achieved by employing double the artificial aging time at 180°C that was needed for the casting alloys. Also, the Mg requirement to achieve this strength is significantly higher for 6082 than for the casting alloys. The ductility of the 6082 is relatively low if compared to its wrought counterpart and the casting alloys (Table 4.21). Low ductility of SSM-HPDC high performance wrought alloys has been reported before and is related to the distribution

of intermetallic compounds within the coarse eutectic regions [116]. The relatively high ductility of SSM-HPDC 6004 is due to the low strength values that are achieved in this alloy (Table 4.21), in agreement with the low hardness values in Figure 4.70.

Table 4.21: Yield strength (YS), ultimate tensile strength (UTS) and % elongation after fracture (%A) of SSM-HPDC alloys in the T6 temper condition. The standard deviation from at least four values for tensile properties is also indicated in brackets.

	6082		**6004**		**A356**		**F357**	
	0NA	120NA	0NA	120NA	0NA	120NA	0NA	20NA
YS (MPa)	323 (12.9)	278 (6.3)	148 (9.4)	207 (2.2)	273 (6.5)	270 (5.5)	315 (5.2)	312 (4.1)
UTS (MPa)	344 (11.7)	305 (10.3)	189 (5.5)	237 (3.0)	333 (8.4)	328 (5.8)	360 (5.0)	355 (3.9)
%A	4.2 (2.0)	5.4 (2.2)	13.1 (1.0)	12.0 (1.6)	8.4 (2.1)	8.0 (2.2)	5.7 (1.1)	6.0 (1.3)

Bichsel and Ried [87] drew contour plots for 6000 series wrought alloys showing the effect of 24 h natural aging on the change in UTS (MPa) as a function of the Mg and Si content (Fig. 2.32). The contour lines indicate the change in UTS after artificial aging at 165^{o}C for 15 h. This is shown in Figure 4.71, together with the compositions of the 6082 and 6004 used in this study. The change in UTS as a result of prior natural aging is much larger in this case (Table 4.21). The heat treatment cycles and processing techniques (wrought vs. SSM-HPDC) employed in this study are different from the data in Fig. 4.71, which might explain the differences between the two sets of results. The data in Figure 4.71 do not include the Si-composition range of the A356 and F357 alloys of 6.5-7.5% Si. However, the high Si content of these alloys reduces the sensitivity to Mg content – naturally aged alloys A356 and F357 reach the same strength and hardness as the alloys which were not naturally aged before artificial aging for Mg contents covering the whole range of 0.25 to 0.7% (see for example Tables 4.9 and 4.10).

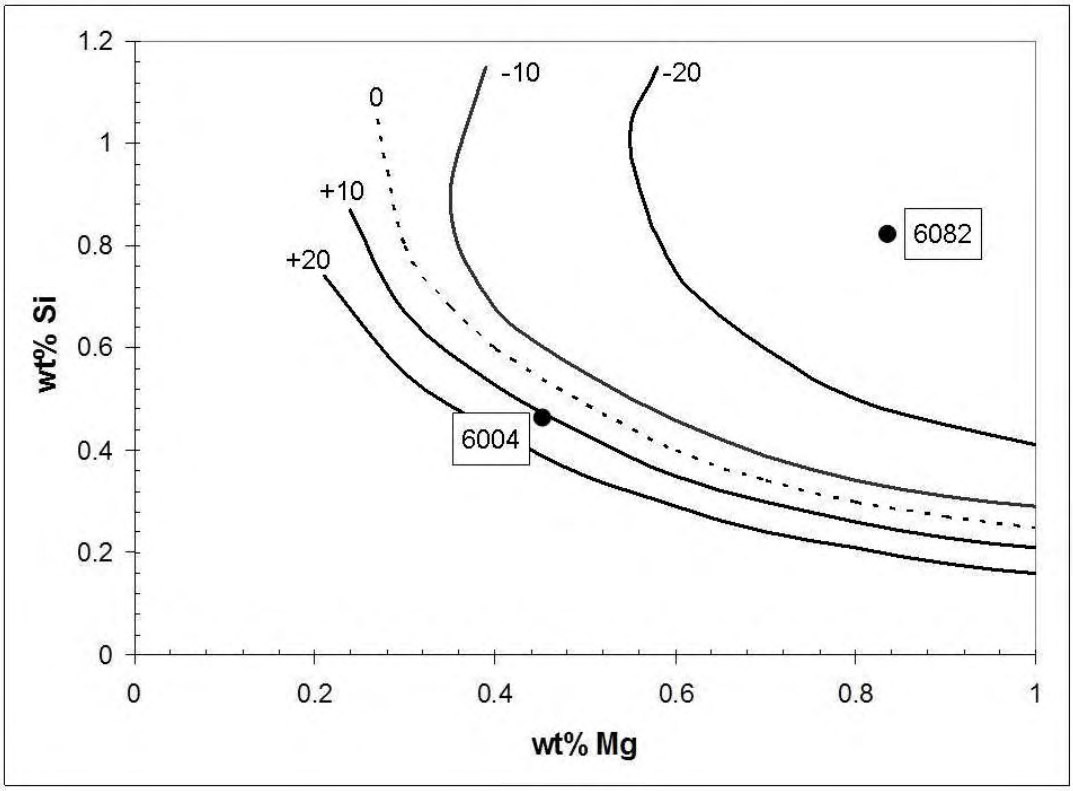

Figure 4.71: Contour plots for 6000 series alloys showing the effect of 24 h prior natural aging on the change in UTS (MPa) after artificial aging at 165°C for 15 h as a function of the Mg and Si content [87]. The present alloy compositions of 6082 and 6004 are also indicated.

4.14. Nanostructural evolution during aging of Al-7Si-Mg alloys

The nanostructural evolution of the 0.49% Mg alloy (Table 3.1) was studied by employing TEM and APT [HM15]. Since APT results are generally presented in terms of at%, the chemical composition in Table 3.1 is presented in Table 14.22 in both wt% and at%.

Table 4.22: Chemical composition of alloy F357 used for TEM and ATP.

	Si	Mg	Fe	Ti	Cu	Mn	Sr	Al
wt%	6.8	0.49	0.13	0.13	0.04	0.01	0.02	Balance
at%	6.6	0.54	0.06	0.07	0.02	0.005	0.006	Balance

4.14.1. Age hardening response and tensile properties

Artificial aging curves following no or 120 h of natural pre-aging for alloy F357 are shown in Figure 4.72. As also shown in Fig. 4.18, a hardness plateau is found between 1 and 4 hours at 180^{o}C following no natural pre-aging. In contrast, a hardness peak is found after 4 h artificial aging following natural pre-aging, with the peak hardness of 120 VHN similar to the plateau hardness. The microhardness values of the primary α-Al and the eutectic components are also indicated in Fig. 4.72. It is seen that the hardness of the primary α-Al is marginally lower than the macrohardness of the alloy, with the hardness of the eutectic being higher. The change of hardness of the eutectic component with aging implies that precipitation hardening also occurs within the α-Al phase of the eutectic. The TEM and APT investigations in this paper relate only to the primary α-Al, but it is seen from Fig. 4.72 that the trends in the aging curves of the alloy (macrohardness) and the primary α-Al are comparable.

Tensile properties of the samples used for TEM and APT investigations are shown in Table 4.23. The results correlate well with the aging curves from Fig. 4.72, with the strength (YS and UTS) of the 120h NA,180^{o}C-10min sample being lower than that of the T4 sample. The strength then increases again for the 120h NA,180^{o}C-1h sample, before reaching peak values for the 120h NA,180^{o}C-4h sample. The samples on the hardness plateau (0h NA,180^{o}C-1h and 0h NA,180^{o}C-4h) have similar UTS values, but different YS values, with the 0h NA,180^{o}C-1h sample having a significantly lower YS than the 0h NA,180^{o}C-4h sample (also see Tables 4.9 and 4.10).

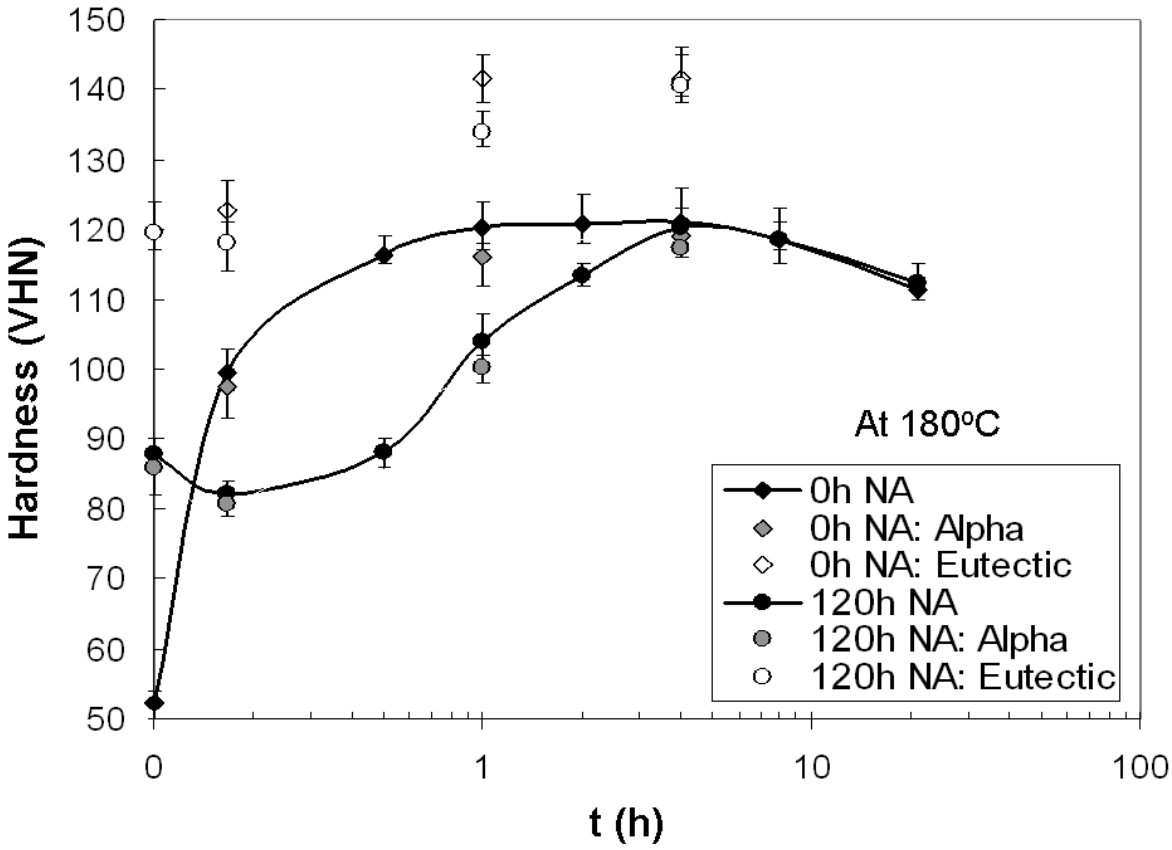

Figure 4.72: Artificial aging curves for alloy F357 following no or 120 h of natural pre-aging (NA), including the microhardness values of the primary α-Al and the eutectic components.

Table 4.23: Tensile properties of SSM-HPDC alloy F357 samples (produced with the 130t HPDC machine) used for TEM and APT analysis. The standard deviation from four values for tensile properties is also indicated in brackets.

	YS (MPa)	UTS (MPa)	% Elongation
T4	176 (4.3)	299 (1.6)	18.0 (2.6)
540°C-1h,120 h NA,180°C-10 min	164 (2.8)	288 (2.6)	20.2 (0.44)
540°C-1h,120 h NA,180°C-1 h	253 (9.5)	335 (3.8)	11.7 (2.6)
540°C-1h,120 h NA,180°C-4 h	303 (3.3)	356 (3.3)	10.6 (1.3)
540°C-1h,0 h NA,180°C-10 min	180 (4.0)	298 (1.6)	19.1 (4.2)
540°C-1h,0 h NA,180°C-1 h	288 (3.0)	362 (1.7)	12.5 (2.4)
540°C-1h,0 h NA,180°C-4 h	304 (1.7)	365 (2.0)	10.6 (1.8)

4.14.2. Nanostructural evaluation

4.14.2.1. Transmission electron microscopy (TEM)

Figure 4.73 shows bright field (BF) images and selected area diffraction patterns (SADPs) recorded with the electron beam near $<001>_{Al}$ for samples that experienced 120 h natural pre-aging before artificial aging at 180°C for up to 4 h, whereas Figure 4.74 shows the same for samples that experienced no natural pre-aging prior to artificial aging at 180°C for up to 4 h. The $<001>_{Al}$ zone axis has been shown to be the best orientation for visualizing the β″ phase [44,118].

There is no indication of precipitation in the bright field images and the SADPs of the T4 sample and the 120h NA,180°C-10min sample in Figures 4.73 (a,b) respectively. The solute clusters that are found in large numbers in Al-alloys in the T4 (Fig. 4.73(a)) and under-aged T6 conditions (Fig. 4.73(b) typically contain only a few to tens of solute atoms [11,78,80]. They are known to be fully coherent with the matrix and are difficult to resolve even by employing high resolution transmission electron microscopy (HRTEM). However, dark contrast arising from GP zones (~ 2 nm diameter) can be seen in the 0 h NA, 180°C-10min sample in Fig. 4.74(a). Faint streaks in the $<100>_{Al}$ SADP of this sample, as shown in Fig. 4.74(a), indicated that there was limited precipitation of β″ [44]. “Cross-shaped” streaks were observed in the $<100>_{Al}$ SADPs of all the samples aged at 180°C for 1 or 4 h, which correspond to weak diffractions produced by the needle β″-precipitates (Figs. 4.73(c,d) and Figs. 4.74(b,c)) [44]. The bright shadows surrounding the needles are reflections of the coherency strains present in the adjoining Al-matrix [44]. The β″-needles increase in size from ~ 2 nm diameter x 10 nm length in the 120h NA, 180°C-1h sample (Fig. 4.73(c)) to ~ 4 nm diameter x 25 nm length in the 120h NA, 180°C-4h sample (Fig. 4.73(d)). Similarly, the β″-needles increase in size from ~ 3 nm diameter x 20 nm length in the 0h NA, 180°C-1h sample (Fig. 4.74(b)) to ~ 4 nm diameter x 25 nm length in the 0h NA, 180°C-4h sample (Fig. 4.74(c)).

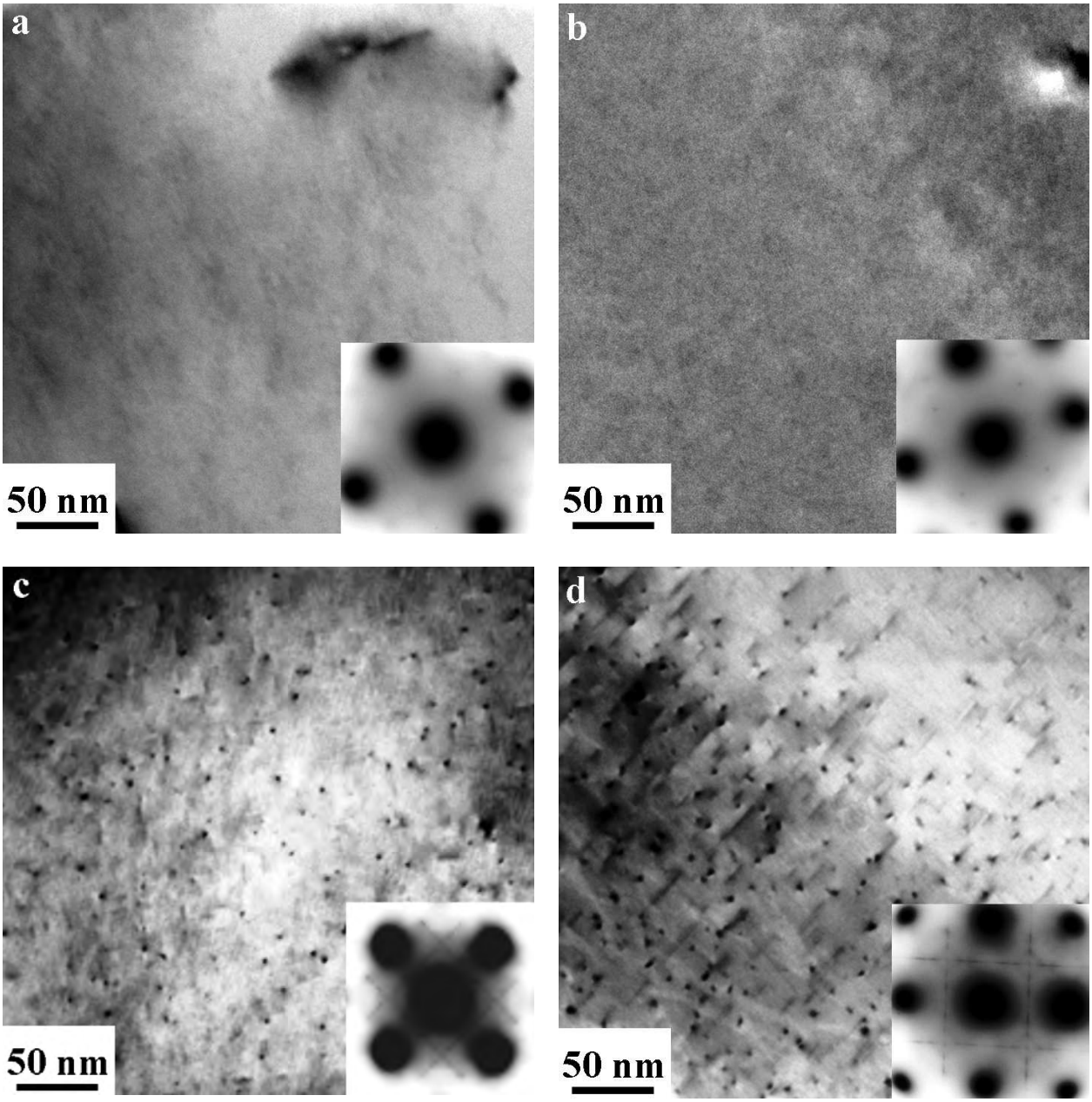

Figure 4.73: Bright field TEM images and SADPs for SSM-HPDC alloy F357 artificially aged at 180^{o}C for (a) 0 min – T4, (b) 10 minutes, (c) 1 h and (d) 4 h after 120 h natural pre-aging.

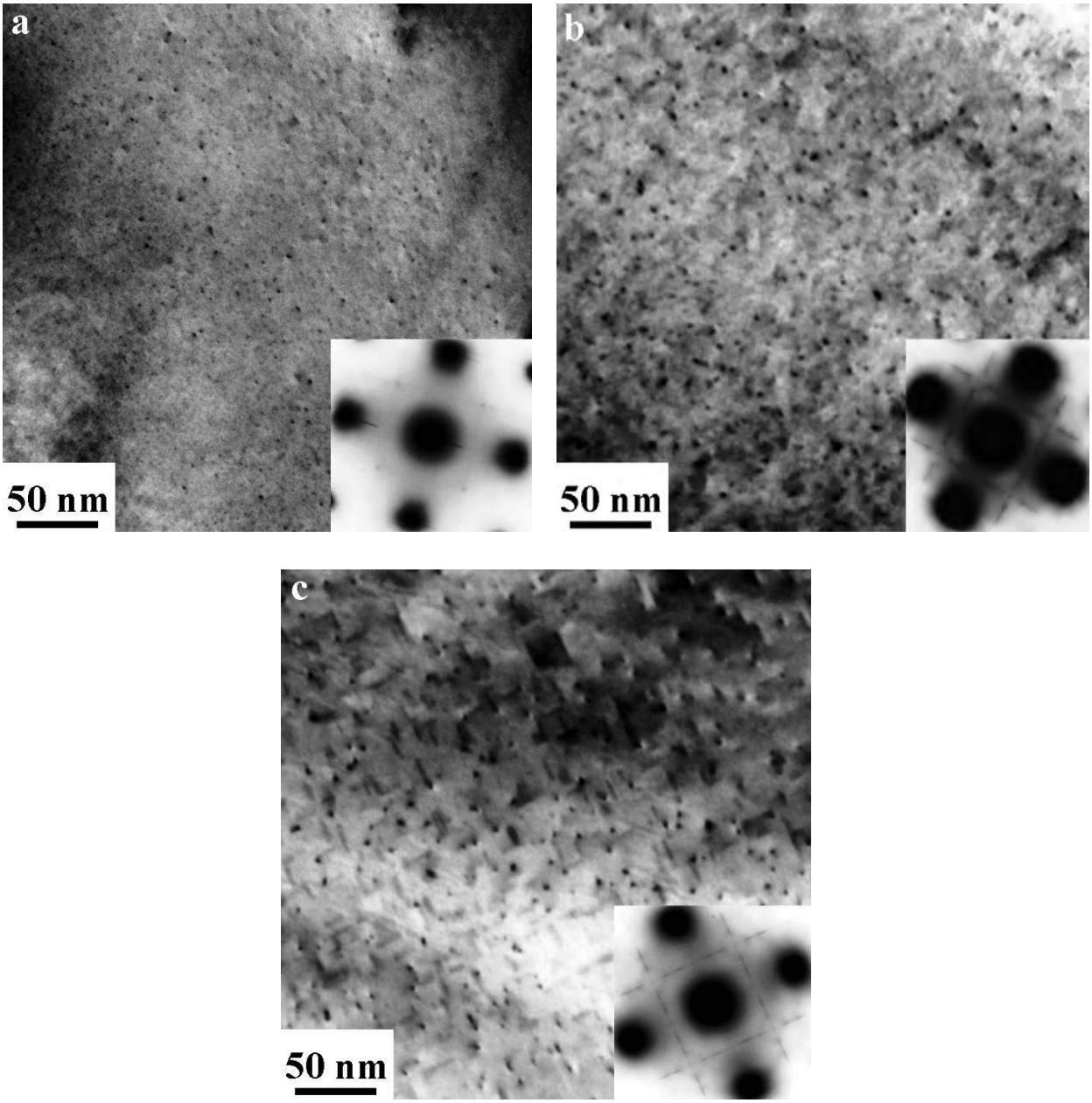

Figure 4.74: Bright field TEM images and SADPs for SSM-HPDC alloy F357 artificially aged at 180^{o}C for (a) 10 minutes, (b) 1 h and (c) 4 h after no natural pre-aging.

4.14.2.2. Atom Probe Tomography (APT)

Figure 4.75 shows three-dimensional (3D) reconstructed Mg atom maps, containing only solute-enriched features of samples that experienced 120 h natural aging before artificial aging at 180^{o}C for up to 4 h, whereas Figure 4.76 shows the same for samples that experienced no natural aging prior to artificial aging at 180^{o}C for up to 4 h. It is difficult to make a scientific distinction between GP zones and clusters of Mg-

Si since they have similar spherical morphologies [39]. GP zones and β″ can be distinguished more readily based on the differences in morphology (spheres vs needles) and also the β″ needles that generally contain more solute atoms than GP zones [42]. Critical sizes of 8 and 30 solutes have been used to distinguish between solute clusters and GP zones in two different wrought Al-Mg-Si alloys [42,78]. The small solute-rich features containing 10-20 detected solute atoms are designated as solute clusters in this study. Considering a detection efficiency of ~55% in APT analysis, a spherical feature of one nm in diameter should contain about 30 atoms. Use of 20 solutes assumes that a third of detected atoms will be Al atoms. Those containing 21-100 solute atoms are GP zones, and elongated β″ contains > 100 solute atoms (Table 4.24). Note that over-aged samples (180°C for > 4 h) were not investigated in this study and that no large β′ rods were detected in any of the analysed volumes (β′ rods typically have diameters of ~ 10 nm and lengths of several hundred nanometers [39]). Thus, even the largest precipitates with n > 1200 in this study refer to β″ rather than β′.

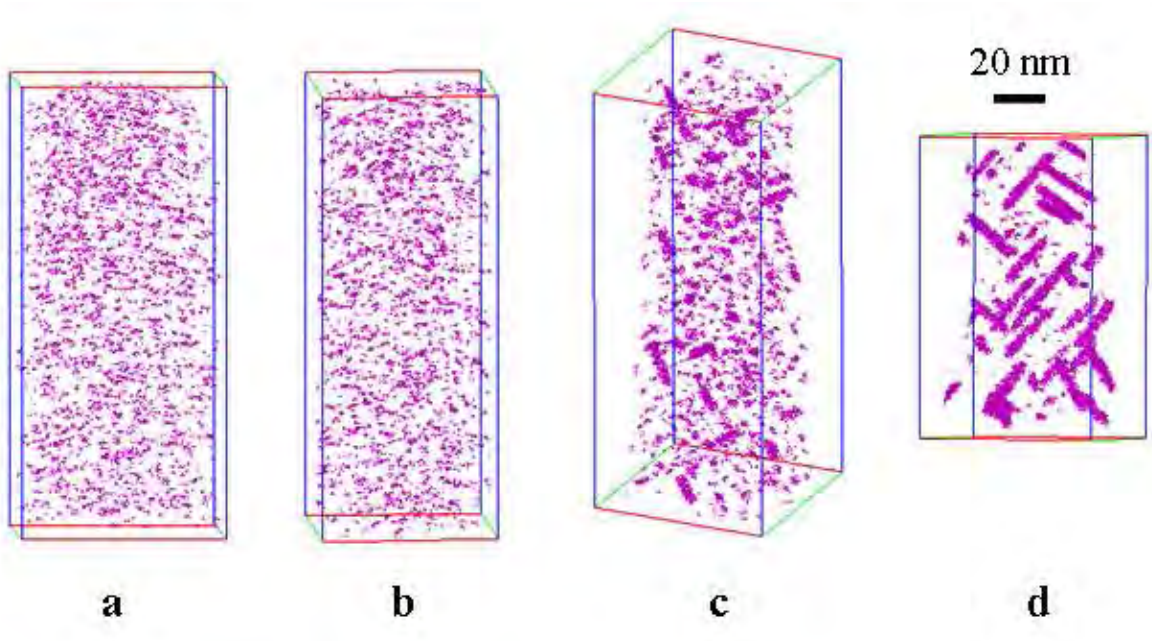

Figure 4.75: 3D Mg atom maps containing only solute enriched features after removing solutes in the matrix of SSM-HPDC F357 alloy samples aged at 180°C for (a) 0 h, (b) 10 min (c) 1 h and (d) 4 h after 120 h prior natural aging.

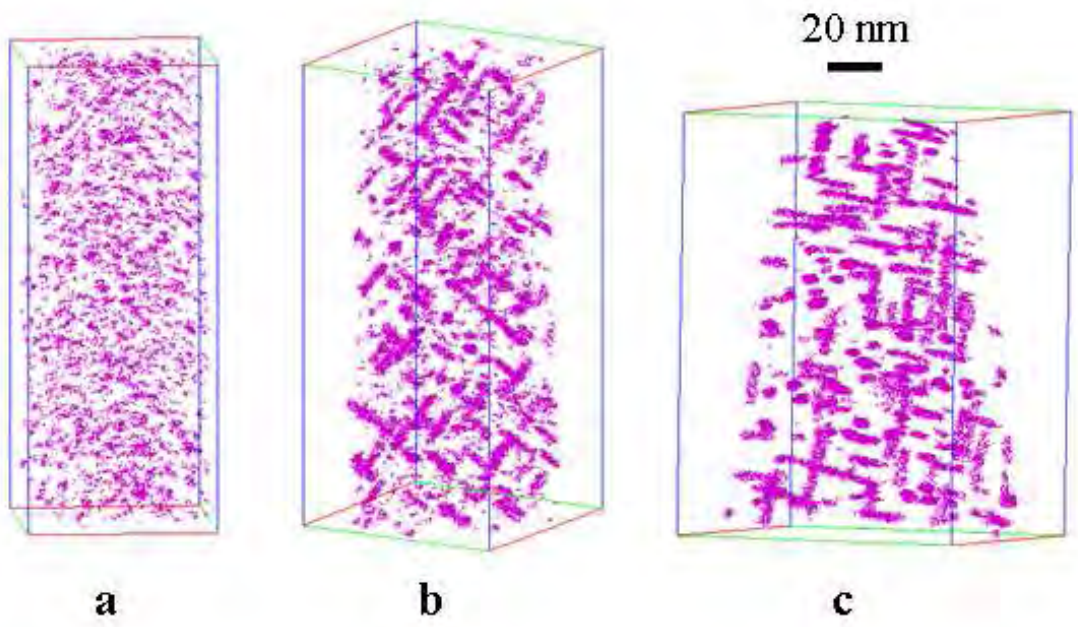

Figure 4.76: 3D reconstructed Mg atom maps containing only solute-enriched features after removing solutes in the matrix of SSM-HPDC F357 alloy samples artificially aged at 180°C for (a) 10 min (b) 1 h and (c) 4 h after no prior natural aging.

Table 4.24: Distinction between solute clusters, GP zones and β″ based on the number of solute atoms (n) detected with APT.

Precipitate	Number of detected solute atoms (n)
Solute clusters	10-20
GP zones	21-100
β″	>100

Only solute clusters and GP zones were observed in the samples in the T4 condition and artificially aged at 180°C for 10 min following 120 h NA, as seen in Figures 4.75 (a) and (b) respectively. In addition to the clusters that were found in Figs. 4.75(a,b), the characteristic needle-shape of the β″-phase was evidenced after artificial aging for 1 h (Fig. 4.75(c)), which corresponds to a significant increase in microhardness of the α-globules (Fig. 4.72). Figure 4.75(d) shows the structure of the peak aged sample, with an apparent higher volume fraction of β″. Figure 4.76(a) shows that more and larger GP zones are found in the sample aged for 10 min at 180°C with no prior NA

compared to Fig. 4.75(b) where 120 h prior NA had occurred, resulting in a higher microhardness value of the former (Fig. 4.72). Continuation of the decomposition of the supersaturated solid solution during artificial aging without prior NA results in a high density network of needle-shape β″ in Figure 4.76(b) after only 1 h, with a significantly higher number density of β″-precipitates compared to Fig. 4.75(c) where 120 h prior NA had occurred. The 0h NA,180^{o}C-1h sample falls within the hardness plateau (Fig. 4.72) and already has the same hardness than that of the 0h NA,180^{o}C-4h sample (Fig.4.76(c)). However, the β″-precipitates appear to be smaller in the 0h NA,180^{o}C-1h sample compared to the 0h NA,180^{o}C-4h (Figs. 4.76(b,c)), in agreement with the TEM micrographs in Figs. 4.74(b,c).

4.14.2.3. Chemical composition evolution of the matrix

The evolution of the Mg- and Si-contents of the matrix during artificial aging is illustrated in Figure 4.77. The Mg and Si contents of the sample in the T4 condition are 0.51 and 1.48at% respectively, which corresponds well with the composition of the alloy (Table 4.22), validating the approach used for sample preparation and analysis. The Si content is in reasonable agreement with a previous study by Taylor and co-workers [48], in which electron probe microanalysis (EPMA) was used to show that the amount of Si in the matrix was ~ 1.3wt% for an Al-7Si-Mg alloy with 0.5wt% Mg. Artificial aging at 180^{o}C for 10 min of the T4 sample does not result in a significant change in the composition of the matrix, measuring 0.52at% Mg and 1.46at% Si. However, further artificial aging causes a gradual decrease in matrix solute content due to precipitation reactions, with the 120h NA,180^{o}C-1h sample containing 0.35at% Mg and 1.41at% Si. Finally, peak aging (120h NA,180^{o}C-4h) results in the lowest matrix solute compositions of 0.12at% Mg and 1.04at% Si. When no natural aging precedes artificial aging, it is seen that the matrix composition decreases more rapidly than when natural pre-aging occurs, with the 0h NA,180^{o}C-10min sample's matrix containing 0.43at% Mg and 1.40at% Si. This decreases further to 0.25at% Mg and 1.23at% Si after 1 h at 180^{o}C, finally reaching values of 0.11at% Mg and 1.13at% Si after 4 h at 180^{o}C. Also, the final matrix compositions of both 180^{o}C-4 h artificially aged samples are similar, regardless of the differences in precipitation sequence caused by natural pre-aging.

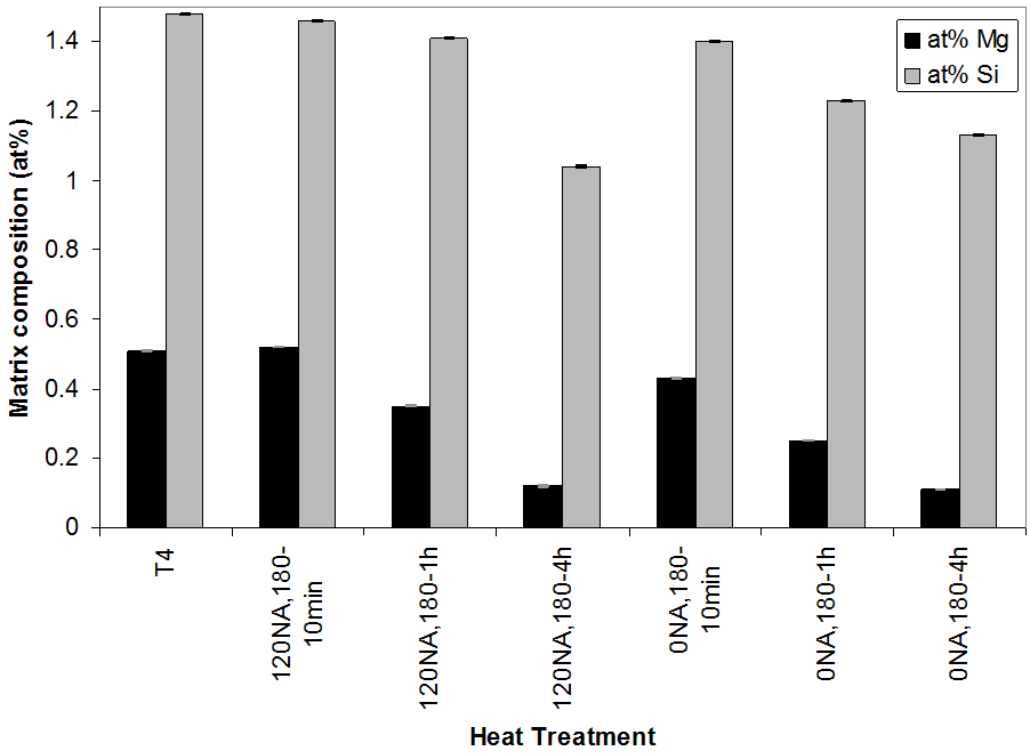

Figure 4.77: The Mg and Si compositions of the F357 matrix in different heat treatment conditions.

4.14.2.4. Number density of precipitates

The number density of precipitates for alloy F357 artificially aged at 180^{o}C for up to 4 h is shown in Figure 4.78(a) following 120 h of natural pre-aging and in Figure 4.78 (b) following no natural pre-aging. Figure 4.78 illustrates that the various precipitates can co-exist during precipitation, which is not discernible from equation 2.1.

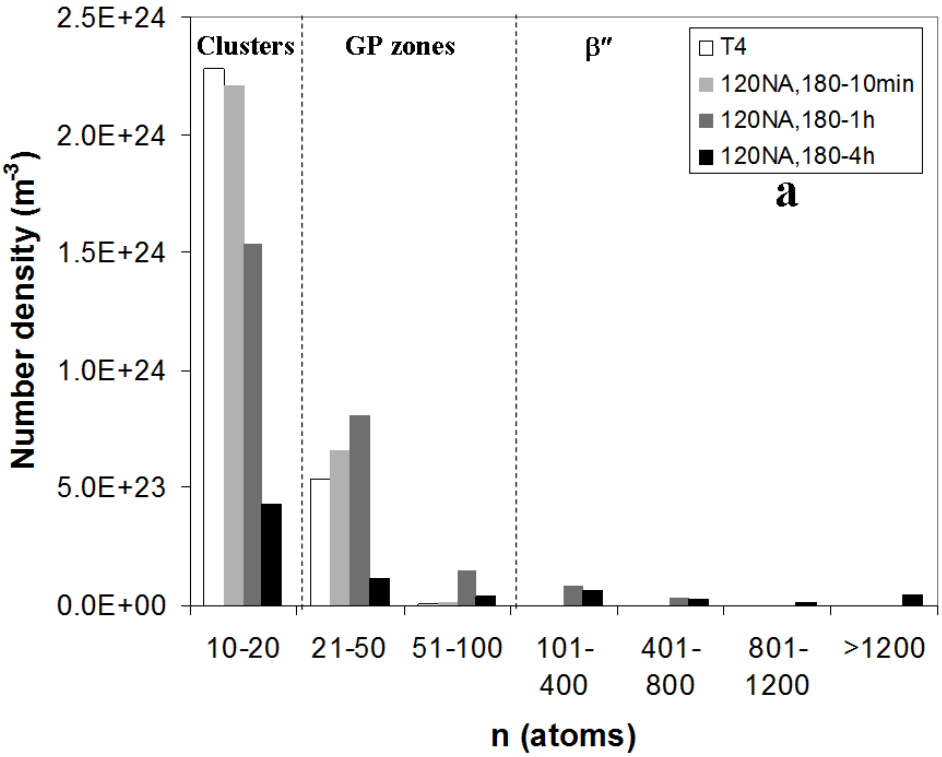

Figure 4.78(a): Comparison of the number density of precipitates for alloy F357 artificially aged at 180°C following 120 h natural pre-aging.

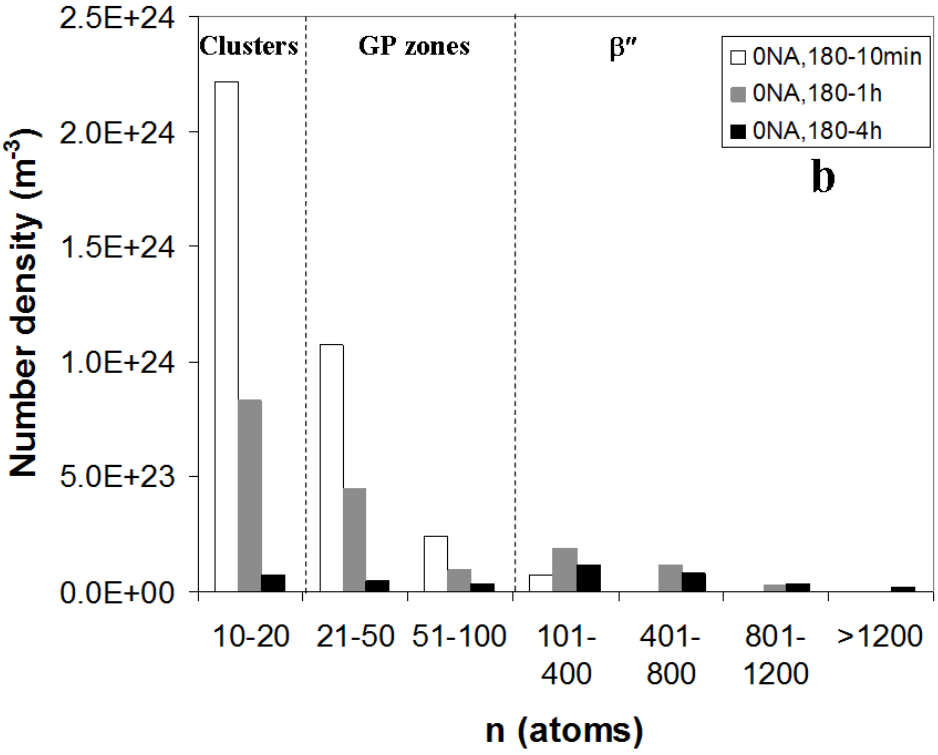

Figure 4.78(b): Comparison of the number density of precipitates for alloy F357 artificially aged at 180°C following no natural pre-aging.

4.14.2.5. The Mg:Si ratio of clusters and precipitates in alloy F357

The composition of the precipitates analysed by APT is normally expressed through the ratio of the main alloying elements, rather than the total quantity of aluminium and solute atoms that are detected in the precipitates [42]. This is due to the issues associated with the acquisition and analysis of atom probe data, especially regarding aberrations in preferential evaporation and ion trajectory [119,120]. Considering the proposed decomposition of the SSS of Al-Si-Mg alloys in equation 2.1, it is seen that the Mg:Si ratio theoretically increases from 0.83 in β″ to 1.7 in β′ to 2 in β. The Mg:Si ratio of solute clusters, GP zones and β″-needles after various stages of artificial aging is shown in Figure 4.79(a) for samples that experienced 120 h natural pre-aging and in Figure 4.79(b) for samples that experienced no natural pre-aging. It is seen that, in general, the Mg:Si ratio increases from ~ 0.6-1.2 with the number of solute atoms within the precipitates.

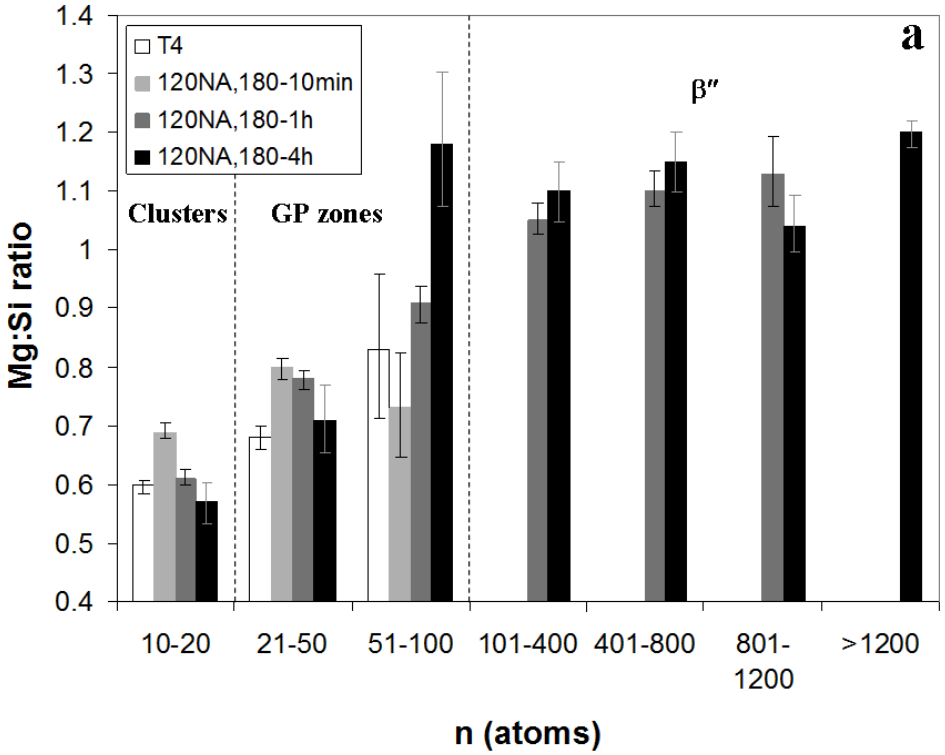

Figure 4.79(a): The Mg:Si ratio of solute clusters, GP zones and β″-needles in F357 samples that were naturally aged for 120 h prior to artificial aging.

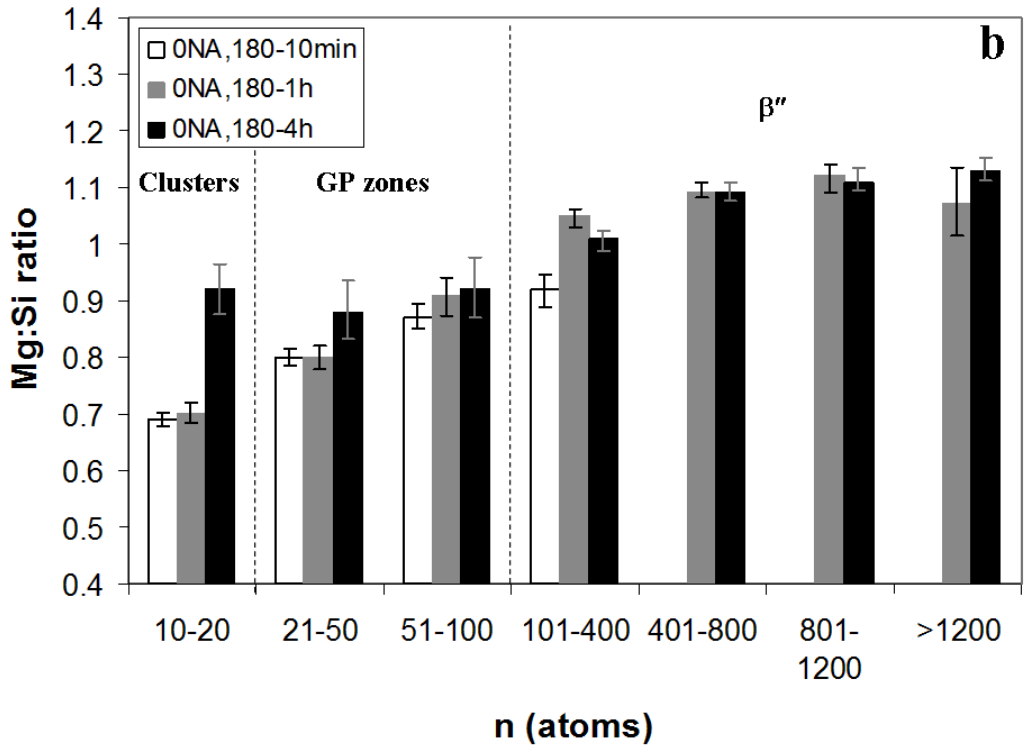

Figure 4.79(b): The Mg:Si ratio of solute clusters, GP zones and β″-needles in F357 samples that were not naturally aged prior to artificial aging.

4.14.2.6. Incorporation of Al into clusters and precipitates of alloy F357

Significant quantities of Al have been detected in all precipitates in this study, despite it being generally accepted that the β″-phase consists of only Mg and Si (Mg_5Si_6) [45]. On average, the solute clusters were found to contain ~ 3.7at% Mg and 5.5at% Si, the GP zones ~ 6.1at% Mg and 6.5at% Si and the β″-needles ~ 10.5at% Mg, and 9.3at% Si. Buha and co-workers [42] also found that the clusters, GP zones and β″-needles in wrought alloy 6061-T6 contained significant amounts of between 65 and 80at% Al. Similar results have also been reported by Vaumousse and co-authors [98] for an Al–Mg–Si–Cu alloy containing an excess of Si. Structural models that accommodate Al atoms in β″-needles and GP zones have been proposed based on TEM studies [118,121].

4.14.2.7. Incorporation of Cu into clusters and precipitates of alloy F357

A few APT precipitation studies have been conducted using pure ternary Al-Mg-Si alloys [50,80]. However, addition of other alloying elements and impurity elements in aluminium alloys can influence precipitation. The addition of Cu for example is

claimed to lead to a higher nucleation rate and refinement of GP zones and β″-precipitates in these alloys [50,51]. The F357 alloy used in this study is a commercial alloy containing numerous alloying elements, with a Cu content of 0.02at% (Table 4.22). The Cu content of the clusters/precipitates is shown in Fig. 4.80(a) for artificial aging with 120 h prior NA and in Fig. 4.80(b) for artificial aging without prior NA.

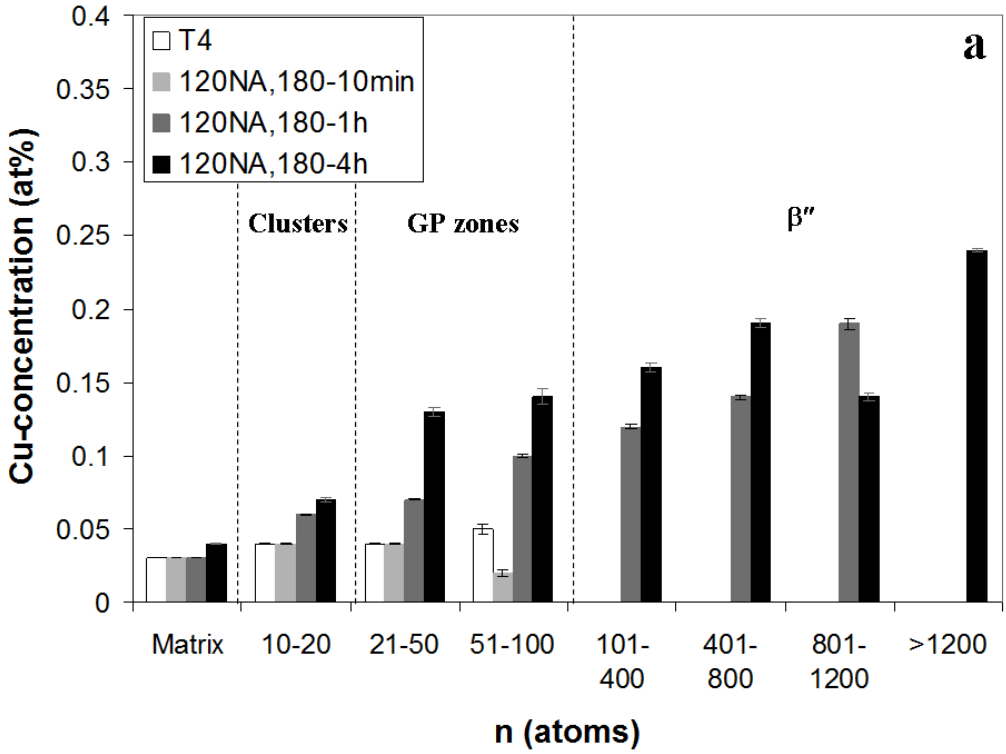

Figure 4.80(a): The Cu content in at% of the clusters/precipitates after artificial aging of alloy F357 with 120 h prior NA.

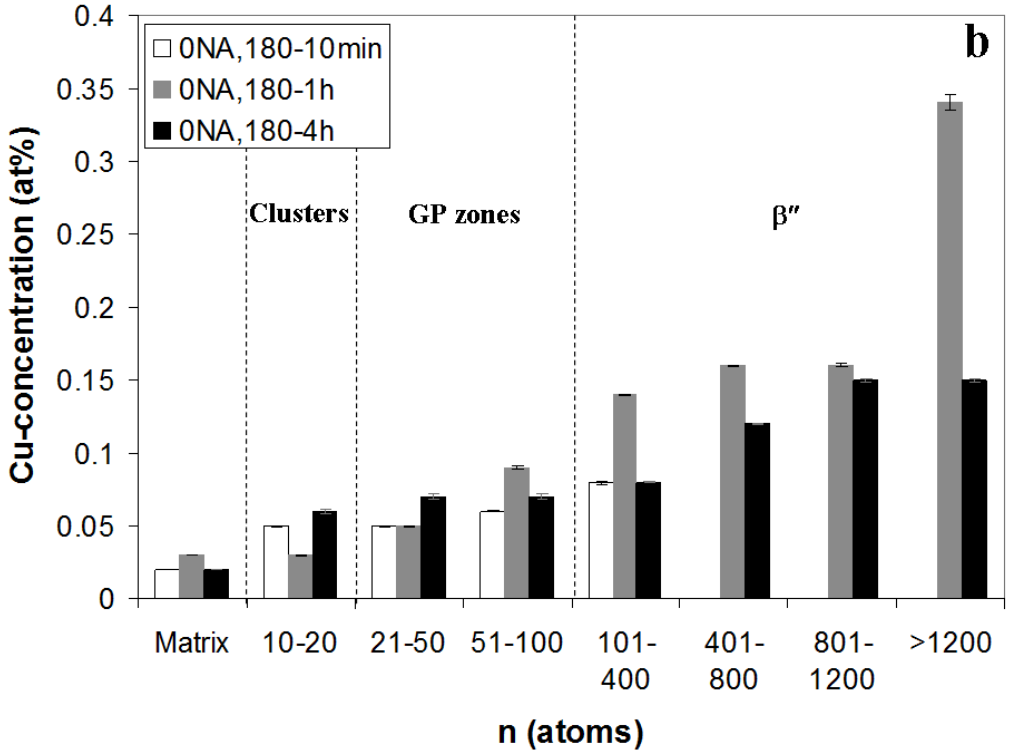

Figure 4.80(b): The Cu content in at% of the clusters/precipitates after artificial aging of alloy F357 without prior NA.

The matrix content of Cu analysed by APT is generally similar to the nominal Cu composition of the alloy, namely 0.02at%. In general, the Cu-content of the particles increases with artificial aging time and as the decomposition of the SSS progresses from clusters to GP zones to β″. Buha and co-workers [42] also found in a 6061-T6 wrought alloy that all precipitates classified as GP zones and β″ were enriched in Cu, whereas no Cu was associated with the solute clusters. Considering Table 4.22, it is seen that Fe and Ti are the other main alloying elements in this alloy. However, neither Fe nor Ti was detected in noteworthy quantities within any of the precipitates in this study and they were detected in the matrix only as trace elements. These elements are rather incorporated into intermetallic particles of which π-$Al_8FeMg_3Si_6$, β-Al_5FeSi and Al_3Ti are the most common in this alloy [HM8].